UNIVERSITE CATHOLIQUE DE LOUVAIN
FACULTY OF SCIENCE, DEPARTMENT OF GEOGRAPHY
EARTH AND LIFE INSTITUTE
GEORGE LEMAITRE CENTER FOR EARTH AND CLIMATE RESEARCH

# Characterizing soil physical crusts in loamy soils using spectral data processing techniques from proximal and remote sensing

DOCTORAL DISSERTATION PRESENTED BY

**GIACOMO CRUCIL**

IN PARTIAL FULFILLMET OF THE
REQUIREMENTS FOR THE DEGREE OF
DOCTOR IN SCIENCES

THESIS COMMITTEE:

| | |
|---|---|
| Prof. Kristof Van Oost (supervisor) | Université Catholique de Louvain |
| Prof. Sébastien Lambot (supervisor) | Université Catholique de Louvain |
| Prof. Marie-Laurence De Keersmaecker (chair) | Université Catholique de Louvain |
| Prof. Bas van Wesemael (secretary) | Université Catholique de Louvain |
| Prof. Charles Bielders | Université Catholique de Louvain |
| Prof. Jeroen Meersmans | Université de Liège |
| Dr. Florian Wilken | Universität Augsburg |

LOUVAIN-LA-NEUVE, APRIL 2022

# List of publications

Chapter 2 is based on the published article:
*Crucil G., Castaldi F., Aldana-Jague E., van Wesemael B., Macdonald A., & Van Oost K. (2019). Assessing the performance of UAS-Compatible multispectral and hyperspectral sensors for soil organic carbon prediction. Sustainability (Switzerland), 11(7).*
*https://doi.org/10.3390/su11071889*

Chapter 3 is based on the published article:
*Crucil G., & Van Oost K. (2021). Towards mapping of soil crust using multispectral imaging. Sensors, 21(5), 1–19.*
*https://doi.org/10.3390/s21051850*

Chapter 5 is based on the published article:
*Crucil, G.; Zhang, H.; Pauly, K.; Van Oost, K. A Semi-Empirical Anisotropy Correction Model for UAS-Based Multispectral Images of Bare Soil. Remote Sens. 2022, 14, 537.*
*https://doi.org/10.3390/rs14030537*

# List of abbreviations

**°C**: Degree Celsius
**1D**: 1st derivative
**ANIF**: Anisotropy Factor
**ASD**: Fieldspec 3 FR spectrometer from Analytical Spectral Devices, Inc.
**BRDF**: Bidirectional Reflectance Distribution Function
**cm:** Centimeter
**$CO_3$:** Carbon trioxide
**cr**: Continuum removal
**deg**: Degree
**DR**: Deleted Roughness (dataset)
**DSM**: Digital Surface Model
**F**: Focal Distance
**FOV**: Field OF View
**g**: Gram
**GPS**: Global Positioning System device
**ha**: Hectare
**iqr**: Inter-Quantile Range
**J**: Joule
**KE**: Cumulative Kinetic Energy
**kg**: Kilogram
**m**: Metre
**mm**: Millimetre
**MRE**: Mean Relative Error
**NIR**: Near Infrared
**nm**: Nanometre
**OH:** hydroxyl group
**PLSR**: Partial Least Squares Regression
**PS_zen**: sensor zenith
**$R^2$**: Coefficient of Determination
**RC**: Runoff Coefficient
**refl**: reflectance
**Rel_az**: Relative azimuth
**Rel_zen**: Relative zenith
**Rf**: Rainfall measured as weight in grams
**RG**: Random Roughness
**RMScorr**: Root Mean Squared correlation
**RMSE**: Root Mean Square Error
**RPD**: Ratio of Performance to Deviation
**RPIQ**: Ratio of Performance to Inter-Quantile range
**RS**: Remote Sensing
**RUSLE**: Revised Universal Soil Loss Equation
**S.Rf**: Sediment exported per unit of rainfall
**S**: Sediment exported
**sd**: Standard Deviation
**Seq**: Sequoia multispectral camera from Parrot Drones S.a.s.,
**SfM**: Structure from Motion
**SNR**: signal-to-noise ratio
**SNV**: Standard Normal Variate
**SOC**: Soil Organic Carbon
**Sol_zen**: solar zenith
**SOM**: Soil Organic Matter
**STS**: STS VIS and STS NIR spectrometers from Ocean Optics Inc.
**SWIR**: Short Wave Infrared
**Tc**: Mini-MCA6 multispectral camera from Tetracam Inc.
**USDA**: United States Department of Agriculture
**USLE**: Universal Soil Loss Equation
**VIP**: Variable Importance in the Projection
**vis**: visible

# Table of Contents

**Chapter 1: General introduction ..... 1**

1.1 State of the art ..... 1

1.1.1 Background ..... 1
1.1.2 Modelling of water erosion ..... 2
1.1.3 Soil physical crust ..... 3
1.1.4 Soil spectroscopy ..... 6
1.1.5 Remote sensing of soil properties ..... 8

1.2 Problem statement ..... 10

1.3 Thesis objectives and outline ..... 11

**Chapter 2: Assessing the performance of UAS-compatible multispectral and hyperspectral sensors for soil organic carbon prediction ..... 15**

2.1 Introduction ..... 16

2.2 Materials and Methods ..... 19

2.2.1 Soil Datasets ..... 20
2.2.2 Sensor Equipment ..... 20
2.2.3 Spectral Measurements ..... 21
2.2.4 Comparison between Measurement Setups ..... 23
2.2.5 Model Transferability between Measurement Setups ..... 24

2.3 Results ..... 26

2.3.1 Validated PLSR Models ..... 26
2.3.2 Evaluation of Model Transferability ..... 31

2.4 Discussion ..... 32

2.5 Conclusions ..... 36

**Chapter 3: Towards mapping of soil crust using multispectral imaging ..... 39**

3.1 Introduction ..... 40

3.2 Materials and Methods ..... 41

3.2.1 Experiment Design and Data Series ..... 41

3.2.2 Samples Setup ..... 42
3.2.3 Rainfall Data ..... 43
3.2.4 Sensors ..... 44
3.2.5 Roughness Characterization Using Photogrammetry ... 44
3.2.6 Spectral Data Acquisition and Pre-Processing ..... 46
3.2.7 Multispectral Data Extraction ..... 49
3.2.8 Spectral Modelling ..... 50
3.3 Results and Discussion ..... 53
3.3.1 KE, Crusting and Roughness Data ..... 53
3.3.2 Hyperspectral Variable Importance ..... 54
3.3.3 Correlation with Multispectral Data ..... 56
3.3.4 Modelling Multispectral Data ..... 59
3.3.5 Multispectral Variable Importance ..... 63
3.4 Conclusions ..... 64

**Chapter 4: Modelling soil physical crust development in field conditions ..... 67**

4.1 Introduction ..... 67
4.2 Materials and Methods ..... 68
4.2.1 Experimental plots ..... 68
4.2.2 Rainfall data ..... 69
4.2.3 Multispectral imaging ..... 70
4.2.4 Hyperspectral sensing ..... 71
4.2.5 Spectral modelling of KE ..... 72
4.2.6 Runoff and sediment data ..... 74
4.3 Results and Discussion ..... 76
4.3.1 PLSR models of KE ..... 76
4.3.2 Sediment modelling ..... 78
4.4 Conclusions ..... 81

**Chapter 5: A semi-empirical anisotropy correction model for UAS-based multispectral images of bare soil ..... 83**

5.1 Introduction ..... 84
5.2 Materials and Methods ..... 85

5.2.1 Multispectral imaging system ..... 85
5.2.2 Data collection and pre-processing ..... 86
5.2.3 ANIF correction model ..... 89
5.2.4 Correction evaluation ..... 94
5.3 Results ..... 95
5.4 Striping issue ..... 95
5.4.1 Model fit ..... 97
5.4.2 Correction evaluation results ..... 101
5.5 Discussion ..... 104
5.6 Conclusions ..... 105
**Chapter 6: General conclusions ..... 107**
6.1 Main findings ..... 107
6.2 Potential, limitations and future perspectives ..... 110
**Appendix A ..... 115**
**Appendix B ..... 117**
**Appendix C ..... 121**
**References ..... 127**
**List of Figures ..... 143**
**List of Tables ..... 151**

# Chapter 1

# General introduction

## 1.1 State of the art

### 1.1.1 Background

Soils are a fundamental component to sustain life on Earth but the impact of human activities for sustainable use of soil is reaching a critical limit (FAO and ITPS, 2015). In recognition of this issue, several initiatives to identify soil threats, inform political decisions and propose global mitigation and management solutions have been attempted. The Global Assessment of Soil Degradation (GLASOD) project (Oldeman, Hakkeling and Sombroek, 1990), during the 1980-1990's, was the first effort aimed at inventorying and mapping worldwide soil degradation processes. The proposition for a Soil Thematic Strategy of the European Union (Commission of the European Communities (CEC), 2006) provided a formal classification of soil degradation processes, namely, erosion, decline in organic matter, local and diffuse contamination, sealing, compaction, salinisation, floods and landslides. It raised the attention on to the fact that the detrimental impacts of these degradation processes represent a serious threat to food production, water and air quality, human safety, biodiversity, and climate. Most importantly, it also emphasized on the concept that, as soil formation is an extremely slow process, soil can be considered essentially as a non-renewable resource. The most recent global initiatives are the Global Soil Partnership and its Intergovernmental Technical Panel on Soils (ITPS), established by the Food and Agriculture Organization (FAO, https://www.fao.org/global-soil-partnership/en/), and the Sustainable Development Goals of the United Nations (UN), specifically the target 15.3 (https://sdgs.un.org/goals/goal15). The most recent European strategy for soil protection is represented by the EU mission "A soil deal for Europe".

Among the identified degradation processes, soil erosion represents one of the most significant threats to soil functions (Montanarella *et al.*, 2016). Soil erosion by water, in particular, accounts for the greatest loss of soil in Europe compared to other erosion processes (i.e., wind and tillage erosion) (Panagos *et al.*, 2015). To mitigate these impacts, a broad range of runoff and erosion models has been developed (Pandey *et al.*, 2016; Borrelli *et al.*, 2021).

However, the limitations and considerable uncertainties associated with model predictions have been repeatedly reported (Cerdan *et al.*, 2010; Auerswald *et al.*, 2014; Quine and Van Oost, 2020).

### 1.1.2 Modelling of water erosion

Soil erosion by water has been defined as the wearing of the earth's surface by the force of water and gravity, and consists of soil particle dislodgement, entrainment, transport, and deposition (McCool and Williams, 2008). It is a complex phenomenon driven by the interaction of several factors and processes, as soil characteristics, rainfall, climate, topography, and human activities. These factors, and the progression from dislodgement and entrainment to deposition are also highly dynamic in space and time. As a result, the reliability of runoff and erosion assessments and their scientific interpretation nowadays still poses several challenges.

The Universal Soil Loss Equation (USLE, Wischmeier and Smith, 1978), its revised version RUSLE (Renard, 1997) and subsequent (R)USLE-based models are nowadays the most widely used erosion models worldwide (Borrelli *et al.*, 2021). These are empirical approaches obtained from regression analyses of erosion losses, from a significant series of standardized plot measurements, versus a set of controlling factors (summarized in five parameters: R = rainfall-runoff erosion; K = soil erodibility; L = slope length; C = cover-management; P = support practice factor), but they are focused on modelling sheet and rill erosion. In parallel, a plethora of process-based physical models has been developed through the years to focus on other specific erosion dynamics. Reviewing efforts of this approaches (Pandey *et al.*, 2016; Borrelli *et al.*, 2021) highlighted nonetheless several issues. Empirical models, despite being suitable for wide scale applications, are usually limited by the need of extensive, long-term field measurements and by the possible biases introduced by abnormal events or by the excessive generalization of spatially variable parameters. This is one of the reasons why recent soil erosion predictions works at the European scale (Panagos *et al.*, 2015) have been criticized by the scientific community (Auerswald *et al.*, 2015; Fiener and Auerswald, 2016). Moreover they may be not suitable to extrapolate results for climate change scenarios (Li and Fang, 2016; Quine and Van Oost, 2020). Process-based models, on the other side, are better suited for event-based predictions and at the spatial scale of fields or small watershed, and often lack proper validation. In general, it is commonly

recognized that good quality and extensive data are required for proper model development and calibration.

A primary challenge is posed by the fact that, in field observations, the same apparent soil surface and rainfall conditions do not necessarily result in the same runoff and erosion rates (Le Bissonnais, Cerdan, *et al.*, 2005; Cerdan *et al.*, 2010; Kim and Ivanov, 2014). This has been repeatedly observed in measurements from paired plots, where the variability of runoff and erosion responses showed a difference of up to two orders of magnitude (Nearing, Govers and Norton, 1999; Kim, Ivanov and Fatichi, 2016). Small-scale experiments (Le Bissonnais, Cerdan, *et al.*, 2005; Leys *et al.*, 2007; Carmi and Berliner, 2008; Cheng, Ma and Cai, 2008; Langhans *et al.*, 2011; Van den Putte *et al.*, 2013) suggested that micro-scale properties of the first few centimetres of the soil surface have an important control on its infiltration capacity and erodibility. More specifically, these studies showed that changes in roughness and the development of soil crusts are important factors controlling the above-mentioned variability, particularly on fine-textured soils. However, these properties are in continuous evolution in both space and time in response the energetic inputs of rainfall, farming operations and biotic processes. Even under laboratory conditions, or controlled field experiments, these factors are difficult to quantify and are usually described using simplified expert-based classes (Cerdan *et al.*, 2002; Cantreul *et al.*, 2020). Another series of challenges stem from the uncertainties in how to tackle and incorporate water and sediment connectivity into spatially explicit modelling approaches (Antoine, Javaux and Bielders, 2009; Peñuela, Javaux and Bielders, 2015; Nunes *et al.*, 2018), and the optimal scale to study them (Cantreul *et al.*, 2018).

### 1.1.3 Soil physical crust

The term soil crusting refers to the forming processes and the hydrological consequences of a thin layer of few millimetres at the soil surface with higher bulk density, reduced porosity and high penetration resistance, which favours runoff initiation and inter-rill soil erosion (Valentin and Bresson, 1998). It is recognized as a soil degradation process as it reduces water infiltration, increases erosion, inhibits seedling emergence and soil aeration. Soil crust generation starts when rainfalls cause the sealing of soil surface due to the breakdown of soil aggregates into finer particles, leading to the infilling of the pores (Nciizah and Wakindiki, 2015). Crust formation is then the consequence of the consolidation, drying and hardening of the seal. Four

aggregate breakdown mechanisms have been classified : i) slaking (rupture from compression of entrapped air bubbles), ii) differential swelling of clay, iii) raindrop impact iv) osmotic physico-chemical dispersion (Le Bissonnais, 1996). Several soil factors influence aggregate breakdown, namely wetting rate, antecedent moisture conditions, soil texture, soil mineralogy, clay type, soil organic matter (SOM) and rainfall characteristics (Nciizah and Wakindiki, 2015). In this context, crusts are commonly classified into two subsequent stages, “structural” and “depositional”: the first refers to the an early stage of formation due to mechanical breakdown and compaction of soil aggregates, the second refers to the result of a sedimentary layer overlaying a previously developed structural crust (Valentin and Bresson, 1992).

The role of soil crust on the increase of soil erosion by water is mainly due to the reduction of water infiltration, which induces ponding and then runoff. Dynamic interactions between crusting, runoff and erodibility have been documented, but they have been complicated by the observation that soil properties affecting erodibility are similar to those affecting crusting (texture, organic matter content, aggregate stability, initial water content, vegetation residue, biotic activity). The issue derives from the fact that some individual relationships behave differently for crusting and erodibility in response to different factors (Le Bissonnais, Daroussin, *et al.*, 2005). For example, wetting rate was observed to exert a greater effect in the formation of a seal on clay soils than on loamy soils, while raindrop kinetic energy showed an opposing behaviour (Singer and Shainberg, 2004). On the other hand, consistent is the role of soil organic matter, which reduces the clay water intake, improves its cohesion and general soil aggregate stability, with the consequence of reducing soil slaking and sediment generation (Chenu, Le Bissonnais and Arrouays, 2000; Zaher, Caron and Ouaki, 2005; Leys *et al.*, 2007). There are also still open issues in the relationship between soil surface roughness and crust during runoff generation: roughness was considered a factor delaying the reduction in infiltration due to crusting, but several studies provided contradictory evidence (Carmi and Berliner, 2008). Further complications come from the fact that, in particular conditions of climate and soil stability (especially in arid climates), crust properties can be modified by the biological activity of cyanobacteria, algae, microfungi, lichens and bryophytes (Chamizo *et al.*, 2012). Crust development has also been observed to occur up to at least 28 days (and possibly 71) after seedbed preparation (Hardie and Almajmaie, 2019). Erodibility and crusting also vary

in space, at different scales within a field or landscape (Le Bissonnais, Daroussin, *et al.*, 2005).

Incorporating the causes and the effects of soil crusting into runoff and erosion models still poses a big challenge. A preliminary issue stems from the fact that soil crust cannot be univocally defined with a single indicator, but a set of different properties must be considered (Valentin and Bresson, 1998; Nciizah and Wakindiki, 2015; Thomsen *et al.*, 2015). Several methods were proposed to monitor soil crust, directly through morphological changes, or indirectly through sealing indexes and surface strength indexes. Crust morphological changes regard measuring crust thickness, surface roughness, the diameter "$D_{lim}$" of the smallest clods not incorporated in the crust (Boiffin and Monnier, 1985), crust density and total porosity (Cresswell and Hamilton, 2002) or surface textural changes (Goldshleger *et al.*, 2004). Sealing indexes are based on measurements of the decrease of crust hydraulic conductivity, while crust strength indexes can be obtained from penetrometer tests (Valentin and Bresson, 1998). In different studies, both $D_{lim}$ and sealing indexes have been linearly related to cumulative rainfall kinetic energy (Valentin and Bresson, 1998). It is indeed generally agreed that aggregate breakdown under rainfall is to a large extent a function of the kinetic energy of raindrops (Le Bissonnais, 1996; Geeves, 1998). Soil basic infiltration rate into a crusted soil has, in fact, also been satisfactory predicted by using the accumulated rainfall kinetic energy for the season (Hussein, Awad and Abdul-Jabbar, 2010). Unfortunately, the main problem for indirect indices is that they remain strictly related to the local soil properties and conditions in which they were developed and thus cannot be easily generalized.

Nowadays, soil erosion models still cannot account for all the factors affecting crust formation and their hydrological consequences (Nciizah and Wakindiki, 2015; Hardie and Almajmaie, 2019). Few models account for the transient nature of soil hydraulic conductivity due to crust development (B. A. King and D. L. Bjorneberg, 2012), and even less can also explicitly take into account the spatial heterogeneity of soil surface properties (Laloy and Bielders, 2008). Large scale models are also still dependent on empirical erodibility parameters. The integration of a physically-based soil crusting, in addition to the more classical erodibility factor, should significantly improve regional scale erosion modelling (Le Bissonnais, Daroussin, *et al.*, 2005) like demonstrated in other studies at smaller scale (Cerdan *et al.*, 2002). It is, however, generally recognized that more precise, accurate, and spatially

distributed information about soil characteristics would be required for model development.

### 1.1.4 Soil spectroscopy

Spectroscopy is a measuring technique based on the principle that the interaction between incoming radiation and chemical compounds occurs with compound-specific molecular vibrations, whose signature in the absorption spectrum can be used for analytical purposes (Siesler *et al.*, 2008). Visible–Near Infrared (vis–NIR) laboratory spectrometry, coupled with improvements in computing and statistics, evolved as a reliable discipline for the estimation of a wide range of soil properties (Viscarra Rossel *et al.*, 2006; Ben-Dor *et al.*, 2009). It is an analytical technique that represents a convenient alternative to traditional wet-chemistry analysis, for the advantages of being fast, cost-effective, environmental-friendly, non-destructive, reproducible, and repeatable (Nocita *et al.*, 2015). Reviews of numerous spectral modelling attempts (Stenberg *et al.*, 2010) showed that the visible and infrared portions of the spectrum (350-2500 nm) contain key spectral features for proficient modelling ($0.41 < R^2_{\text{validation}} < 0.92$) of soil properties relevant to erosion susceptibility, such as components of soil organic matter (or soil organic carbon -SOC- as its indirect estimate), texture, or moisture content. The creation of spectral libraries at national (Romero *et al.*, 2018), continental (Stevens *et al.*, 2013) and global (Viscarra Rossel *et al.*, 2016), scales testifies the growing interest of the scientific community for the potential of this analysis technique.

Nonetheless, several operative aspects must be considered for an efficient employment of this technique. First, the accuracy of laboratory spectroscopy is controlled by the technical characteristics of the spectrophotometers: i) spectral resolution, ii) spectral range, iii) stability of the measurement conditions, and iv) signal-to-noise ratio (SNR). Secondly, these characteristics need to match the detectability requirements of the spectral features of the target variable. Furthermore, although laboratory spectroscopy can provide robust and accurate estimates of soil properties, it only provides an estimate at the sample point location and geostatistical techniques must be used to infer continuous spatial information. Regarding data processing, a challenge is posed by the fact that diffuse reflectance spectra of soil in the vis–NIR are largely nonspecific due to the overlapping absorption of soil constituents and to the scattering effects caused by soil texture, particle segregation or specific constituents. These factors result in complex absorption patterns

that need to be mathematically extracted from the spectra and correlated with soil properties, requiring a rich sampling for the calibration of multivariate analysis techniques (e.g., Partial Least Squared Regression -PLSR-, random forest, artificial neural networks) (Stenberg *et al.*, 2010).

The recent development of lightweight spectrophotometers opened the road for proximal sensing[1] applications like the field employment of soil spectrometry (Soriano-Disla *et al.*, 2017), and to the advantages of much higher data density (Franceschini *et al.*, 2018). Imaging spectrometry represents an even further step, providing a tangible perspective for adding spatial detail to spectral information, thereby enhancing the thematic application of spectral recognition algorithms, and overcoming the limitation of point spectrometry (Ben-Dor *et al.*, 2009; Ben-Dor, 2012; Chabrillat *et al.*, 2019). The employment of proximal sensing spectrometry in outdoor or field conditions, nonetheless, has been less explored and reported to be much less accurate than laboratory measurements. This is due to a series of 'in situ' factors, like soil-to-sensor distance and inclination, illumination conditions, contamination by other targets, and field natural heterogeneity concerning soil moisture and roughness (Kühnel and Bogner, 2017; Franceschini *et al.*, 2018). A peculiar element challenging the accuracy of soil spectral data is indeed the anisotropic response of soil to radiation, resumed in the theory of the Bidirectional Reflectance Distribution Function (BRDF) (Ben-Dor *et al.*, 2009; Ben-Dor, 2012). Furthermore, depending on the instrumental design, these approaches are only applicable at plot/field scale, and their integration in larger scale assessments is still in its infancy (Žížala, Zádorová and Kapička, 2017).

The spectral properties of crusted soils have been already the subject of studies that linked specific spectral features to crust development. Rainfall energy in controlled experiments has been indeed observed to alter the particle size composition of soil surface, depending on the texture, mineralogy, and rainfall amount. Hussein, Awad and Abdul-Jabbar (2010) observed a surface crust texture which is higher in silt and lower in sand and clay compared to that of the original soil. On the other hand, several other studies observed an enrichment of clay particles on the soil crust surface (Ben-Dor *et al.*, 2003, 2004; Eshel, Levy and Singer, 2004). In alle these studies, soil crust spectral changes have been directly related to soil

[1] Proximal sensing: when the sensor is close to the object and is installed on platforms ranging from handheld, fixed installations, or robotics and tractor-embedded sensors.

infiltration rates and cumulative rainfall kinetic energy. Ben-Dor *et al.* (2003) more specifically associated the increase in soil albedo with fine particle enrichment, and ascribed spectral features to OH groups in the clay lattice (at 2200 nm) or $CO_3$ in calcite minerals (at 2330 nm). A spectral feature at 680 nm as also been used to discriminate between physical and biological soil crusts (Chamizo *et al.*, 2012). Studies that, on the other hand, dealt with the radiometric effects of soil roughness (Croft, Anderson and Kuhn, 2009, 2012, 2014; Piekarczyk *et al.*, 2016), successfully developed and refined models of soil surface roughness using proximal hemispherical measurements of hyperspectral directional reflectance factors. Nonetheless, they recognized the difficulty of separating the contribution of soil variables like roughness, moisture, and organic carbon to soil reflectance factors, and the complexity that exists in attempting to retrieve them from remotely sensed optical data.

### 1.1.5 Remote sensing of soil properties

Remote sensing is the practice of deriving information about Earth's land and water surface using images acquired from an overhead perspective, using electromagnetic radiation in one or more regions of the electromagnetic spectrum, reflected or emitted from the Earth's surface (Campbell and Wynne, 2011). It commonly employs airborne or satellite-borne radiometric sensors, but the last decade saw the rise of UAS-based applications (Unmanned Aircraft Systems, also known as UAV: Unmanned Aerial Vehicles, i.e., drones) (Aasen *et al.*, 2018). Recent reviews (Mulder *et al.*, 2011; Ben-Dor and Demattê, 2015; Angelopoulou *et al.*, 2019; Tziolas *et al.*, 2021) highlighted the crescent activity in the employment of remote sensing for soil surveying and their importance for: i) supporting the segmentation of the landscape into homogeneous units for analytical purposes; ii) allowing measurement or prediction of soil properties with physically-based and empirical methods; iii) supporting spatial interpolation of sparsely sampled soil property data. More in detail, remote sensing potential has been successfully employed to target soil properties related to runoff and erosion, like soil organic carbon (Aldana-Jague *et al.*, 2016; Angelopoulou *et al.*, 2019; Castaldi *et al.*, 2019; Dvorakova, Heiden and van Wesemael, 2021), soil moisture (Zhang and Zhou, 2016; Babaeian *et al.*, 2019; Wu *et al.*, 2019), salinity and contamination (Ben-Dor *et al.*, 2009), fine scale topography and roughness (Anderson and Croft, 2009). As a result, some of these approaches are now being explicitly directed in the estimation of the parameters of

popular wide-scale erosion models (e.g., (R)USLE-based models) (King *et al.*, 2005; Phinzi and Ngetar, 2019).

This discipline seems, nonetheless, still far from maturity as the drawbacks of insufficient accuracy and systematic errors are still often reported in the estimation of soil properties, topographic parameters and land use classification (Phinzi and Ngetar, 2019). The complications of soil roughness, moisture and vegetation residue are still a great deterrent for robust estimation of soil properties from remote sensing (Angelopoulou *et al.*, 2019). In the same class of problems, soil crusting and its textural changes represent another source of uncertainty. A recent study (Prudnikova and Savin, 2021), for example, showed that rainfall and soil crust development negatively affected the accuracy of SOM predictions with Sentinel-2 satellite data. Future studies should therefore focus on improving the integration of proximal and remote sensing using scaling-based approaches to account for fine-scale and fast-changing surface properties and on the optimal use of all data sources available (Angelopoulou *et al.*, 2019; Tziolas *et al.*, 2021). Furthermore, since advances in proximal sensing have evolved much faster than in remote sensing, a technology gap still has to be bridged (Mulder *et al.*, 2011).

When comparing satellite and airborne and UAS solutions, some considerations need to be made. Most of the current and new satellite sensors have a spatial resolution (10–30 m) that does not allow a sufficient explanation of the short-range variability that characterizes some soil variables. Moreover, fixed revisit times may not be optimal for an appropriate temporal coverage, due to the influence of cloud cover, or when dry and bare soil conditions are required. While the spatial resolution of airborne sensors is higher (2–5 m), the high operational costs do not generally allow multi-temporal data to be obtained, which are often necessary to increase the likelihood of collecting soil data in optimal conditions. Consumer-grade UAS and sensors are now mature enough to support the development of geoinformation products and services, in particular small photogrammetric and remote sensing projects (Colomina and Molina, 2014). They represent a superior alternative to ground surveys, as they offer high spatial and temporal resolution at a better time- resource- and cost- efficiency. While they still cannot match the spatial coverage of aerial and satellite data, UAS offer indisputable flexibility advantages in planning and executing the surveys (Aasen *et al.*, 2018). This is supported by a flourishing literature of UAS-based approaches in precision agriculture

(Zhang and Kovacs, 2012; Matese *et al.*, 2015; Menzies Pluer *et al.*, 2020), photogrammetry and topographic analysis (Eltner and Schneider, 2015; Fazeli, Samadzadegan and Dadrasjavan, 2016), carbon export (Wehrhan, Rauneker and Sommer, 2016), and soil surface conditions for erosion assessment (Wassenaar *et al.*, 2005; Corbane *et al.*, 2008; D'Oleire-Oltmanns *et al.*, 2012; Hassan-Esfahani *et al.*, 2015; Eltner, Schneider and Maas, 2016; Pineux *et al.*, 2017). A great opportunity for the advocated integration of UAS data with other remote sensing techniques is represented by data fusion approaches. Data fusion has been defined as "the science of combining measurements, signals, or observations from different sources to obtain a result that is in some sense better than what could have been achieved without this combination" (Schmitt and Zhu, 2016). The choice of a remote sensing instrument is indeed always facing a trade-off, either between spatial resolution and temporal frequency or between spatial resolution and spectral resolution (Ghamisi *et al.*, 2019). In this context, UAS and portable high-resolution spectrometers offer helpful tools for spatio-spectral fusion (i.e. pansharpening) and spatio-spectral fusion (i.e. multiband image fusion).

## 1.2 Problem statement

Quantity and quality of input data are critical for the calibration and validation of both process-based and empirical erosion modelling approaches, but also for their final application as a decision-making tool. Extensive data requirement is an issue often reported for the application of physical models (Pandey *et al.*, 2016), while lack of proper validation is a common issue to all modelling approaches (Borrelli *et al.*, 2021). Wide scale models are also weakened by the improper/excessive lumping of model parameters and by their reliance on a static description of soil erodibility properties, which is wrongfully ignoring the complex effect of their dynamic variability (Laloy and Bielders, 2008; Quine and Van Oost, 2020). In particular, seasonal and intra-seasonal changes in the surface characteristics of the first few centimetres of soil, namely, roughness and crust development, are still poorly considered by modellers. This represents an issue as the effects of the short-term mutual dynamics of these two properties, in response to climate factors, biotic processes and tillage operations, may be greater than expected.

To tackle these problems, the scientific community working on soil erosion modelling is in dire need for accurate and spatially distributed data of soil surface properties. Remote sensing applications are now able to offer the

means to assess spatial-temporal variability of soil conditions quantitatively and accurately at different scales. Practical consideration and issues concerning data resolution, accuracy, and ease of access between the different remote sensing tools are nevertheless limiting the available choices. UAS-based soil spectroscopy and spectral imaging can bridge the gap between satellite/airborne solutions and the necessary ground-based calibrations with undeniably superior flexibility, but not before solving another series of issues severely affecting the quality of its measurements, namely:

- the unknown influence of 'in situ' factors like soil-to-sensor distance and inclination, illumination conditions, inconsistent soil presentation to the sensor, soil moisture, and field natural heterogeneity, partial cover by (non) photosynthetic active vegetation which are specific to sensor characteristics and to the target soil property.
- the largely nonspecific nature of diffuse reflectance spectra of soils in the vis–NIR, due to the overlapping absorption of soil constituents and to the scattering effects caused by soil structure.
- the effect of soil anisotropy on spectral measurements, especially on spectral imaging, and their repercussion on aerial mapping products, i.e., those resulting from photogrammetric approaches.

## 1.3 Thesis objectives and outline

This thesis work is based on the main hypothesis that soil physical crust development, and its effect on soil surface runoff and sediment generation, can be detected by means of low altitude multispectral remote sensing. The general objective of this thesis is to offer quantitative insights and a modelling approach to describe the evolution of the soil physical crust, using UAS-based multispectral data, with a case study focused on loamy soils of the Belgian loess belt. Four specific objectives were tackled in pursue of the general one. These have been structured on an ideological pathway to test a set of sensors and their detection capability for soil properties, starting from laboratory analysis and progressively scaling to the remote sensing domain (Figure 1.1).

Objective 1) To provide a preliminary proof of concept for the spectral modelling of soil surface properties with multispectral imaging. This takes form in the investigation of the capabilities of a range of hyper- and multi-spectral sensors that can be mounted on UAS for SOC estimation. The specific aim is to

compare the influence of spectral resolution and range on SOC prediction accuracy when employing UAS-portable sensors in laboratory and under the environmental influence of outdoor conditions. The choice of SOC as target variable is made for two reasons: i) the availability of a rich soil sample collection, with accurate SOC data from traditional laboratory measurements; ii) the relevance of SOM as a variable influencing soil aggregate stability and crust development. Chapter 2 presents the pursuit of this objective.

Objective 2) To analyse the functional relationships between soil crusting and soil surface reflectance as derived from multispectral imaging and how this can be inferred from low-altitude UAS sensors. More specifically, the aim is disentangling the effects of soil surface roughness from those of crust development on spectral reflectance factors, by establishing and evaluating a dedicated data pre-processing protocol. Chapter 3 presents the pursuit of this objective.

Objective 3) To verify, building on the findings of objective 2, if soil crust development can be described by means of low altitude UAS-based multispectral imaging in real field conditions, and possibly to quantify the contribution of the development of soil crust on sediment yield under natural rainfall conditions on an agricultural loamy soil. Chapter 4 presents the pursuit of this objective.

Objective 4) To address the problems caused by soil anisotropy in UAS-based spectral mapping, by elaborating a semi-empirical correction methodology for multispectral imaging datasets to account for the effects of the BRDF, and by evaluating the benefits of this correction method on the quality of SfM-based multispectral orthomosaics. Chapter 5 presents the pursuit of this objective.

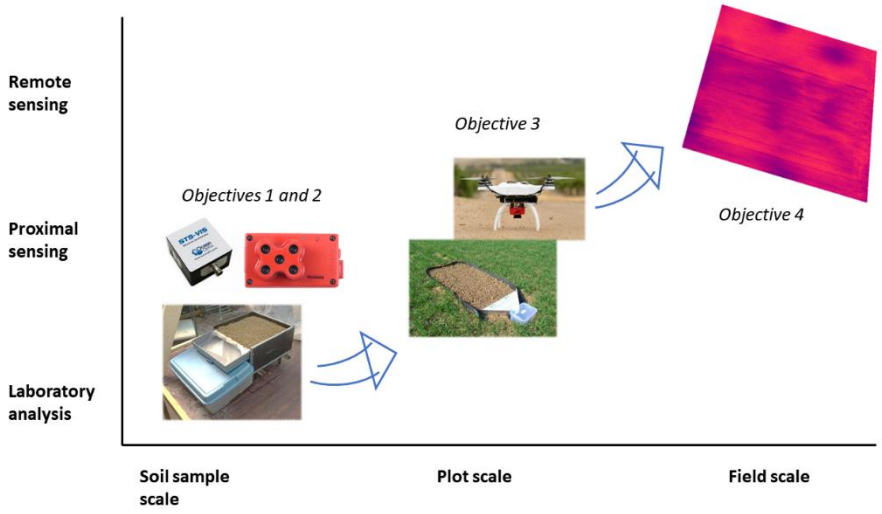


Figure 1.1. This conceptual workflow represents how the four objectives of this thesis have been structured to pursue the general objective. The work started with a test of sensors and their detection capability for soil properties, moving from laboratory analysis and progressively scaling to proximal sensing in outdoor and field conditions, and finally to the remote sensing domain.

# Chapter 2

# Assessing the performance of UAS-compatible multispectral and hyperspectral sensors for soil organic carbon prediction

*The content of this chapter is based on the published article:*
*Crucil G., Castaldi F., Aldana-Jague E., van Wesemael B., Macdonald A., & Van Oost K. (2019). Assessing the performance of UAS-Compatible multispectral and hyperspectral sensors for soil organic carbon prediction. Sustainability (Switzerland), 11(7).*
*https://doi.org/10.3390/su11071889*

## Abstract

Laboratory spectroscopy has proved its reliability for estimating soil organic carbon (SOC) by exploiting the relationship between electromagnetic radiation and key spectral features of organic carbon located in the visible, near infrared and shortwave infrared region (vis-NIR-SWIR, in the 350–2500 nm range). While this approach provides SOC estimates at specific sampling points, geo-statistical or interpolation techniques are required to infer continuous spatial information. UAS-based proximal or remote sensing has the potential to provide detailed and spatially explicit spectral sampling of the topsoil at the field or even watershed scale. However, the factors affecting the quality of spectral acquisition under outdoor conditions need to be considered. In this study, we investigate the capabilities of two portable hyperspectral (STS-VIS and STS-NIR), and two small-form multispectral cameras with narrow bands in the vis-NIR region (Parrot Sequoia and Mini-MCA6), to predict SOC content. We collected spectral data under both controlled laboratory and outdoor conditions, with the latter being affected by variable illumination and atmospheric conditions and sensor-sample distance. We also analysed the transferability of the prediction models between different measurement setups by aligning spectra acquired under different conditions (laboratory and outdoor) or by different instruments. Our results indicate that UAS-compatible small-form sensors can be used to reliably estimate SOC. The results show that: i) the best performance for SOC

estimation under outdoor conditions was obtained using the vis-NIR range ($R^2$ = 0.94), while the addition of the SWIR region decreased the prediction accuracy ($R^2$ = 0.89); ii) prediction models using only the narrow bands of multispectral cameras gave better performances ($R^2$ = 0.93-0.94) than those using continuous spectra from the STS hyperspectral sensors ($R^2$ = 0.85); and iii) when used in outdoor conditions, the micro hyperspectral sensors substantially benefitted from a laboratory model calibration followed by a spectral transfer using an internal soil standard ($R^2$ increased from 0.4 to 0.9). Based on this analysis, we recommend vis-NIR portable instruments for estimating spatially distributed SOC data. The integration of these sensors in UAS-mapping devices could represent a cost-effective solution for soil research and precision farming applications when high resolution data are required.

## 2.1 Introduction

Laboratory spectroscopy has proved its reliability for estimating the soil organic carbon (SOC) concentration by exploiting the relationship between electromagnetic radiation and organic carbon spectral features (Nocita *et al.*, 2015). The key spectral regions affected by SOC content are located in the visible (VIS) region around 664 nm and in the SWIR region from 2100 to 2300 nm (Mouazen *et al.*, 2007; Stenberg *et al.*, 2010; Castaldi *et al.*, 2016). The accuracy of laboratory spectroscopy is mainly controlled by the technical characteristics of the spectrophotometers: i) high spectral resolution, ii) wide spectral range, iii) stability of the measurement conditions, and iv) low signal-to-noise ratio (SNR). Laboratory spectroscopy has now become a routine method to estimate SOC and other soil parameters. The use of proximal (Nawar and Mouazen, 2017) or remote sensing (Melendez-Pastor *et al.*, 2008; Stevens *et al.*, 2010; Castaldi *et al.*, 2014) could be very useful to provide more information on soil spatial variability at the field or even regional scale. Satellite data are very attractive because of the large spatial coverage and short revisit time, which results in the availability of a larger number of images over the same area. The use of remote sensing data for SOC estimation, despite some promising results obtained with Sentinel-2 multispectral broad-bands (Castaldi *et al.*, 2019), is currently hampered by the lack of suitable hyperspectral sensors mounted on the satellite platforms (Kruse, Boardman and Huntington, 2003; Casa *et al.*, 2013; Castaldi *et al.*, 2014). Within a few years, six satellites equipped with hyperspectral sensors will be launched (Guanter *et al.*, 2015; Pignatti *et al.*, 2015) and the future

hyperspectral imagers could provide more reliable data for soil spectroscopy applications. However, the issue related to the low spatial resolution of remote data remains unresolved: most of the current and new satellite sensors have a spatial resolution (10–30 m) that could not allow a sufficient explanation of the short-range variability that characterizes some soil variables, especially if the objective is soil mapping for precision farming. Moreover, fixed revisit times are not optimal for an appropriate temporal coverage, due to the influence of cloud cover, or when dry and bare soil conditions are required. While the spatial resolution of airborne sensors is higher (2–5 m), the high operational costs do not generally allow multi-temporal data to be obtained, which are often necessary to increase the likelihood of collecting remote sensing soil data in an optimal condition, i.e., bare, without harvest residues, low roughness, and low soil moisture (Itten *et al.*, 2008).

The recent development of Unmanned Aircraft Systems (UAS) (Colomina and Molina, 2014; Eltner and Schneider, 2015) and lightweight spectrophotometers (Soriano-Disla *et al.*, 2017) has allowed the assessment of the spatial and temporal variability of soil properties at a high resolution (< 1 m) and at relatively low costs. The advantages in terms of cost, flexibility, and spatial/temporal resolution, compared to aerial and satellite surveys, have been discussed in detail (Matese *et al.*, 2015; Aldana-Jague *et al.*, 2016). The new generation of hyper-/multi-spectral sensors that have become available during the last few years provides new opportunities for soil science and mapping (Ben-Dor, 2012); UAS-based sensing may provide a very attractive solution for research, particularly where high-resolution spatial data is needed (Soriano-Disla *et al.*, 2017).

The technological push toward smaller sensors with a better performance is mainly implemented for precision farming applications with a strong focus on crop performance (Zhang and Kovacs, 2012; Castaldi *et al.*, 2016; Nebiker *et al.*, 2016). At present, the use of UAS-based applications in soil science is still in an early stage. To our knowledge, only a few authors have dealt with UAS-based multispectral imaging for soil property estimation (e.g., Zhang and Kovacs, 2012; Gilliot *et al.*, 2017; Soriano-Disla *et al.*, 2017), and we are not aware of any applications of hyperspectral UAS systems for predicting soil properties.

Most authors that deal with remote or UAS data directly calibrate the sensor signal of a limited number of pixels, i.e., they collect soil samples within bare fields, measure the soil property in the laboratory, and calibrate a

multivariate model linking the measured soil property to the spectra extracted from the pixel at its sampling point (Mulder *et al.*, 2011). Wider applicable estimation models could be calibrated by exploiting existing national or continental or soil spectral libraries (Tóth, Jones and Montanarella, 2013; Viscarra Rossel *et al.*, 2016). Recently, Castaldi et al. (Castaldi *et al.*, 2018) used the pan European LUCAS topsoil database (Tóth, Jones and Montanarella, 2013) to estimate SOC content without applying spectral transfer between the calibration and validation dataset, because both sets of spectra were acquired using the same instrument (FOSS XDS Rapid Content Analyzer; FOSS NIR Systems Inc, Laurel, MD, USA) and no differences between equivalent spectra were detected (Tóth, Jones and Montanarella, 2013). The pre-processing procedure (radiometric, geometric, and atmospheric correction) on airborne, satellite, and UAS images introduces uncertainty in the spectra, compromising the comparability of different campaigns and of remote spectra and spectra from soil libraries (Nouri *et al.*, 2017; Castaldi *et al.*, 2018). However, a shorter distance between the UAS sensor and soil surface may result in a more robust acquisition of soil spectra, relative to airborne or satellite sensors. A UAS equipped with an incoming sunlight sensor can also provide a reliable at the surface reflectance, in contrast to satellite or airborne sensors, where the reflectance is calculated using atmospheric correction models. These characteristics make UAS-based soil sensing particularly suitable for spatial continuous mapping.

Here, we present a pilot study to investigate the capabilities of a range of hyper- and multi-spectral sensors that can be mounted on UAS for SOC estimation. The main objective was to compare the influence of spectral resolution and range on SOC prediction accuracy when employing UAS-portable sensors in laboratory and outdoor conditions (where we explicitly consider changing illumination and atmospheric conditions and sensor distance). We acquired reflectance from soil samples at close range (from few cm to 2–3 m), in both laboratory and outdoor conditions, using a range of sensors mounted on a tripod. The performance of multivariate calibration models applied to the spectra acquired by two portable hyperspectral sensors (STS-VIS and STS-NIR from Ocean Optics), and two miniature multispectral cameras (Parrot Sequoia and Tetracam Mini-MCA6), was compared to those obtained with a high-end hyper-spectral sensor (ASD Fieldspec 3 FR). Finally, we analysed the transferability of the prediction models between different measurement setups.

## 2.2 Materials and Methods

The experimental design used in this study is summarized in the following flowchart (Figure 2.1). It includes data collection and pre-processing, a comparison of instrument performances, and an evaluation of model transferability.

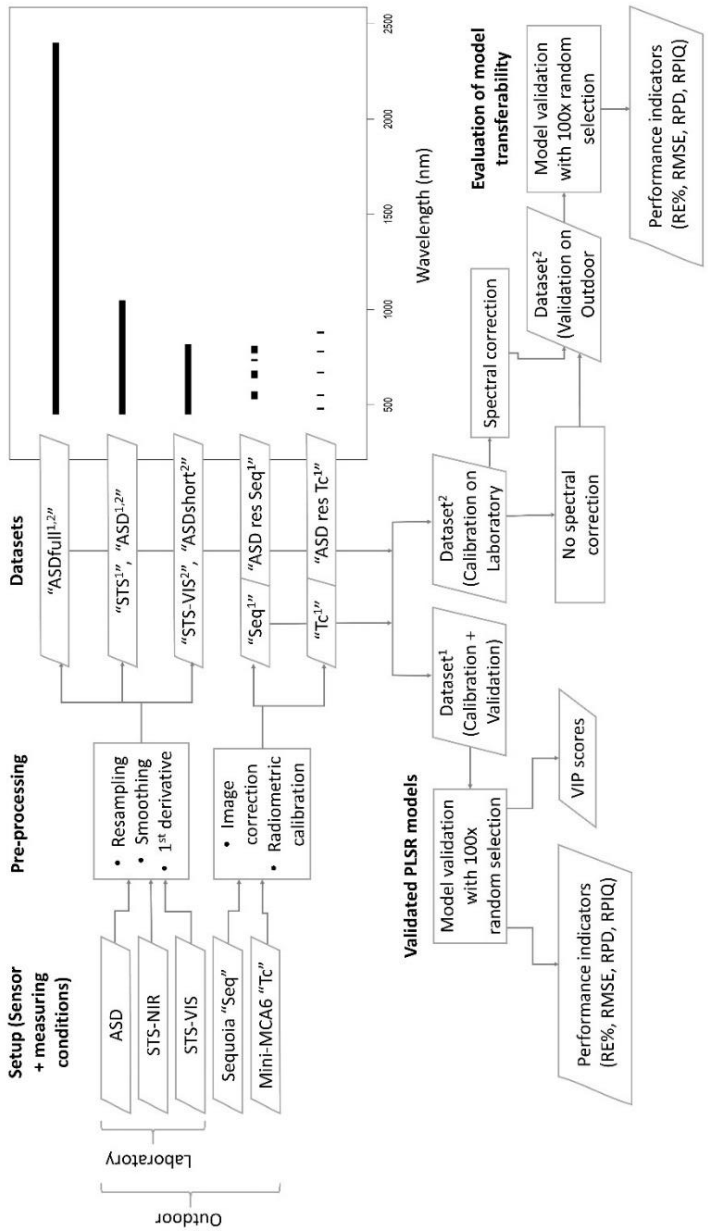


Figure 2.1. Flowchart of the experimental and analytical design.

### 2.2.1 Soil Datasets

In total, 96 soil samples from one of the Rothamsted long-term field experiments were used. The samples (0–2 cm) were taken from the Hoosfield Spring Barley Experiment, plots 72, 62, and 42 (Rothamsted Research, 2006; Aldana-Jague *et al.*, 2016). The soil on Hoosfield (Batcombe series; classified as a Chromic Luvisol (Bull *et al.*, 1998; Wrb, 2015)) is a flinty-silty-clay loam overlying clay with flints (Glendining *et al.*, 1997). The experimental design includes plots that have received different amounts and combinations of mineral fertilizers and organic manures, resulting in plots with very different SOC contents. The plots are ploughed to a depth of 23 cm each year. Consequently, the whole topsoil (0–23cm) layer is regularly mixed and the C content of the plough layer is relatively homogeneous. The SOC content of the 96 samples used in this study ranged between 8.2 and 46.7 $g \cdot kg^{-1}$ (mean = 16.56 $g \cdot kg^{-1}$, *sd* = 10.82 $g \cdot kg^{-1}$). Fresh soil samples were oven-dried (72h 60°C), ground, and sieved (< 2 mm with a sieving machine) prior to analysis. The total carbon content for all samples was obtained in a laboratory by dry combustion (using a VarioMAX CN Analyser Elementar GmbH, Germany). The inorganic carbon content of the soil was measured following the method of Sherrod et al. (Sherrod *et al.*, 2002). SOC was obtained by subtracting the inorganic carbon content from the total carbon content. Each sample was distributed on a petri dish (diameter 6.5 cm) for spectral data acquisition.

### 2.2.2 Sensor Equipment

The hyperspectral sensors employed were the STS-VIS and STS-NIR (Ocean Optics Inc., Dunedin, USA). The STS-VIS covers the wavelength range 350–800 nm, while the latter covers the range 650–1100 nm. Both sensors are compact (40 x 42 x 24 mm) and ultra-light (60 g) and provide light intensity values with an output optical resolution of 1.5 nm, resampled at a 0.45 nm data output resolution. Each single spectral acquisition with the STS instruments was performed with an integration time of 0.5 seconds.
The multispectral sensors employed were the Sequoia (Parrot Drones S.a.s., Paris, France) and Mini-MCA6 (Tetracam Inc., Chatsworth, USA). The Sequoia (Seq) measures 59 x 41 x 30 mm and weighs 72 g. It is a camera equipped with five imaging sensors: one for common RGB images and the other four for spectral bands centred at 550, 660, 735, and 790 nm wavelengths, with a width of 40, 40, 10, and 40 nm respectively. The field of view is 61.9 x 48.5 deg and the image resolution is 1280 x 960 pixels. The Sequoia works in

combination with an incident light sensor that provides an image-level correction factor for changing illumination conditions during image acquisition. The Mini-MCA6 (Tc) measures 134 × 93 × 78 mm and weighs 1080 g. It can be customized with a series of band-pass filters. We selected six lenses to filter six spectral windows, centred at 480, 550, 670, 780, 880, and 1000 nm wavelengths, with a width of 10 nm. Nevertheless, only the first five windows were used in this experiment (the window at 1000 nm was malfunctioning). The field of view of the camera is 38.3 × 31.0 deg, while the image resolution is 1280 x 1024 pixels.

The sensor used as the reference was an ASD Fieldspec 3 FR spectro-radiometer sensor (Analytical Spectral Devices Inc., Boulder, CO, USA) that provides single-spot light intensity data in the vis-NIR-SWIR region (350–2500 nm) with an optical resolution of 3 nm in the 350–1000 nm region and 10 nm for the 1000–2500 nm region, resampled at a 1 nm data output resolution. Each single spectral acquisition with the ASD instruments was performed with an integration time of 5.4 seconds.

All sensors and characteristics considered in this study are summarized in Table 2.1.

Table 2.1. Spectral resolution of the sensors used in this study.

| Instrument | Type | Wavelength Range (nm) | Output Resolution (nm) | Spectral Windows (nm) |
|---|---|---|---|---|
| ASD | hyperspectral | 350–2500 | 1 | / |
| STS-VIS | hyperspectral | 350–800 | 0.45 | / |
| STS-NIR | hyperspectral | 650–1100 | 0.45 | / |
| Sequoia | multispectral | / | / | 550 ± 20, 660 ± 20, 735 ± 5, 790 ± 20 |
| Mini-MCA6 | multispectral | / | / | 480 ± 5, 550 ± 5, 670 ± 5, 780 ± 5, 880 ± 5, 1000 ± 5 |

### 2.2.3 Spectral Measurements

Radiometric calibration was performed on all raw data acquired from the hyperspectral and multispectral sensors to obtain reflectance data. For the hyperspectral sensors (ASD and STS), the process involved the spectral measurement of a Spectralon white reference surface. Conversion to reflectance was automatically managed by the acquisition software (RS$^3$

software from ASD, OceanView software from OceanOptics). This calibration was repeated every six samples. Radiometric calibration and image correction for the Sequoia were performed by taking a picture of a calibration panel (Parrot Sequoia Calibration Target) and then post-processing the images following the procedure described on the manufacturer's website (Micasens Support, 2021), using the software R (R Core Team, 2021). Radiometric calibration and image correction for the Mini-MCA6 were performed by taking a picture of the Sequoia calibration panel and following the procedure described in Aldana-Jague et al. (Aldana-Jague *et al.*, 2016), using the software R.

The spectral measurements of the soil samples were carried out both in laboratory and outdoor conditions. Hyperspectral data with ASD, STS-VIS, and STS-NIR were acquired in both setups, while multispectral acquisitions could only be made outdoors:

- Laboratory setup ("Lab" dataset): all samples were scanned once, by the ASD and the STS sensors, using the ASD contact probe, which is equipped with its own light source (100 W halogen reflectorized lamp), and that allows for a spot size of 10mm of diameter. Measures were carried out with the probe in contact with the soil sample, in a dark room to minimize sources of disturbance (Figure 2.2, left).
- Outdoor setup ("Out" dataset): all samples were scanned once, in an open area, to minimize reflection from vertical objects in the surroundings, with stable, clear-sky, natural sunlight conditions for the whole duration of the measurements. In the ASD and STS cases, the sensor head was set at a 10 cm height above the samples, at the nadir position, providing a measuring spot size of 4.4 cm of diameter (Figure 2.2**,** right). In the cameras cases, the pictures were taken from a low altitude (ca. 2 m) in the nadir position above the samples, resulting in c. 35-40 pixels/sample.



Figure 2.2. The experiment setup in laboratory (left) and outdoor (right) conditions.

### 2.2.4 Comparison between Measurement Setups

All STS–VIS and STS–NIR spectra were resampled to match the ASD output resolution of 1 nm. They were then merged in a single continuous spectrum in the vis-NIR range 450–1050 nm (named "STS" dataset), applying a splice interpolation on the common spectral window to correct for the step between the different sensors. Bandwidths below 450 nm and beyond 1050 nm were removed to eliminate areas with excessive signal noise. ASD spectra were both used in their full spectral range ("ASDfull" dataset, in the 450–2400 nm vis-NIR-SWIR range, after removing the noisy bands) and cut to the same range of the "STS" ("ASD" dataset) to allow for a comparison. For the "ASDfull" spectra, the noisy bands in the water absorption intervals (1350–1450 and 1800–1950 nm) were removed, in accordance with the ranges used by Castaldi et al (Castaldi *et al.*, 2016). Both "ASD" and "STS" spectra acquired in outdoor conditions ("Out" dataset) were smoothed with a Savitzky-Golay transformation (Savitzky and Golay, 1964) using a second-order polynomial fit. Then, to facilitate SOC modelling through PLSR, data transformation with 1$^{st}$ derivative (1D), continuum removal (cr), and Standard Normal Variate (SNV) were applied and tested. To evaluate the performance of the cameras (respectively "Seq" and "Tc" datasets for Sequoia and Mini-MCA6 cameras), four sub-datasets were extracted from the laboratory and outdoor "ASD" dataset, by resampling to match the spectral windows of Sequoia and Mini-MCA6 (respectively "ASD res Seq" and "ASD res Tc", for laboratory and outdoor). The data processing was carried out in the software R, using the "prospectr" package (Stevens and Ramirez-Lopez, 2013).

As a preliminary analysis, Pearson's correlation between SOC and wavelengths was calculated on the full spectral range for both "ASD" laboratory and outdoor setups. Two parameters were calculated in four ranges (450–1050, 1051–1999, 2000–2400, and 450–2400 nm): i) the RMScorr and ii) the percentage of bands with a correlation significantly different from 0 ($p < 0.05$).

PLSR models were then developed for all groups, i.e., combinations of conditions (Lab and Out), instruments, and data transformations, using the R package "pls" (Bjørn-Helge and Wehrens, 2007). First, the skewness of the SOC distribution of the calibration datasets was reduced by using a logarithmic transformation. For each group, a PLSR model with up to 25 latent variables and "Leave-one-out" cross validation was built, with the aim of selecting the optimal number of latent variables. The best PLSR model

within each group was selected based on the number of latent variables (PLSR components) that provided the first local minimum in the relation between the cross-validated RMSE and the number of components. To evaluate the robustness of the models, a validation was then performed, for each group, splitting the data into a calibration and validation dataset (70% and 30%, respectively), with random selection, for 100 repetitions. The performance of the models was tested on the validation datasets using the mean of 100 simulations of the following metrics: i) MRE % (Equation 2.1), ii) RMSE (Equation 2.2), iii) $R^2$ (Equation 2.3), iv) RPD (Equation 2.4), and v) RPIQ (Equation 2.5) (Bellon-Maurel *et al.*, 2010), defined as following:

$$MRE\% = \frac{\sum_{i=1}^{n}(\hat{y}_i - y_i)}{\bar{y}} \cdot 100 \quad (2.1)$$

$$RMSE = \sqrt{\frac{\sum_{i=1}^{n}(\hat{y}_i - y_i)^2}{n}} \quad (2.2)$$

$$R^2 = \frac{\sum_{i=1}^{n}(\hat{y}_i - \bar{y})^2}{\sum_{i=1}^{n}(y_i - \bar{y})^2} \quad (2.3)$$

$$RPD = \frac{sd}{RMSE} \quad (2.4)$$

$$RPIQ = \frac{iqr}{RMSE} \quad (2.5)$$

where $\hat{y}$ = predicted value, $\bar{y}$ = mean observed value, y = observed values, n = number of samples (with i = 1, 2, … , n), *sd* is the standard deviation of the observed values, and *iqr* is the inter-quantile range of the observed values. The significance of the differences between the means of performance indicators, in terms of RMSE, RPD, and RPIQ, was evaluated using a *t* test for all the comparisons hereby discussed. Furthermore, the importance of the wavelengths relevant for SOC estimation according to the PLSR was identified by the VIP index (Variable Importance for the Projection) (Wold, Sjöström and Eriksson, 2001). A VIP > 1 was considered as a criterion for the detection of relevant bands, following Chong & Jun (Chong and Jun, 2005).

### 2.2.5 Model Transferability between Measurement Setups

The dataset was used to test the stability of the spectral measurements collected by ASD and STS-VIS under different acquisition conditions, namely between the laboratory and outdoors. The tests concerned the STS-VIS measurements between 450 and 820 nm (“STS-VIS” dataset) and the ASD

data at three spectral ranges: 450–2400 nm ("ASDfull" dataset), 450–1100 nm ("ASD" dataset), and 450–820 nm ("ASDshort" dataset). The dataset was randomly split 100 times in a calibration (75%) and validation (25%) dataset for each test. The SOC values and the laboratory spectral data of each calibration dataset were then used to build a PLSR model, which was tested on the validation dataset composed of spectral data acquired in outdoor conditions. We also validated the PLSR models obtained from both ASD and STS-VIS instruments, both under laboratory and outdoor conditions (450–820 nm), on data acquired with the other sensor. For example, the calibration dataset derived from the ASD-VIS laboratory spectra was used to validate the STS outdoor dataset. All the above-mentioned SOC calibration models were also applied before and after the normalization of the spectra using an internal soil standard (Kopačková and Ben-Dor, 2016). For this purpose, one Australian white sand sample (named Lucky bay) was used as a soil standard. This sand was chosen because: *i*) the size and shape of the grains are similar to natural soil, *ii*) reiterated spectral measurements are stable across the whole spectral region, *iii*) spectral features are negligible, and *iv*) the sample is stable because it consists almost entirely of quartz (Pimstein, Notesco and Ben-Dor, 2011). The Lucky Bay sand sample was scanned using ASD and STS-VIS spectroradiometers, both under laboratory and outdoor conditions. All the sand spectral data were acquired the same day of the soil measurements and using the same protocol described in the previous section. The sand spectra acquired with ASD and STS-VIS (secondary instruments) were compared with the benchmark spectrum, namely the Lucky Bay spectrum acquired with an ASD spectroradiometer (primary instrument) in the Commonwealth Scientific and Industrial Research Organisation (CSIRO) laboratory. The soil spectral measurements were corrected with a correction factor based on the following Equation (2.6):

$$C_\lambda = 1 - \left( \frac{\rho_{sl,\lambda} - \rho_{be,\lambda}}{\rho_{sl,\lambda}} \right) \quad (2.6)$$

where λ is a given wavelength, $\rho_{sl,\lambda}$ is the reflectance of the Lucky Bay sand measured with one of the secondary instruments in laboratory or outdoor conditions, and $\rho_{be,\lambda}$ is the Lucky Bay sand reflectance acquired at the CSIRO laboratory (benchmark spectrum).

Then, the correction factor $C_\lambda$ is applied to the original soil spectra acquired with the secondary instrument, $R_{so,\lambda}$, obtaining the corrected spectra $R_{sc,\lambda}$ , as in Equation (2.7):

$$R_{sc,\lambda} = R_{so,\lambda} \cdot C_{\lambda} \quad (2.7)$$

The average statistic values (RE%, RMSE, RPD, RPIQ) of the 100 iterations of each test were computed before and after the application of the correction factor based on the Lucky Bay sand. The significance of the differences between the means of performance indicators, in terms of RMSE, RPD, and RPIQ, was evaluated using a *t* test for all the comparisons hereby discussed.

## 2.3 Results

### 2.3.1 Validated PLSR Models

The correlation plot (Figure 2.3) between SOC and spectral wavelengths based on the "ASDfull" laboratory dataset showed strongly correlated bands in the range 500–850 nm, and an average RMScorr of 0.53 $g \cdot kg^{-1}$ for the 450-1050 nm spectral region. In total, 78% of wavelengths were significantly correlated to SOC (Table 2.2). Almost the same result was obtained when taking into account the full spectrum, with an average RMScorr of 0.48 $g \cdot kg^{-1}$ and 77% of bands significantly correlated; nonetheless, the range between 1000 and 2000 nm was characterized by overall poorly correlated bands (average RMScorr = 0.32 $g \cdot kg^{-1}$), while only the range between 2000 and 2400 nm showed good correlation values (average RMScorr = 0.67 $g \cdot kg^{-1}$, with 93% of bands significantly correlated). For outdoor conditions, the scores for the 450-1050 nm range were just slightly lower than those obtained under laboratory conditions, with an average RMScorr of 0.49 $g \cdot kg^{-1}$ and 70% of wavelengths significantly correlated. On the other hand, the average RMScorr dropped consistently both in the 1050–1999 (RMScorr = 0.16 $g \cdot kg^{-1}$, 32% of wavelengths correlated) and 2000–2400 nm ranges (RMScorr = 0.19 $g \cdot kg^{-1}$, 37% of wavelengths correlated).

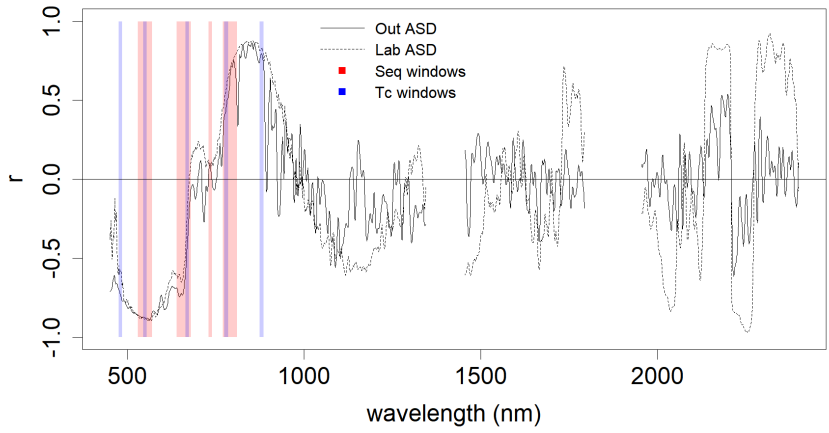


Figure 2.3. Pearson's correlation plot between SOC and spectral wavelengths for the "ASDfull" laboratory (dashed line) and outdoor (solid line) setups. The spectral windows of the Sequoia (Seq) are highlighted in red and Mini-MCA6 (Tc) in blue.

Table 2.2. RMScorr of the four spectral regions for the "ASDfull" laboratory and outdoor setups.

| | | Spectral range (nm) | | | |
|---|---|---|---|---|---|
| **Setup** | | **450–1050** | **1051–1999** | **2000–2400** | **450–2400** |
| Laboratory | RMScorr | 0.53 | 0.32 | 0.67 | 0.48 |
| | % $p < 0.05$ | 78 | 67 | 93 | 77 |
| Outdoor | RMScorr | 0.49 | 0.16 | 0.19 | 0.28 |
| | % $p < 0.05$ | 70 | 32 | 37 | 47 |

The performances of PLSR models built from the "ASD" and "ASDfull" data were first compared to evaluate the possibility of modelling SOC content from the vis-NIR window only (Table 2.3, Figure 2.4 and Figure 2.5). D1 transformation provided the best results in comparison to cr and SNV. Therefore, only the first transformation method was used for the comparisons. Differences in terms of RMSE (2.2 and 2.1 $g \cdot kg^{-1}$, respectively), RPD (5.3 and 5.4, respectively), and RPIQ (6.2 and 6.9, respectively) were not significant for the laboratory dataset ($p > 0.05$). Under outdoor conditions, however, the use of the full spectral range caused a significant decrease in performances, i.e., the RMSE increased from 2.6 to 3.9, the RPD decreased from 4.2 to 2.9, and the RPIQ decreased from 4.9 to 3.6.

When comparing the "ASD" and the "STS", the latter performed ~30% worse for all indices in the laboratory setup (RMSE = 2.9 $g \cdot kg^{-1}$, RPD = 3.9, RPIQ =

4.5) and even less in the field setup (RMSE = 4.2 g·kg$^{-1}$, RPD = 2.6 and RPIQ = 3; Table 2.3, Figure 2.4 and Figure 2.5). For the Sequoia and Mini-MCA6 multispectral cameras, we obtained an RMSE of 2.7 and 3.3 g·kg$^{-1}$ and an RPD of 4.2 and 3.5, respectively. These results were comparable to the performances of the "ASD", using the vis-NIR spectral range only, under outdoor conditions. Furthermore, it should be noted that the cameras outperformed the "STS" when used outdoors. We also compared the performance of the cameras and of the laboratory and outdoor "ASD" data resampled on cameras' spectral windows, to test the effects of size and position of these windows. Laboratory "ASD res Seq" gave an RMSE of 2.4 g·kg$^{-1}$ and an RPD of 4.7, and laboratory "ASD res Tc" gave an RMSE of 2.6 g·kg$^{-1}$ and RPD of 4.4. The outdoor "ASD" data resampled on the same windows gave results which were not statistically different from the laboratory resampling ($p > 0.05$). The average bias estimated with the RE% was low for all models (Table 2.3). The plots with the observed versus predicted SOC values from all models used in the comparison of the measuring setups are presented in Appendix A (Figure A 1, a-l).

Table 2.3. RE%, RMSE (g·kg$^{-1}$), RPD, RPIQ, and $R^2$ of the validation PLSR performances (data reported represents the mean value over 100 repetitions) for all the instruments and setups: "ASD", "ASDfull", "STS", "ASD res Seq", "ASD res Tc", "Seq", and "Tc". The number of latent variables (n° comp) used in each model is also reported.

| | Laboratory setup | | | | | | Outdoor setup | | | | | |
|---|---|---|---|---|---|---|---|---|---|---|---|---|
| **Dataset** | **n° comp** | **MRE%** | **RMSE** | **RPD** | **RPIQ** | **$R^2$** | **n° comp** | **MRE%** | **RMSE** | **RPD** | **RPIQ** | **$R^2$** |
| "ASD" | 3 | 0.51 | 2.2 | 5.3 | 6.2 | 0.96 | 5 | 0.8 | 2.6 | 4.2 | 4.9 | 0.94 |
| "ASDfull" | 3 | 1 | 2.1 | 5.4 | 6.9 | 0.96 | 7 | 2.7 | 3.9 | 2.9 | 3.6 | 0.89 |
| "STS" | 3 | 2.4 | 2.9 | 3.9 | 4.5 | 0.94 | 6 | 3.1 | 4.2 | 2.6 | 3.0 | 0.85 |
| "ASD res Seq" | 4 | 0.48 | 2.4 | 4.7 | 5.1 | 0.95 | 4 | 0.45 | 2.5 | 4.4 | 5.6 | 0.95 |
| "ASD res Tc" | 5 | 0.17 | 2.6 | 4.4 | 5.3 | 0.95 | 5 | 0.79 | 2.5 | 4.5 | 5.2 | 0.95 |
| "Sequoia" | / | / | / | / | / | / | 4 | 0.82 | 2.7 | 4.2 | 5.1 | 0.94 |
| "Tc" | / | / | / | / | / | / | 5 | 2.2 | 3.3 | 3.5 | 4.5 | 0.93 |

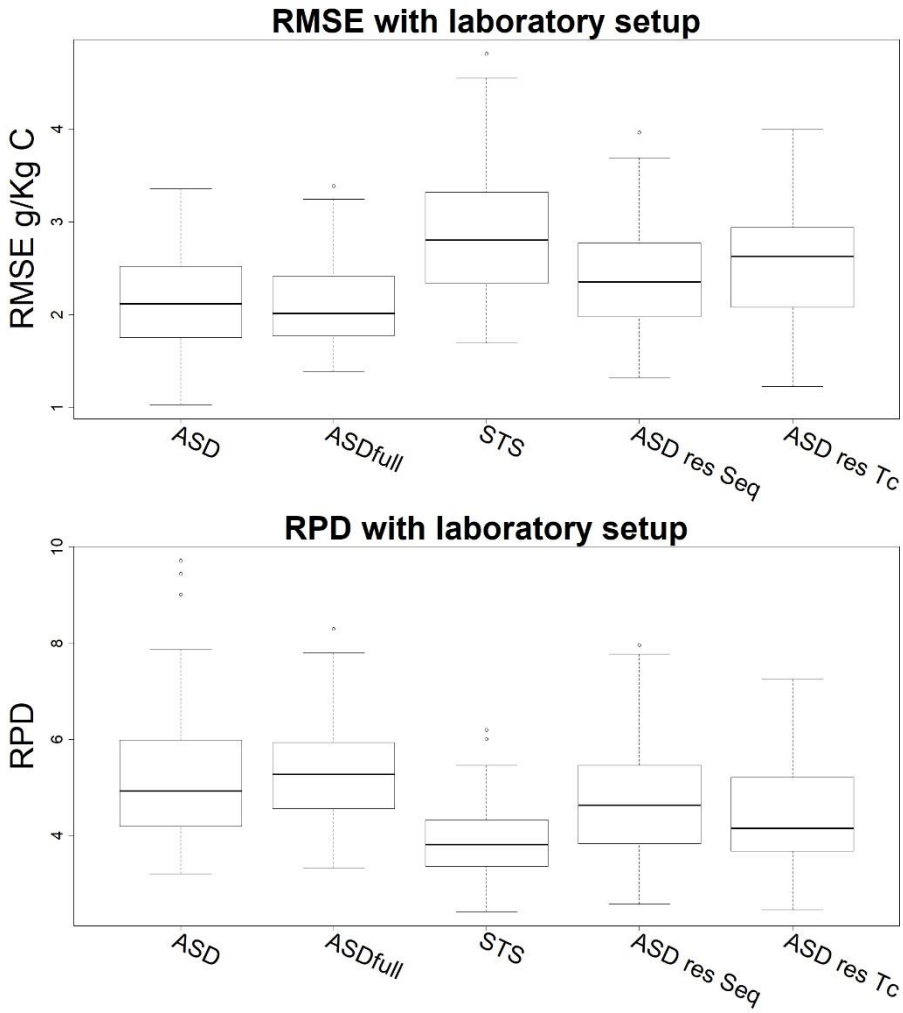


Figure 2.4. RMSE and RPD from the validation of the models built under laboratory conditions: “ASD”, “ASDfull”, “STS”, “ASD res Seq”, and “ASD res Tc”.

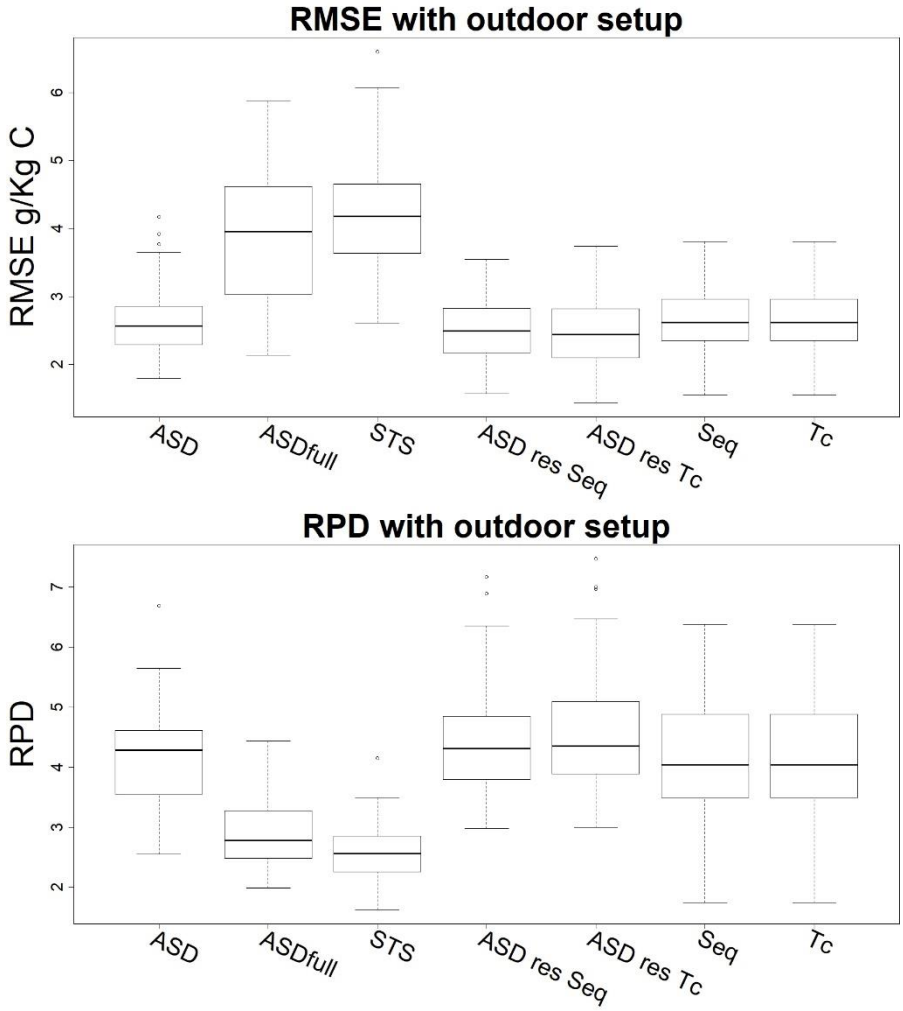


Figure 2.5. RMSE and RPD from the validation of the models built under outdoor conditions: “ASD”, “ASDfull”, “STS”, “ASD res Seq”, “ASD res Tc”, “Seq”, and “Tc”.

The VIP scores calculated for both the “ASD” laboratory and outdoor setups showed a similar trend in the whole vis-NIR range, highlighting a large single region of interest (VIP > 1) for the PLSR models in the 500–600 nm range (Figure 2.6). The models built from the cameras were, on the contrary, exploiting all spectral windows except for the one centred on the 550 nm region.

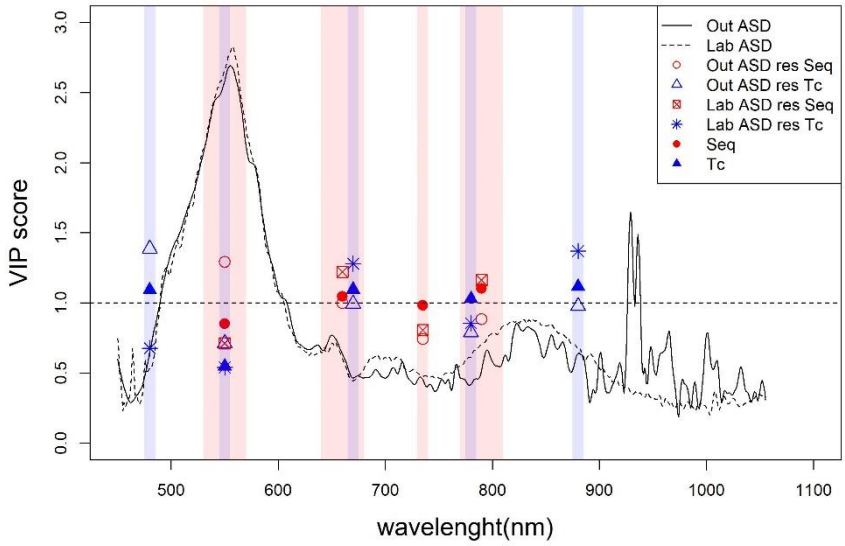


Figure 2.6. VIP scores in the vis-NIR range from the PLSR models: laboratory and outdoor "ASD", laboratory and outdoor "ASD res Seq" and "ASD res Tc", and outdoor "Seq" and "Tc".

### 2.3.2 Evaluation of Model Transferability

The models that were calibrated with the laboratory ASD data, and without applying the correction factor $C_\lambda$, were successfully validated with outdoor ASD spectra for all spectral ranges (Table 2.4). The best estimation accuracies were obtained with a reduced range ("ASDshort" and "ASD"); in these cases, the RPD was higher than 3 and RMSE was 3.1 g·kg$^{-1}$ for the 450–1100 nm range and 3.4 g·kg$^{-1}$ for the 450–820 nm range. The use of the full 450 – 2400 nm spectrum data ("ASDfull") degraded the estimation accuracy (RMSE = 4.6 g·kg$^{-1}$; RPD = 2.5; RPIQ = 3.0). After the application of the correction factor, the statistics did not improve for any of the ASD data, while the use of the $C_\lambda$ allowed us to align the "STS-VIS" laboratory and "STS-VIS" outdoor spectra. In fact, the RPD after the correction increased from 1.4 to 2.9 (Table 2.4). The models calibrated using "ASD" laboratory data were successfully tested on "STS-VIS" outdoor data (RMSE = 4.4 g·kg$^{-1}$; RPD = 2.5; RPIQ = 2.9), and the correction factor allowed us to slightly improve the accuracy.

Table 2.4. RMSE (g·kg$^{-1}$), RPD, RPIQ, and $R^2$ of PLSR performances of transferred models, both with and without the application of a spectral correction using an internal soil standard.

| Dataset | | No spectral correction | | | | | Spectral correction | | | | |
|---|---|---|---|---|---|---|---|---|---|---|---|
| Calibration | Validation | RE% | RMSE | RPD | RPIQ | $R^2$ | RE% | RMSE | RPD | RPIQ | $R^2$ |
| Lab "ASDshort" | Out "ASDshort" | –0.4 | 3.4 | 3.2 | 4.0 | 0.9 | 0.6 | 3.4 | 3.2 | 3.8 | 0.9 |
| Lab "ASD" | Out "ASD" | −5.3 | 3.1 | 3.5 | 4.3 | 0.9 | -18.3 | 5.7 | 2.3 | 2.5 | 0.7 |
| Lab "ASDfull" | Out "ASDfull" | −24.4 | 4.6 | 2.5 | 3.0 | 0.8 | 20.9 | 4.7 | 2.4 | 2.6 | 0.8 |
| Lab "STS-VIS" | Out "STS-VIS" | 34.7 | 7.8 | 1.4 | 1.6 | 0.4 | 14.6 | 3.7 | 2.9 | 3.2 | 0.9 |
| Lab "ASDshort" | Out "STS-VIS" | 11.5 | 4.4 | 2.5 | 2.9 | 0.8 | -7.8 | 4.2 | 2.6 | 3.1 | 0.8 |

## 2.4 Discussion

The use of spectral sensors that can be mounted on UAS-based platforms for the analysis of soil properties requires optimization. First, UAS payload and battery limitations typically require small and very light sensors. Secondly, their detection capabilities have to be optimized, which is related to the spectral features of the target variable and requires a priori knowledge of the spectral characteristics of all sensed objects for successful applications of any quantitative analysis (Ben Dor, 1997).

The spectral features related to SOC are located along many spectral regions, due to the heterogeneity of its components. Some important features were detected in the NIR and SWIR regions (Viscarra Rossel *et al.*, 2006; Mouazen *et al.*, 2007; Grunwald, 2009; Stenberg *et al.*, 2010; Castaldi *et al.*, 2016). These are mainly related to specific chemical bonds between carbon and hydrogen (C-H) at 1340–1380 nm, the amide nitrogen-hydrogen bond (N-H), and the bond between Oxygen and Hydrogen in the hydroxyl group, both at 1860–1900 nm. Lignin and cellulose influence the reflectance, respectively, between 1600–1800 nm and around 2100 nm (Bartholomeus *et al.*, 2008). Other features linked to cellulose, lignin, and starch can be found around 2300 nm, close to features related to phenolic, amide, and aliphatic groups (Ben Dor, 1997). Important correlations between reflectance and organic carbon content were also detected in the VIS region. Although these strong correlation values in the VIS region were mainly reported to be due to the direct relationship between the soil colour and the organic matter abundance (Bartholomeus *et al.*, 2008; Castaldi *et al.*, 2016), specific wavelengths and spectral regions were identified. Strong correlations with SOC were found in the VIS region between 550 and 700 nm (Galvao and Vitorello, 1998), between 526 and 587 nm (Melendez-Pastor *et al.*, 2008), and in the 600–800 nm range (Conforti *et al.*, 2013). Strong correlation

between reflectance and SOC was also found within narrower ranges centred at 490 (Mouazen *et al.*, 2007), 660 nm ('The contribution of diffuse reflectance spectroscopy to soil organic carbon analysis : from laboratory to airborne', no date; Bartholomeus *et al.*, 2008; A Stevens *et al.*, 2013), and 750 nm (Ge *et al.*, 2011). Melendez-Pastor et al. (Melendez-Pastor *et al.*, 2008) have already pointed out that the cost-effectiveness of field spectro-radiometers for SOC detection could benefit from their focus on the VIS range and our findings are in line with this statement.

Starting from the analysis of laboratory ASD data, we found regions with a strong average correlation in the 500–850 nm and 2000–2400 nm ranges, but our PLSR models showed that the differences in performance between vis-NIR and full spectrum (vis-NIR-SWIR) datasets are not significant ($p > 0.05$) in terms of SOC prediction accuracy. Since the range between 1050 and 1999 nm was characterized by overall poorly correlated bands, it is therefore possible that this portion of the spectrum is not informative for SOC and its inclusion in PLSR modelling deteriorates overall performances, at least for the specific soil and SOC range we used in this study. When moving from laboratory to outdoor conditions, the model performances decreased when including the SWIR (Table 2.3, Figure 2.4 and Figure 2.5). Indeed, while the correlation for the vis-NIR range was just slightly lower than the one observed in the laboratory, they dropped both in the 1050–1999 and 2000–2400 nm ranges. This may be due to the lower signal-to-noise ratio of the ASD under outdoor conditions, especially in the 2000–2400 nm range (Figure 2.7).

The SOC prediction accuracy obtained with the "STS" dataset was lower than that obtained with the "ASD" data. This was most probably due to the presence of important noise in the wavelengths at the start (< 500 nm) and at the end (>900 nm) of its spectrum, especially for the outdoor setup (Figure 2.7, in the zoomed windows). This noise was probably due to the shorter integration time used for data acquisition with the STS instruments (0.5 sec), to simulate "in-flight" operational conditions, compared to the ASD one (5.4 sec).

The Sequoia and Mini-MCA6 cameras yielded good performances, possibly due to the fact that some of their spectral windows, especially those centred at 550, 660, and 670 nm, match portions of the spectrum that are strongly correlated to SOC (Figure 2.3). In particular, the Sequoia-based model yielded results similar to those of the ASD in outdoor conditions. The hyperspectral and multispectral resolutions influenced the VIP values in different ways: on

the one hand, hyperspectral data exploited the 500-600 nm range that appears to be a very informative region, probably for its slope, (e.g. Bartholomeus *et al.*, 2008). On the other hand, multispectral data mainly exploited the other windows up to 880 nm (Figure 2.6). The narrow bands used in the Sequoia camera, centred at 660 and 790 nm, cover a spectral range more correlated to SOC than the narrow bands available for our Mini-MCA6 in the same regions (Figure 2.3). This is supported by the observation that the PLSR performances obtained using the outdoor ASD spectra resampled on the cameras' windows showed better results when using the Sequoia narrow bands than the Mini-MCA6 ones (Table 2.3).

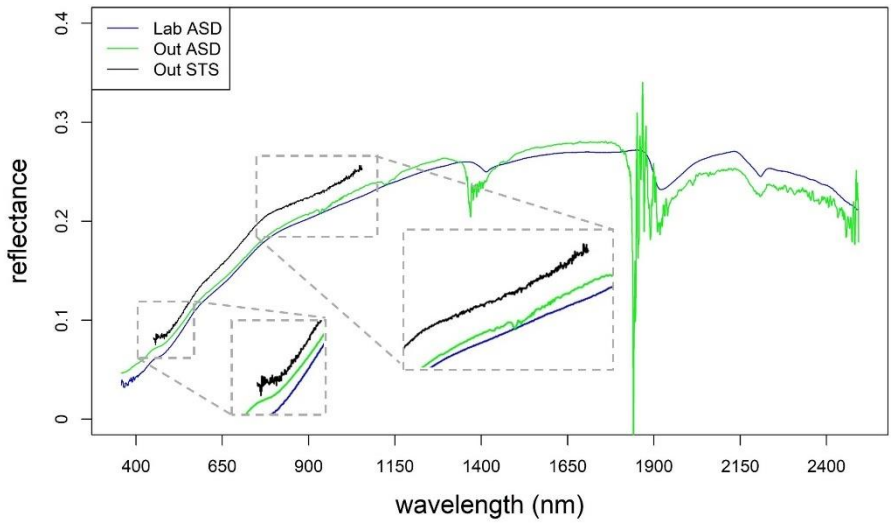


Figure 2.7. Example of soil sample spectrum as registered by the ASD in laboratory conditions (in blue) and by ASD and STS in outdoor conditions (green and black, respectively). Head and tail of the STS signal are zoomed to highlight the higher noise, as compared to the ASD signals.

The results from the comparison of the validation sets provided some important information on the contribution of different spectral regions and resolutions, and on the influence of setup conditions on SOC prediction accuracy. Nevertheless, it should be noted that the outdoor setup was not fully representing real field conditions. Although the outdoor measurements were made under conditions similar to those in the field (natural sunlight, moist air, and sensor distance), the effects of soil roughness and soil moisture were eliminated in this study. Furthermore, the sensors were not mounted on a drone, but were installed on a tripod, to facilitate the scanning of a range

of soil samples with different sensors. In addition, our tests were performed on soils collected from several plots with different SOC contents within a single field experiment and may not fully represent typical ranges of SOC that can be found in real-life conditions. Although new research should be carried out to prove the effectiveness of mapping SOC using UAS-based data under real flight conditions (Aldana-Jague *et al.*, 2016), the information obtained here can be used to understand the potential and limitations of different sensor setups .

Another key problem related to SOC mapping is the extrapolation of these empirical models to areas that differ from the ones where the calibration was obtained. This is often very difficult, costly, or just impossible. Consequently, the collection of a specific dataset for each investigated area is necessary in order to obtain an accurate quantitative estimation of the target soil property. Nevertheless, the collection of a calibration dataset requires an extensive sampling and laboratory analysis. However, many large soil spectral libraries covering local to global scales (Panagos *et al.*, 2013; Viscarra Rossel *et al.*, 2016) already exist. Once the issue of the alignment between datasets is solved, they could be exploited to predict soil properties in another dataset. The alignment between laboratory spectra acquired using two different protocols or instruments is a common practice in soil spectroscopy (Fearn, 2001). This goal can be achieved by applying a spectral transfer function, which is obtained by scanning some soil samples using both instruments. An alternative practice is the alignment by means of an internal soil standard (Kopačková and Ben-Dor, 2016). These techniques could be very attractive to apply predictive models, calibrated with laboratory spectra, to proximal and remote sensing data. However, their use is mainly hampered by the uncertainty of the atmospheric correction, which affects the spectral responses from remote sensing data (Castaldi *et al.*, 2018). For this reason, only a few studies have dealt with the transfer between laboratory and remote spectra (Nouri *et al.*, 2017; Castaldi *et al.*, 2018). Obviously, reducing the distance between the sensor and soil could reduce the issues related to atmospheric correction and UAS-borne sensors could be used for this purpose; however, we are not aware of studies dealing with the alignment between laboratory and UAS spectral data. This is probably due to the large differences between the spectral resolution of laboratory instruments and UAS borne cameras/sensors. Although many light hyperspectral sensors are currently available, their performances for soil properties prediction are still poorly quantified. In this study, we tried to

validate laboratory PLSR models for outdoor spectra with and without the alignment by an internal soil standard. Our tests highlighted a good correspondence between the laboratory ASD and outdoor ASD spectra without spectral correction. The worst result with ASD data was obtained using the "ASDfull" range (450-2400 nm), and this is due to the important noise in the SWIR region of the outdoor measurements that increases the difference with the laboratory "ASDfull" (Figure 2.7). It should be noted that this was also visible in the correlations between reflectance and SOC (Figure 2.3). The main differences between outdoor ASD and laboratory ASD spectra are in the NIR-SWIR region, while in the VIS, the two spectra have very similar trends and values (Figure 2.7). The STS-VIS sensor showed a larger difference between laboratory and outdoor spectra, relative to the ASD. In fact, the performance statistics of the validation after the spectral correction consistently increased. However, the "STS-VIS" performance is still lower than the one obtained with the ASD for the same spectral range ("ASDshort" 450-820 nm). These results show that exploiting a predictive model calibrated with laboratory data to outdoor spectra obtained by the same instruments is feasible. However, it should be noted that for the "STS-VIS", a spectral correction was necessary. The differences between ASD and STS-VIS were mainly due to the high noise in the STS-VIS spectra, especially for the outdoor measurements (Figure 2.7). In addition, in this case, a satisfactory correspondence between the outputs of the two instruments can be observed (RPD = 2.5), and no significant improvement, in terms of prediction accuracy, was observed when applying $C_\lambda$.

## 2.5 Conclusions

The UAS-compatible hyperspectral sensors and multi-spectral cameras operating in the vis-NIR spectral range that were tested in this study are able to provide data with a sufficient quality for developing SOC prediction models in outdoor conditions. SOC prediction modelling based on the narrow bands of the two multispectral cameras (Parrot Sequoia and Tetracam Mini-MCA6) provided better performances than those obtained with the STS hyperspectral sensors. Furthermore, the model built on the Sequoia camera reached the same performance (RMSE = 2.7, RPD = 4.2) as the reference ASD instrument in outdoor conditions (RMSE = 2.6, RPD = 4.2). VIP scores of our PLSR models showed that: i) the spectral region between 500 and 600 nm contains most information for hyperspectral SOC modelling, and ii) the vis-NIR range up to about 900nm is exploited when using multispectral narrow

bands. Validation results indicate that the vis-NIR range alone may be sufficient for SOC prediction, at least for the conditions encountered in this study. Consequently, the implementation of small-form vis-NIR portable sensors in UAS systems could be a viable strategy to improve the effectiveness of SOC assessments. Moreover, we showed that it is possible to exploit predictive models calibrated with hyperspectral laboratory data on outdoor spectra obtained by the same portable instruments, applying a correction factor based on an internal soil standard. Together, this shows that UAS-based multispectral and hyperspectral sensors have the potential to estimate soil organic carbon on bare soils with an acceptable accuracy and at a much higher spatial and temporal resolution than existing methodologies.

# Chapter 3

# Towards mapping of soil crust using multispectral imaging

*The content of this chapter is based on the published article:*
*Crucil G., & Van Oost K. (2021). Towards mapping of soil crust using multispectral imaging. Sensors, 21(5), 1–19. https://doi.org/10.3390/s21051850*

## Abstract

Soil crusts and surface roughness are properties which are highly dynamic in both space and time that change in response to biotic processes, meteorological conditions, and farming operations. These factors, however, are difficult to quantify and are usually described using simplified expert-based classes. This hampers a clear identification of the controlling factors and their relation to soil erosion and sediment generation processes. The availability of new small portable multispectral cameras offers the potential to study soil surface dynamics at a high spatial and temporal resolution. The objective of this study was to analyse the relationship between soil crusting, represented by cumulative rainfall kinetic energy, and soil surface reflectance, as derived from vis-NIR multispectral imaging. We designed a series of rainfall-soil surface experiments to disentangle the effects of soil crusting on spectral reflectance factors from those related to surface micro-scale roughness. PLSR models were developed to predict both kinetic energy and roughness from multispectral images. We evaluated different roughness removal methods, which were based on the transformation of reflectance through Standard Normal Variate (SNV) and roughness thresholding using high resolution digital elevation models. Furthermore, we assigned the light scattering effect related to roughness in the multispectral spatial domain by calculating the inter-quantile range of the reflectance values in a kernel. Our experiments and workflow demonstrate that it is possible to model crust development, using rainfall kinetic energy as a proxy, from vis-NIR based multispectral imaging.

## 3.1 Introduction

The general introduction in Chapter 1.1 highlighted how there are still persistent issues in the reliability of runoff and soil loss estimates, which make modelling soil runoff/erosion and subsequently landscape management difficult. A long-standing challenge in the field has been indeed the observation that the cause of soil surface runoff is non-unique, i.e., the same apparent soil surface and rainfall conditions do not necessarily result in the same runoff and erosion rate. A literature review suggested that micro-scale properties of the first few centimetres of the soil surface strongly affects its infiltration capacity and erodibility. In particular, soil physical degradation from the changes in roughness and the development of soil crusts are important factors controlling the above-mentioned variability, particularly on fine-textured soils. Chapters 1.1.3 provided a summary of the complexity of the physico-chemical changes involved in soil crust development, its hydrological consequences, and its scientific description. It was shown that a major problem resides in the fact that soil crust and roughness are highly dynamic in both space and time in response to biotic processes, the energetic input of rainfall and/or farming operations. Even under laboratory conditions, or controlled field experiments, these factors are difficult to quantify. Therefore, one way to improve not only our mechanistic understanding of rainfall-runoff processes, but also erosion model performance, is to improve the accuracy and precision of model input data, using new sensor measurement methods, and to test how sensitive the model is to variations in input data(Thomsen *et al.*, 2015).

Chapter 1.1.4 provided a summary of the effectiveness of soil spectral analysis in the estimation of a wide range of soil properties. It showed, in particular, that the spectral properties of crusted soils were already the subject of several studies looking at specific spectral features, and this was also related to soil infiltration rates and cumulative rainfall kinetic energy. The recent advent of small portable sensors with multi-spectral capabilities now provide the means, the accuracy and the resolution to quantitatively and accurately assess spatial-temporal variability of soil conditions at different scales, especially if combined with low altitude flights with unmanned aerial systems (UAS) (Chapter 2 - Crucil *et al.*, 2019). These systems have the potential to present a better alternative to ground surveys, on one side, and satellite data on the other: they offer superior spatial and temporal resolution at a better time- resource- and cost- efficiency. In the

context of soil surface analysis, several studies of Croft et al. (Croft, Anderson and Kuhn, 2009, 2012, 2014) successfully developed and refined models of soil surface roughness using proximal hemispherical measurements of hyperspectral directional reflectance factors. Nonetheless, they recognized the difficulty of separating the contribution of soil variables like roughness, moisture, and organic carbon to soil reflectance factors, and the complexity that exists in attempting to retrieve them from optical remotely sensed data (Anderson and Croft, 2009). Elucidating the factors, as well their interactions, that shape the soil spectral signature is therefore critical. This is important in the context of developing predictive models of soil crust development suitable for proximal sensing applications and/or low altitude UAS flights.

The general objective of this study is to analyse the functional relationships between soil crusting and soil surface reflectance as derived from multispectral imaging and how this can be inferred from low-altitude UAS sensors. More specifically, we aim at disentangling the effects of soil surface roughness from those of crust development on spectral reflectance factors, by establishing and evaluating a dedicated data pre-processing protocol. To this end, we carried out indoor and outdoor experiments to monitor the evolution of soil crust and micro-scale soil roughness in response to cumulative rainfall kinetic energy. We combine data from a vis-NIR-SWIR hyperspectral sensor for spectral feature characterization at high resolution with image analysis in the spatial domain using a vis-NIR multispectral camera and high-resolution photogrammetry. The dynamics of soil crusting and soil roughness development were studied at two spatial scales: (i) at the 2 mm scale, which is the size of the small soil clods affecting micro-scale roughness, and (ii) at the 15 mm scale, which is the resolution obtainable by low-altitude UAS flights.

## 3.2 Materials and Methods

### 3.2.1 Experiment Design and Data Series

Soil samples were subjected to two separate phases of simulated or natural rainfalls: the aim was to force the evolution of soil crust and changes in surface micro-scale random roughness while controlling rainfall input. The runoff coefficient (RC) was calculated for every rainfall event as the ratio between the amount of runoff and the amount of precipitation. Soil crust development was first quantified from the changes in runoff caused by the progressive surface sealing. The amount of rainfall kinetic energy (KE)

previously applied to a soil sample to generate each specific crust condition was then used as a proxy for crust development. Surface conditions were sensed under dry soil conditions at the start of the experiment and after each rainfall application phase, under natural sunlight. Sensing was executed by means of close-up photogrammetry, multispectral imaging, and hyperspectral point measurements. This data was acquired to (i) estimate surface random roughness (RG) from a high-resolution DTM and (ii) to provide a spectral descriptor for crust development. In this way, both soil crusting and roughness were related as a response to cumulative rainfall kinetic energy. Four data series, consisting of three phases of surface monitoring, were generated to obtain a range of KE/RC/RG values. Three of the data series, each with three replicates, were obtained under laboratory conditions using simulated rainfall, while one data series, with six replicates, was obtained outdoor under natural rainfall. The data series structure is summarized in Figure 3.1.

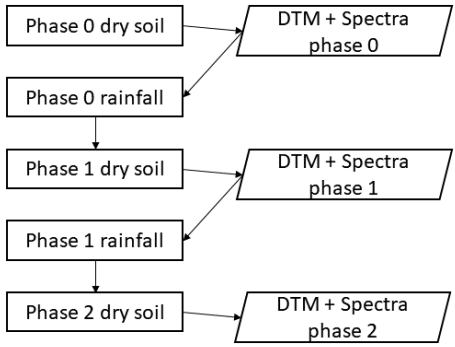


| | Series | | | |
|---|---|---|---|---|
| | **1** | **2** | **3** | **4** |
| **N° of boxes** | 3 | 3 | 3 | 6 |
| **Rainfall type** | Simulated | Simulated | Simulated | Natural |
| **Rainfall intensity (mm/h)** | 50 | 48 | 190 | variable |
| **Slope (deg)** | 1.8 | 5.6 | 5.6 | 6.3 |

Figure 3.1. Data series structure (top) and variables (bottom).

### 3.2.2 Samples Setup

Soil samples were collected from two adjacent cultivated fields situated in the Belgian loam belt. They are classified as Luvisols in the WRB classification

and silt-loam by texture according to the USDA classification. SOC content ranged between 9.3 and 10.9 g/Kg (analysed with the dry combustion method, as described in Chapter 2.2.1). Each container, from now referred to as "soilbox" (Figure 3.2), consists of a wooden box of 30 cm × 30 cm wide, 15 cm tall, open on the top and filled with 10 cm of manually compacted soil. Soil bulk density resulted ~1.3 g/cm$^3$ for soilbox series 1 and 2, ~1.4 g/cm$^3$ for series 3 and 4. The downslope side of the soilbox accommodates two sections that allow for water outflow: (i) on the top, a rectangular broad-crested weir, 30 cm wide and 2 cm tall, levelled with the soil for surface runoff: (ii) on the bottom, a rectangular hole 30 cm wide and 2.5 cm tall, for water exfiltration. A 2.5 cm thick metallic grate covered with geo-tissue was placed on the floor of the soilbox, acting like a selective membrane toward the exfiltration hole, to prevent soil loss while allowing water outflow.



Figure 3.2. Illustration of a soilbox used during the experiments.

### 3.2.3 Rainfall Data

An indoor rainfall simulator, consisting of an axial-flow full cone nozzle (Series 490/491 Lechler spray nozzles and engineered systems, Lechler GmbH, Metzingen, Germany) was positioned at a height of 3 m. The nozzle was connected to the water grid through a discharge gauge in order to set and monitor the amount of litres/second of water applied. A panel of 30 cm × 30 cm with 16 small buckets, was used to calibrate the rainfall simulator by converting the measured discharge to mm/h at floor level (after a drop fall of 3 m). Natural rainfall was measured with a tipping bucket rain gauge with a time resolution of 5 min and depth resolution of 0.25 mm. Rainfall intensity was kept constant during the simulated events and was variable under natural rainfall. No pre-wetting was applied to the soil samples.

To estimate the combined effect of rainfall duration and intensity on the soil surface (i.e., the destruction of clods and particle displacement), cumulative kinetic energy was chosen as an indicator. To estimate the kinetic energy $KE_p$ ($J \cdot m^{-2}$) applied during each measurement phase, time-specific rainfall kinetic energy $KE_t$ ($J \cdot m^{-2} \cdot h^{-1}$) was first estimated using the universal power law proposed by (Shin, Park and Choi, 2016), for each 5 min measuring time-step. $KE_p$ was then estimated as the sum of $KE_t$ for each measurement time step during a phase. This method is a simplification based on the assumption that the drop-size distribution is uniform in constant rainfall intensity. The cumulative kinetic energy KE was then estimated for each dry soil phase as the sum of each antecedent $KE_p$ since the start of the experiment.

### 3.2.4 Sensors

A Nikon D3100 camera (Nikon Inc., Tokyo, Japan) was used for photogrammetric soil surface reconstruction. The camera model is based on a DX format RGB CMOS sensor with a max resolution of 4608 × 3072 (14.2 effective megapixels). The camera was mounted with an 18-55 mm objective which was fixed at a focal length of 30 mm. The multispectral sensors employed was a Micasense Rededge-M multispectral camera (MicaSense Inc., Seattle, WA, USA). This widely used system consists of an array of 5 synchronized cameras, each having a distinct narrowband filter providing spectral bands centred at 475, 560, 668, 717 and 840 nm wavelengths, with a bandwidth (Full Width at Half Maximum) of 20, 20, 10, 40 and 10 nm respectively. The image resolution is 1280 × 960 pixels with 3.75 µm pixel pitch, and the camera has a focal length of 5.4 mm, resulting in a 47.2° cross-track FOV and a 36.2° along-track FOV. The hyperspectral sensor was an ASD Fieldspec 3 FR spectro-radiometer (described in Chapter 2.2.2).

### 3.2.5 Roughness Characterization Using Photogrammetry

For the photogrammetric surface reconstruction, 16 images were taken with the Nikon camera from different positions regularly distributed in a dome above the soil box, between 0.5 and 1 m of distance (see Figure 3.3-a). A DTM with 0.2 mm resolution was then generated for each soilbox/phase with the software Pix4Dmapper (Pix4Dmapper SA, 2022) (Figure 3.3-b,c), then resampled to 2 mm for calculation purposes. Four ground control points marked on the wooden frame of each soilbox were used to increase the accuracy of the DTMs and to allow the subsequent alignment of the multispectral images with the custom coordinate system of the surface

elevation models. Geolocation accuracy of the control points was estimated at 1, 1, and 0.5 mm for the X, Y and Z components, respectively. The wooden frames were then cropped out of the DTMs. For each DTM, the residual topography (the DTM detrended from the effect of the general soilbox inclination) was extracted subtracting the plane of the average soilbox slope from all DTM elevations. Maps of random roughness (RG) were then generated by calculating the standard deviation of the elevations on the residual topography in a moving square window of 22 mm × 22 mm (example of roughness map series in Figure 3.3-d, and corresponding RGB images in Figure 3.3-e). The size of the moving window was chosen to encompass the largest soil clods and, thus, the largest sources of roughness. The average value of random roughness for the whole box window was calculated in the same way.

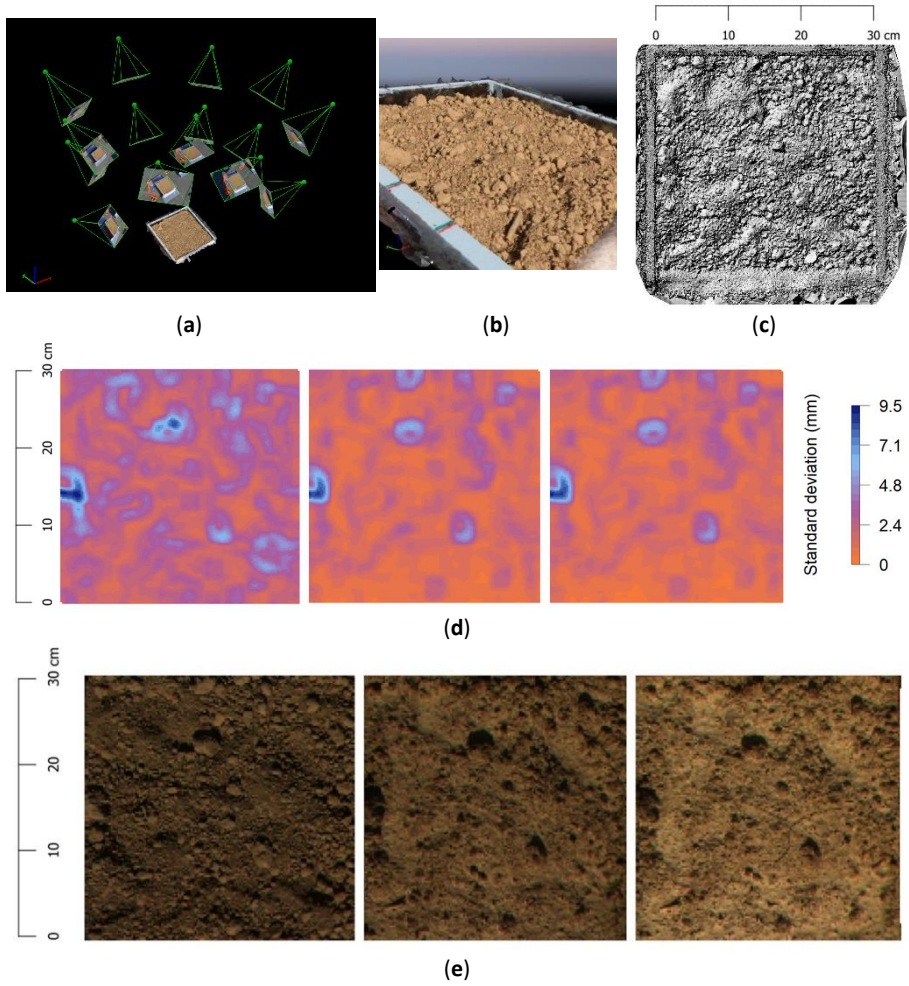


Figure 3.3. Roughness characterization using photogrammetry: (a) an illustration of the 3D mesh and the estimated positions of the camera; (b) detailed view of the 3D mesh from close distance; (c) DTM with hillshade representation. In the middle (d) an example of random roughness map, for the same soilbox, in three subsequent phases (left to right: before, after first and after second rainfall application) and, on the bottom (e), their corresponding RGB images.

### 3.2.6 Spectral Data Acquisition and Pre-Processing

Soil spectral measurements were carried out in outdoor conditions in an open area to minimize reflection from vertical objects in the surroundings, during stable, clear-sky and natural sunlight conditions for the whole duration of the measurements. Measurements were taken within two hours of solar noon. Before every sensor measurement took place, the soil-boxes

were oven-dried at 60 °C for 72 h and then air-dried in open air for at least other 48 h. For the hyperspectral measures, the sensor head was set at ca. 6 cm height above the soil surface, at the nadir position, providing a measurement footprint with a diameter of c. 2.6 cm. This footprint was chosen to allow for an easy individuation on the multispectral images for spectral comparison. Each single spectral acquisition with the ASD instruments was performed with an integration time of 5.4 s. 25 measurements were taken during each phase, in a regular 5 cm × 5 cm grid. Radiometric calibration for the ASD was automatically managed by its hardware + software routine. For the conversion of radiance to reflectance a Spectralon white reference surface measurement was repeated every ten samples. Bandwidths below 400 nm and above 2400 nm were removed because they typically contain excessive noise, as well as the bandwidths influenced by water vapour absorption in the intervals 1350–1450 and 1800–1950 nm. Spectra were also smoothed with a Savitzky-Golay smoothing filter (Savitzky and Golay, 1964) using a second order polynomial fit. Spectral outliers were removed, at each box/phase level, setting a threshold of three times the standard deviation of the Mahalanobis distance of the spectra projected in the first two latent variables of the principal component space. The average of the 25 spectra (minus outliers) was then used as representative for each box/phase.

For multispectral imaging, a single picture was taken for each soilbox phase, from 1 m distance at the nadir position. Radiometric calibration, image correction and conversion to reflectance for the Rededge-M images were performed in post processing following the procedure described on the manufacturer's website (*RedEdge Camera Radiometric Calibration Model*, no date) using the software R (R Core Team, 2021). Conversion to reflectance was possible thanks to the employment of a calibrated reflectance panel (provided by the Rededge-M manufacturer), which was sampled before each sample image acquisition. Reflectance images were then scaled to true dimension (resulting in pixel size of c. 0.5 mm) and orthorectified by anchoring the 4 ground control points visible in the pictures to those identified in the photogrammetric procedure, using R software and gdal (GDAL/OGR contributors, 2020) scripts. Scaling and orthorectification were executed separately for each image in the 5 spectral bands to account for the different offset of the Rededge-M sensors. Finally, images were resampled at two resolutions: 2 mm and 15 mm.

Since multispectral images were acquired at very high resolution, shadows cast on the soil surface were affecting a substantial portion of the soil surface. Shadows commonly cause partial or total loss of radiometric signature, hence shadow reduction or removal becomes important during image analysis (A. Movia, Beinat and Crosilla, 2016). A threshold segmentation method applied on the intensity (also referred as brightness) component I of the HSI colour system (Surveying, 2013) was calibrated and found to be sufficient for shadow detection and elimination on our case study. The method is discussed in detail in the Appendix B. Shadows from micro-reliefs and soil cracks were removed from all multispectral images with this method to create the base dataset (example in Figure 3.4, central column). Furthermore, a new set of multispectral maps ("DR") was generated by removing pixels where the random roughness was above the threshold of 2 mm, which was visually assessed as appropriate to discard soil clods, and consistent with the minimum pixel size (example in Figure 3.4, right columns). The underlying idea is that this allows isolating soil crust colour information from the light scattering effect of roughness.

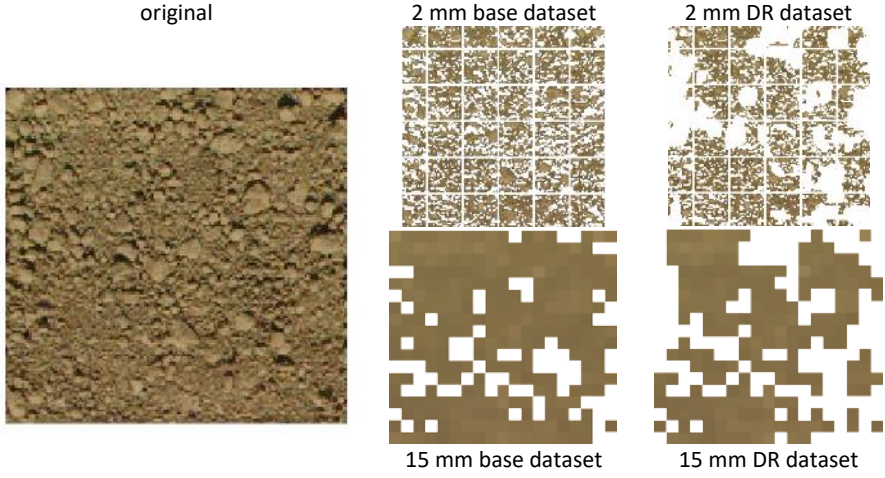


Figure 3.4. Example of RGB composite from multispectral image that shows the steps of pixel selection for the selective extraction of spectral data: original image; base dataset (with shadows removed) at 2 mm and 15 mm resampling; DR dataset (with roughness threshold < 2 mm) at 2 mm and 15 mm resampling. The images at 2 mm resolution also display with white lines the 6 × 6 grid used for partitioning reflectance histogram extraction.

### 3.2.7 Multispectral Data Extraction

Previous studies (Croft, Anderson and Kuhn, 2009, 2012) on the directional reflectance properties of soil surface showed that rough soils exhibit higher degrees of spectral anisotropy, resulting in wavelength-dependent spectral variability. We thus hypothesise that the residual (after de-shadowing) light scattering effect related to soil surface irregularities (i.e., roughness) in the multispectral spatial domain could be assigned to a spectral variability index in its spatial domain. We hereby propose to calculate this variability with a wavelength-specific inter-quantile range (*iqr,* visualized in Figure 3.5-a) of the reflectance values on a given surface. To do so, local spectral histograms for all the multispectral bands were extracted at two spatial scales, on each soilbox,: (i) in a 5 cm × 5 cm grid (example in Figure 3.4, top-right) on the images at 2 mm resolution (total of 36 squares per soilbox, number of total sampling locations n = 36 × 42 = 1512); (ii) on the whole soilbox for the images at 15 mm resolution (number of sampling locations n = 42). From each histogram two indexes for each of the five available broad-bands were used to summarize the multispectral data: the mean reflectance value and *iqr*. This information was extracted both from the base dataset and from the DR one. Mean multispectral values were also compared for consistency with hyperspectral values at the same sampling locations (Figure 3.5-b).

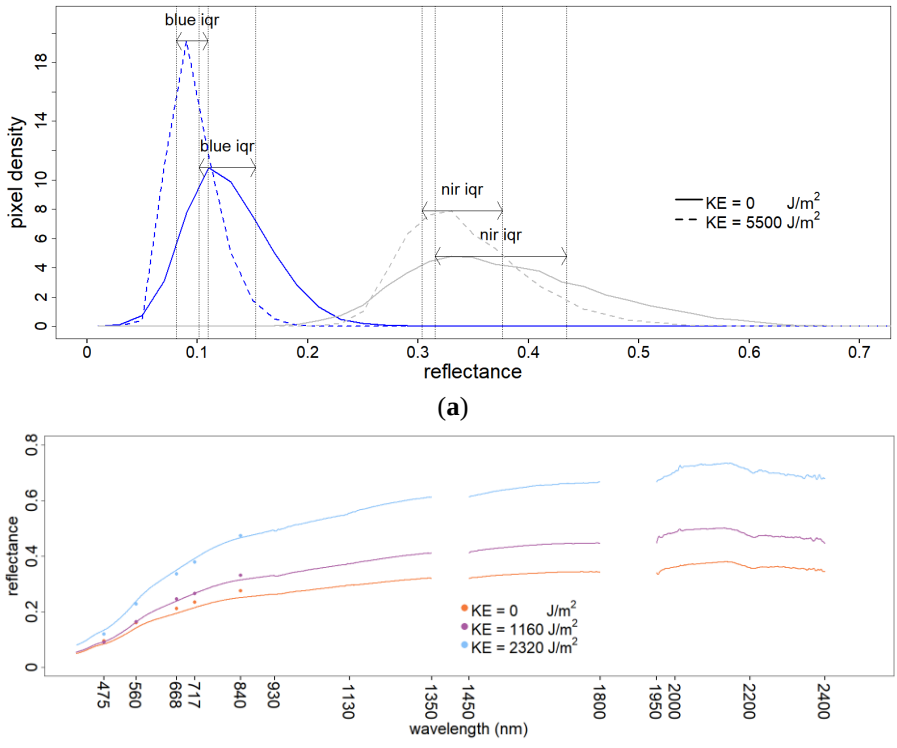


Figure 3.5. (a) Example of the evolution of the multispectral pixel density histograms, for two spectral bands drawn as an example (blue and NIR, respectively coloured in blue and grey), from a single soilbox across two different amounts of cumulated rainfall kinetic energy (0 and 5500 J/m$^2$). The *iqr* is visualized as the span distance between the 1st and 3rd quantile of each histogram; (b) example of the evolution of mean multispectral reflectance values (points) and corresponding hyperspectral reflectance samples (lines) at the same soilbox location, for three levels of KE (0, 1160 and 2320 J/m$^2$).

### 3.2.8 Spectral Modelling

The aim of the spectral data acquisition was to build a spectral model for soil crust development and to disentangle the effects of random roughness from soil physical-chemical changes on reflectance factors. In this framework, crust development (through its proxy kinetic energy) and roughness were used as the main target variables for PLSR spectral modelling. The higher spectral resolution of hyperspectral-based models was used to assess the relative relevance of vis, NIR and SWIR spectral regions and of specific spectral features in KE models through the variable importance in projection (VIP) analysis and to support the interpretation of vis-based multispectral

data. Multispectral-based models were developed and validated to find the optimal data pre-treatment techniques for KE and RG prediction and mapping purposes.

From the hyperspectral data, PLSR models were developed on both raw reflectance (refl) and reflectance transformed through SNV, using the R package "pls". SNV normalizes each vector of spectral data by subtracting its mean and dividing by its standard deviation. It is intended to normalize spectral data to correct for light scattering, normally influenced by irregular surface geometry and particle size. In this study, its intended purpose was to understand to what degree it could be used to separate colour features from roughness features.

From the multispectral data, PLSR models were developed on datasets that were filtered and/or transformed to remove the effect of roughness on spectral features in a gradual way: (i) base reflectance maps; (ii) reflectance maps with DR filter; (iii) SNV transform; (iv) SNV transform and DR filter. Models were developed at a 2 mm and 15 mm resolution. A "leave-one-out" cross validation was used to select the optimal number of latent variables for each sub-dataset. The best PLSR model was selected based on the number of latent variables (PLSR components) above which a decrease in RMSE was not significant. To evaluate the stability and consistency of the models a validation was then performed splitting each dataset into calibration and validation (80% and 20%, respectively), with random selection and model re-calibration for 200 repetitions. The performance of the models was evaluated on the validation datasets using the mean of 200 simulations of the following metrics: (i) MRE %, (ii) RMSE, (iii) $R^2$ and (iv) RPIQ. The VIP was used to assess variable importance in the PLS regressions. A threshold VIP score of 1 was used to highlight relevant variables (ref). The modelled datasets are summarized in flow chart (Figure 3.6).

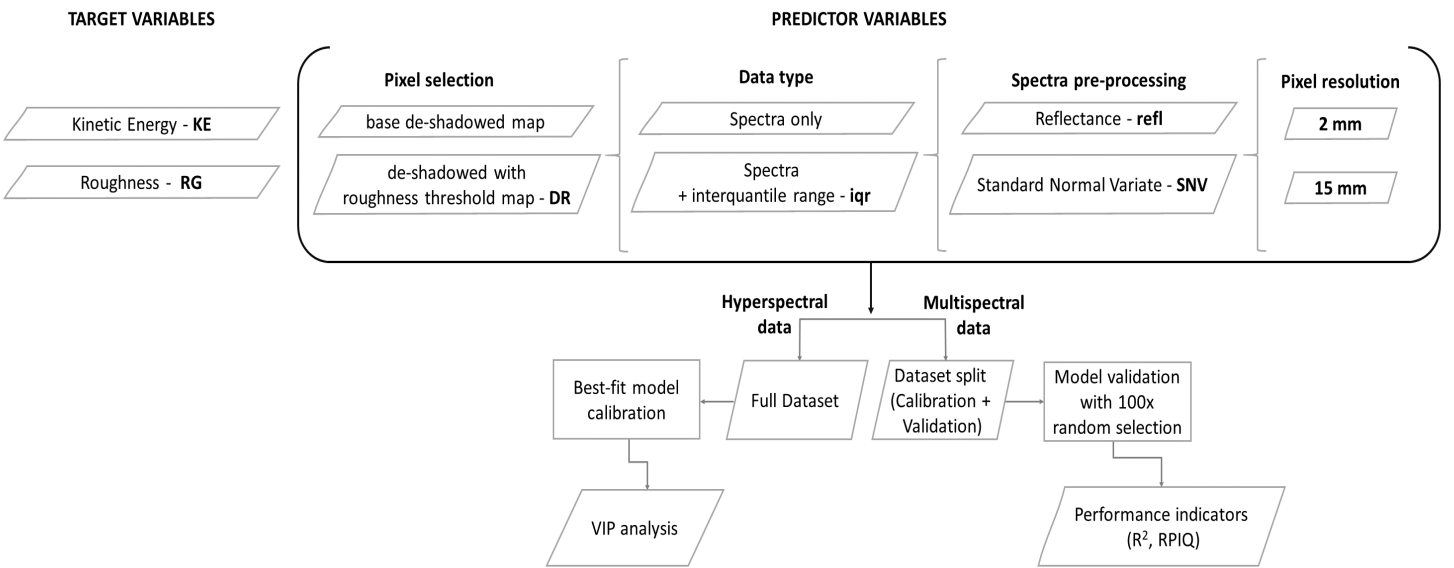


Figure 3.6. Flowchart of data selection and sub-setting for the PLSR modelling of multispectral data.

## 3.3 Results and Discussion

### 3.3.1 KE, Crusting and Roughness Data

Figure 3.7 shows the relationship between the RC and the amount of KE previously received by the soil samples surface during the experiments. RC was positively correlated with KE, with an overall significant correlation of 0.82. These results are in line with the evidence, provided by previous studies (Valentin and Bresson, 1998; Ben-Dor *et al.*, 2003), that the amount of KE received by a soil surface can be linked to the sealing effects and decrease in infiltration rate due to the development of a soil crust. This provides, together with the observed changes in soil spectra discussed below, a solid basis to link soil crust development to cumulative rainfall kinetic energy.
Figure 3.8 and Figure 3.9 synthesizes the data obtained for KE and roughness for the two resolutions (i.e., 2 and 15 mm, respectively), and their relationship during the experiments. Both scatterplots show that the soilboxes were prepared with a range of starting roughness conditions (i.e., between 0–5 mm and 0 J/m$^2$ of KE) that were subsequently levelled by rainfall to values between 1 and 2 mm. This resulted in a roughness distribution skewed toward these values, but with significant correlations ($0.37 < r < 0.87$) for all four data series. One data series (3rd) provided data with KE amount higher than 3000 J/m$^2$, resulting in skewed distribution also for KE values.

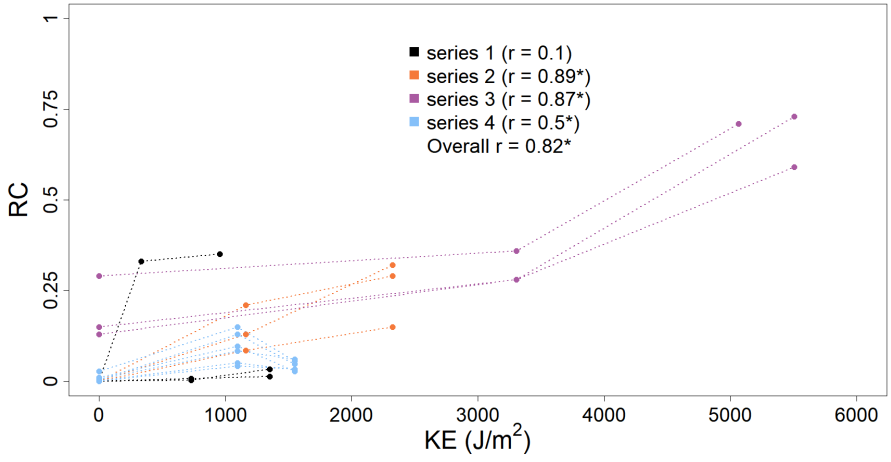


Figure 3.7. Scatterplot of KE in J/m$^2$ and RC. The pertinence to the four data series is highlighted with colours. Correlation values with $p < 0.05$ are marked with *.

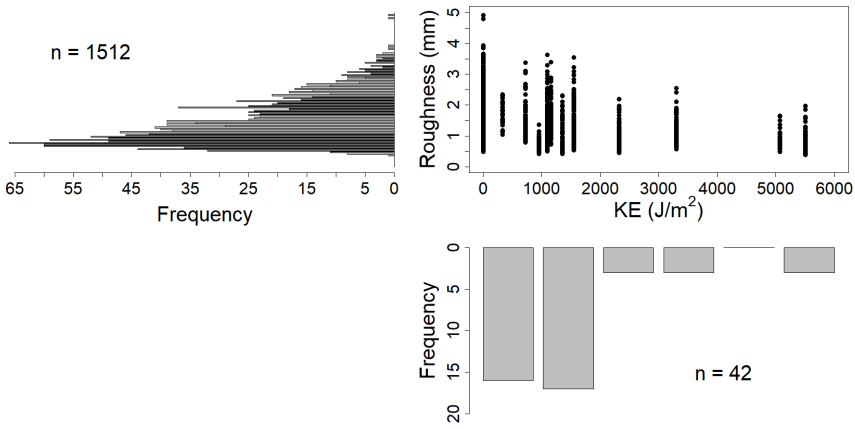


Figure 3.8. Scatterplot of KE in J/m² and measured roughness in mm of standard deviation, detailed for the 2 mm resolution. Data histograms are plotted side by side to the respective axes.

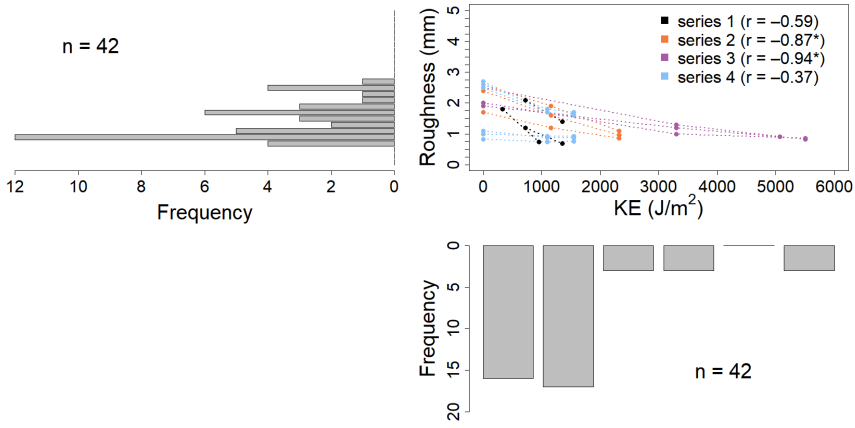


Figure 3.9. Scatterplot of KE in J/m² and measured roughness in mm of standard deviation, detailed for the 15 mm resolution. Data histograms are plotted side by side to the respective axes. The pertinence to the four data series is highlighted with colours. Correlation values with $p < 0.05$ are marked with *.

### 3.3.2 Hyperspectral Variable Importance

PLSR models based on the hyperspectral data were developed aiming at the best fit to highlight the optimal variable importance for KE with different datasets. Full range reflectance data (Figure 3.10) provided the best model fit but the full range SNV (Figure 3.11) attributed more importance to the vis-

NIR portion of the spectrum with comparable performance. Common peaks of information were found at 570, 930 and 1130 nm for the vis-NIR region and 1950, 2000, 2140 and 2200 nm for the SWIR region. The 2140 and 2200 nm peaks were already individuated and described by other studies (Ben-Dor *et al.*, 2003; Eshel, Levy and Singer, 2004) working on the spectral properties of soil crust and assigned to the enrichment of soil surface in clay particles during the crusting process. The use of only the vis-NIR portion of reflectance spectra (Figure 3.12-a) and SNV (Figure 3.12-b) with hyperspectral data showed that modelling of KE was possible, thus motivating the prospect of using the vis-NIR range only, in both base reflectance and SNV transformation. No sensible reflectance/SNV difference was obtained in either variable selection (except a peak on the blue reflectance wavelengths) nor performance, and a peak on information was observed in both datasets at 762 nm. An increase in baseline (albedo) was generally observed with increasing levels of KE (as reported in the example in Figure 3.5), in line with the observations made by the studies just mentioned (Ben-Dor *et al.*, 2003; Eshel, Levy and Singer, 2004). Nevertheless, changes in slope in the vis-NIR portion of our soil spectral may have played an important role in KE model performance. These same studies also pointed out that reflectance changes in soil crust are dependent on soil texture and mineralogy; the soil samples used in this study were homogeneous in texture and collected from the same area. Although this allows us to compare the different experiments, it represents a limiting factor for the generalization of our results.

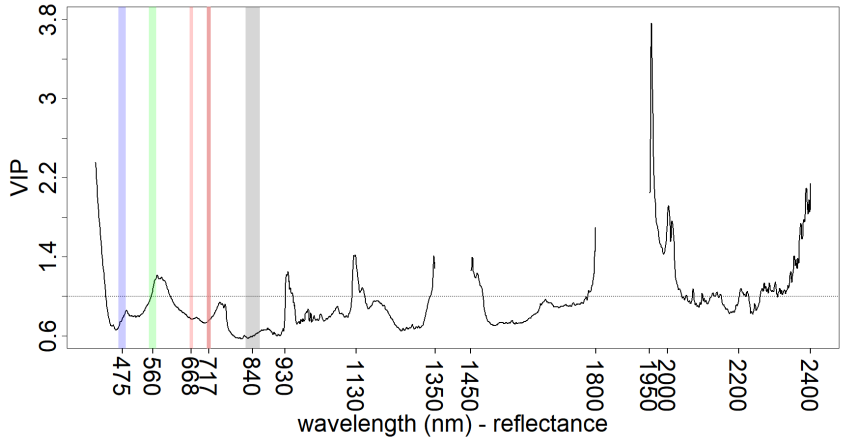


Figure 3.10. VIP scores of KE PLSR models from hyperspectral data using full vis-NIR-SWIR reflectance spectral range. Goodness of fit is reported using $R^2$ and RPIQ. The

multispectral broad-bands of the Rededge-M camera model are shown for comparison.

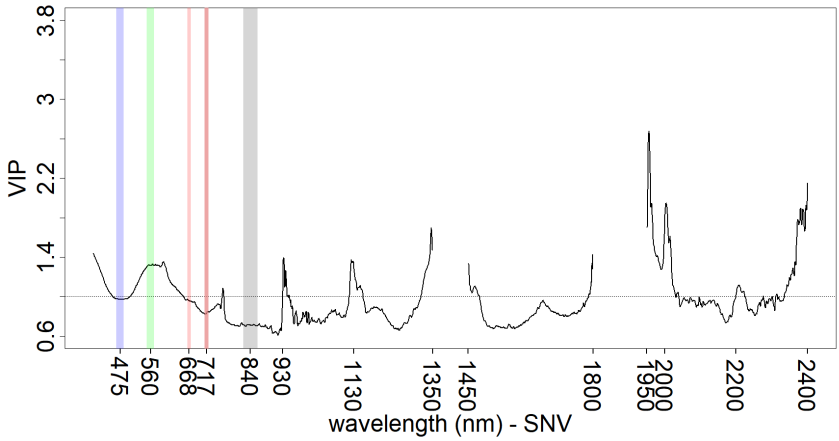


$R^2$ = 0.97, RPIQ = 5.82

Figure 3.11. VIP scores of KE PLSR models from hyperspectral data using the SNV of the full vis-NIR-SWIR spectral range. Goodness of fit is reported with $R^2$ and RPIQ. The multispectral broad-bands of the Rededge-M camera model are shown for comparison.

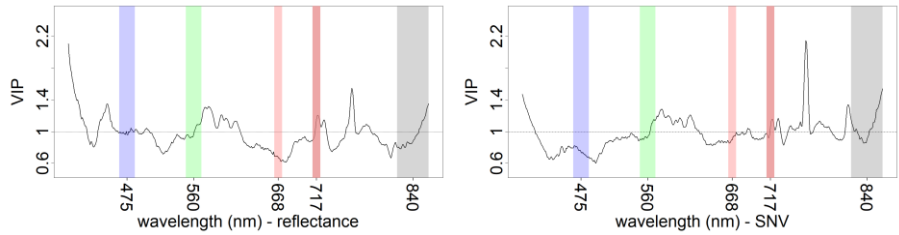


(**a**) $R^2$ = 0.88, RPIQ = 3.14 (**b**) $R^2$ = 0.87, RPIQ = 3.01

Figure 3.12. VIP scores of KE PLSR models from hyperspectral data using: (a) reflectance vis-NIR range; (b) SNV vis-NIR range. Goodness of fit is reported with $R^2$ and RPIQ. The multispectral broad-bands of the Rededge-M camera model are shown for comparison.

### 3.3.3 Correlation with Multispectral Data

A correlation analysis was carried out between the target parameters (i.e., KE and roughness) and the spectral indices (i.e., spectra and *iqr*) with different data pre-treatments (base, roughness thresholding DR, SNV) at the 2 mm spatial scale (Figure 3.13-a,b, for KE and roughness, respectively). Considering only the results where $p < 0.05$, four base reflectance values (excluding the blue band) showed a low positive correlation with KE (0.03 < r

< 0.12) and a low negative correlation with roughness (−0.13 < r < −0.17). On the other hand, *iqr* values showed significantly higher correlations, both negatively with KE (−0.24 < r < −0.33) and positively with roughness (0.21 < r < 0.36). In general, base reflectance and *iqr* correlation resulted in opposing trends between KE and roughness. The SNV transformation of base reflectance increased the correlation of some spectral bands with KE (blue = 0.23, green = −0.28, rededge = −0.27). SNV mildly affected the significative correlation of two spectral bands with roughness (red = −0.12, rededge = 0.19, with opposite sign respect to KE) and showed no correlation with the other 3 bands. The DR pre-treatment, with both KE and roughness, did not influence the correlation values of base reflectance or SNV but had a sensible effect in lowering the correlation of *iqr* (−22/24% with KE, −44/50% with roughness). This analysis shows that KE and roughness are spectrally entangled. This is also evident from the high correlation of their change after rainfall application. Nevertheless, the analysis shows that the *iqr* index seems to be a better index to describe roughness, due to its overall significant positive correlation and to its negative response to DR pre-treatment. SNV, on the other hand, was more strongly related to KE.

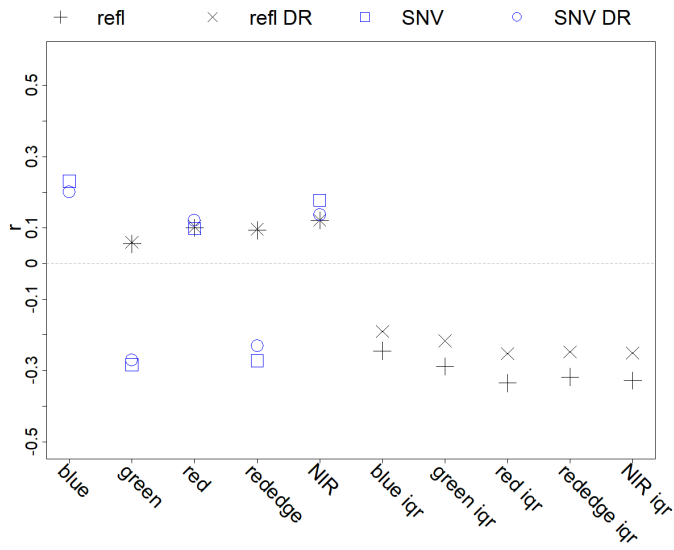


(**a**) KE

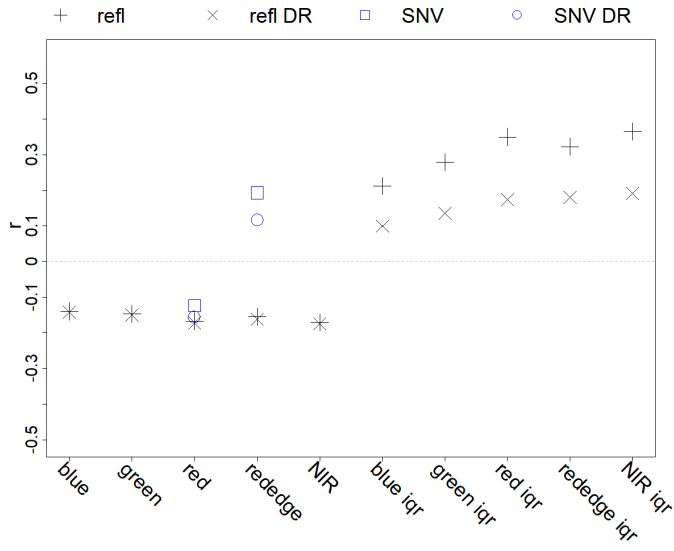


(**b**) RG

Figure 3.13. Correlation of the multispectral indexes with KE (a) and with roughness (b) from the 2 mm resolution dataset: “refl” represents the base dataset, “DR” the roughness threshold dataset, “SNV” the Standard Normal Variate transformation of reflectance data. Points where $p < 0.05$ were excluded from the plot.

### 3.3.4 Modelling Multispectral Data

Results from the validation phase of the PLSR models are shown in Figure 3.14 ($R^2$) and Figure 3.15 (RPIQ). At the 2 mm resolution (Figure 3.14-a and Figure 3.15-a), models for KE per-formed better when using the combination of pure reflectance + *iqr* data, while the DR pre-treatment did not affect performance ($R^2$ refl = 0.47, refl DR = 0.44). SNV transformation substantially decreased performance both for the base and DR sub-datasets ($R^2$ SNV = 0.25, SNV DR = 0.2), on par with the reflectance models based on spectra only ($R^2$ refl = 0.25, refl DR = 0.23). Regarding roughness, model performance decreased with the different techniques used to account for roughness effects: in order, from the base reflectance dataset ($R^2$ = 0.41) to its DR sub-dataset, to SNV, and finally SNV DR ($R^2$ = 0.09). Performance using spectra only (no *iqr*) were low in all cases. In general, at the fine scale, the datasets with DR pre-treatment were the ones where the difference between KE and roughness model performances was the highest, both with reflectance and SNV. The roughness removal pre-processing methods were lowering the performance of the rough-ness models, as expected, but SNV negatively affected KE models too. Since SNV did not affect model performance with hyperspectral data, it is possible that the loss of albedo in-formation from this data transformation technique may be necessary for multispectral modelling of KE. For our experiments, reflectance + *iqr* based models with DR pre-treatment seemed to be the data processing protocol with the best combination of high predictive performance and high discrimination between KE and roughness.

At the 15 mm resolution (Figure 3.14-b and Figure 3.15-b), KE model performance was on aver-age lower than with the 2 mm resolution with reflectance-based data ($R^2$ refl = 0.34, refl DR = 0.35) and slightly better with SNV ($R^2$ SNV = 0.29, SNV DR = 0.31). Roughness modelling performance showed the same decreasing power with the data pre-treatment techniques, as seen with the 2 mm resolution, from $R^2$ = 0.49 to $R^2$ = 0.28. No sensible difference was brought by the DR pre-treatment. Regarding the models based on spectra only, KE models resulted in equivalent performance as with the *iqr* dataset, while roughness models showed generally poor predictions. In general, at the coarser scale, all models for KE per-formed equally but showed a very low RPIQ (~1), probably due to the limited number of samples and variability in the calibration dataset. Roughness models, on the other hand, provided acceptable predictions. As a result, the best data processing

protocol proposed for the 2 mm resolution dataset could not be confirmed when using the 15 mm resolution dataset.

Overall, SNV + *iqr* did not offer better model performances than using only base reflectance indexes, especially at the finer scale where richer calibration data where available. Given the good modelling performance with the SNV of hyperspectral data, it is possible that the available multispectral resolution was not suitable for this kind of data transformation for KE predictions. The albedo information contained in pure reflectance data may be critical for KE prediction with multispectral data. Other studies that at-tempted modelling crust development (Ben-Dor *et al.*, 2003; Eshel, Levy and Singer, 2004) obtained good results ($0.86 < R^2 < 0.94$) using specific SWIR hyperspectral bands to predict crusted soil infiltration rates, but did not perform a validation of their models. To our knowledge, no other studies attempted modelling soil crusting with vis-NIR multispectral data.

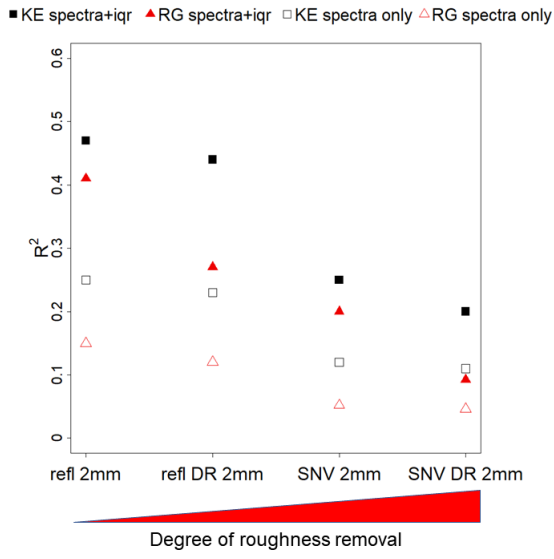


(**a**)

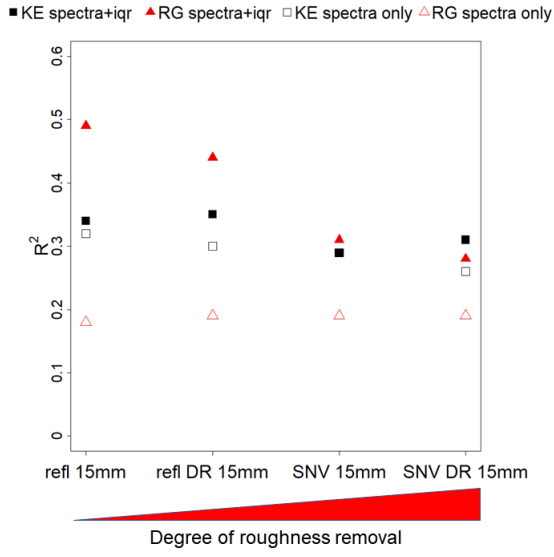


(**b**)

Figure 3.14. Validation of the PLSR models (using $R^2$) for the different data transformations, ordered by their degree of roughness removal, from left (none) to right (max). Black symbols depict KE models $R^2$, while red symbols represent RG models $R^2$. Solid symbols represent models based on spectral data + *iqr*, void symbols represent models based on spectra only. Panel (a) shows result for the 2 mm scale, panel (b) results for the 15 mm scale.

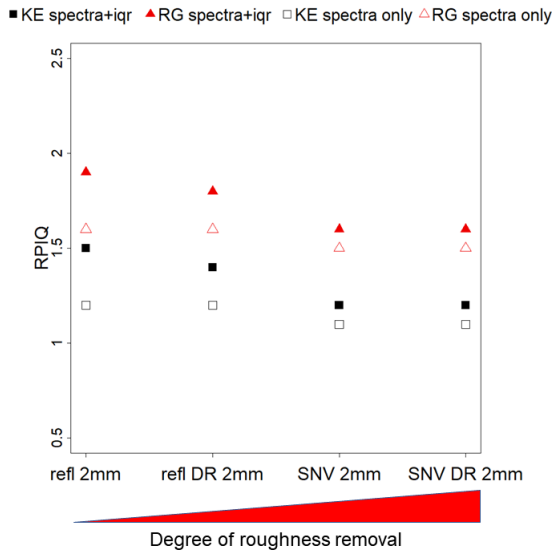


(**a**)

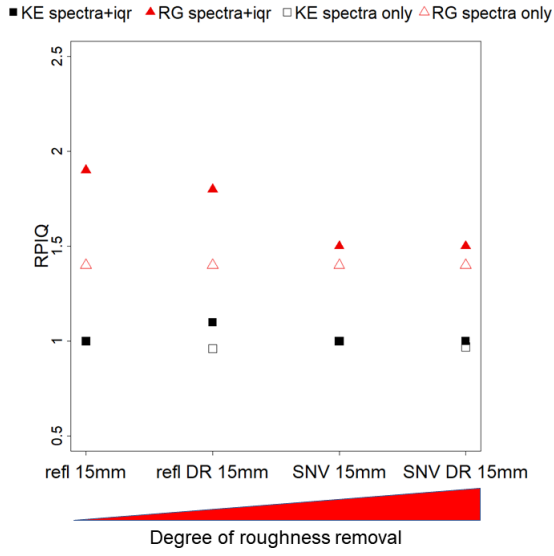


(**b**)

Figure 3.15. Validation of the PLSR models (using RPIQ) for the different data transformations, ordered by their degree of roughness removal, from left (none) to right (max). Black symbols depict KE models $R^2$, while red symbols represent RG models $R^2$. Solid symbols represent models based on spectral data + *iqr*, void symbols represent models based on spectra only. Panel (a) shows result for the 2 mm scale, panel (b) results for the 15 mm scale.

### 3.3.5 Multispectral Variable Importance

At the 2 mm spatial scale VIP scores showed some interesting differences in variable selection between KE and RG models (Table 3.1). When using reflectance data, KE models used a combination of base spectral bands (blue, green, NIR) and *iqr* indexes while roughness models were mainly dependent on *iqr* indexes (VIP > 1 for red, rededge and NIR). This supports the hypothesis that emerged from the correlation analysis that the spectral *iqr* contains useful information to model roughness. The SNV shifted the weight of KE model variable selection from *iqr* towards pure spectral bands (especially on the rededge channel, as expected from correlation analysis) but had the same effect on roughness models. Given that model performances were substantially lowered for both KE and roughness when adopting SNV, it is possible that this technique effectively accounted for the effects of roughness, but the available multispectral sensor resolution was not suitable for the modelling of KE.

At the 15 mm resolution, variables behaviour for both KE and roughness models was similar to that at the finer resolution. In general, blue *iqr* and green *iqr* indexes were discarded by all models (their correlation was also weaker relative to the other three bands *iqr*). A possible reason for this, as postulated by (Croft, Anderson and Kuhn, 2009), is that, due to Rayleigh scattering effects in the atmosphere, greater directional interference from atmospheric scattering in shorter wavelengths can cause a less coherent directional signal from the soil in these channels.

Table 3.1. VIP scores from the multispectral data PLSR models of kinetic energy (KE) and roughness (RG) at the two different resolutions. VIP scores higher than 1 are marked with grey colour cells.

| | | Blue | Green | Red | Reded | NIR | Blue *iqr* | Green *iqr* | Red *iqr* | Reded *iqr* | NIR *iqr* |
|---|---|---|---|---|---|---|---|---|---|---|---|
| KE 2 mm | refl | 1.09 | 1.33 | 0.989 | 0.974 | 1.14 | 0.48 | 0.726 | 0.938 | 1.04 | 1.05 |
| | refl DR | 1.14 | 1.35 | 0.898 | 0.812 | 1.01 | 0.514 | 0.769 | 0.998 | 1.13 | 1.12 |
| | SNV | 0.815 | 1.24 | 0.996 | 1.29 | 0.998 | 0.86 | 0.864 | 0.864 | 0.94 | 1.01 |
| | SNV DR | 0.825 | 1.34 | 1.13 | 1.26 | 1.01 | 0.816 | 0.84 | 0.796 | 0.867 | 0.948 |
| RG 2 mm | refl | 0.734 | 0.906 | 0.731 | 0.898 | 0.974 | 0.591 | 0.94 | 1.18 | 1.34 | 1.38 |
| | refl DR | 0.857 | 0.97 | 0.838 | 0.723 | 0.927 | 0.603 | 0.915 | 1.18 | 1.38 | 1.32 |
| | SNV | 0.497 | 1.01 | 1.05 | 1.24 | 0.71 | 0.843 | 0.883 | 1.08 | 1.15 | 1.27 |
| | SNV DR | 0.552 | 0.964 | 1.55 | 1.1 | 0.69 | 0.821 | 0.806 | 0.938 | 1.05 | 1.14 |
| KE 15 mm | refl | 1.18 | 1.15 | 1.09 | 0.992 | 1.03 | 0.778 | 0.634 | 0.822 | 0.945 | 1.14 |
| | refl DR | 1.25 | 1.2 | 0.985 | 0.949 | 1.13 | 0.655 | 0.592 | 0.822 | 0.997 | 1.06 |
| | SNV | 0.821 | 1.66 | 1.61 | 0.947 | 0.865 | 0.818 | 0.412 | 0.495 | 0.695 | 0.772 |
| | SNV DR | 0.769 | 1.64 | 1.66 | 0.936 | 0.876 | 0.768 | 0.378 | 0.487 | 0.782 | 0.701 |
| RG 15 mm | refl | 0.98 | 0.982 | 0.906 | 0.698 | 1.13 | 0.591 | 0.864 | 1.09 | 1.15 | 1.35 |
| | refl DR | 1.02 | 1.08 | 0.995 | 0.694 | 1.28 | 0.59 | 0.754 | 1.03 | 1.03 | 1.25 |
| | SNV | 0.835 | 1.22 | 1.5 | 0.797 | 1.38 | 0.421 | 0.607 | 0.771 | 0.878 | 0.976 |
| | SNV DR | 0.909 | 1.32 | 1.49 | 0.811 | 1.38 | 0.41 | 0.604 | 0.709 | 0.814 | 0.923 |

## 3.4 Conclusions

We have developed PLSR models based on vis-NIR multispectral imaging data to predict the cumulative kinetic energy received by soil samples, as a proxy for soil crust development. The combination of hyperspectral data, multispectral imaging and high-resolution topography from photogrammetry offered insights to identify a suitable data pre-treatment protocol that allows to isolate the effects of rainfall kinetic energy (and hence crusting) from micro-scale roughness in soil reflectance factors. After eliminating shadows, we assigned the residual light scattering effect related to soil surface irregularities (i.e., roughness) in the multispectral spatial domain by calculating the inter-quantile range *iqr* of the reflectance values in a kernel. A high resolution DTM provided a map to exclude areas where prominent roughness was present (i.e., DR sub-setting). At the 2 mm image resolution, the *iqr* of all multispectral bands was significantly related to soil roughness. PLSR models suggested that a model based on reflectance + *iqr* data with DR pre-treatment provides the best combination of high predictive performance and high dis-crimination between kinetic energy and roughness. SNV provided lower performance for kinetic energy prediction with multispectral data, while it did not deteriorate model performance with hyperspectral data. This demonstrates that hyperspectral data contains

information to model the effect of rainfall kinetic energy on soil crusting from small, specific features and this with a high model performance. In contrast, multispectral datasets have to rely more on albedo information, which is removed by SNV. At the 15 mm image resolution, the same conclusions could not be made: models for roughness performed equally or better than those for kinetic energy and as a result, no clear discrimination between them could be made. This issue was most probably related to the limited sample size used and the non-optimal distribution of kinetic energy values for model calibration and our results are therefore not conclusive. A VIP analysis showed that the variable importance was significantly different between kinetic energy and roughness models based on reflectance + *iqr* sub-setting, supporting our conclusion on the preferential discrimination technique: while kinetic energy models were also relying on base reflectance information, roughness components were almost exclusively related to some specific *iqr* indexes.

As a general conclusion, our experiments suggest that it is possible to model the amount of rainfall kinetic energy received by a soil sample, as a proxy for crust development, from vis-NIR based multispectral imaging. However, there is a caveat: roughness effects on spectral features should be eliminated before modelling. Among the tested methods for roughness effect removal, shadow elimination was found to perform consistently at both 2 mm and 15 mm image resolution; DR sub-setting and *iqr* calculation can improve spectral discrimination of kinetic energy effects from roughness effects, but a fine image resolution is required (good at 2 mm, insufficient at 15 mm). Although these findings are limited to a single soil type, the methods and analysis proposed in this study provide a first workflow to interpret data from multispectral imaging for the mapping of soil crusting.

# Chapter 4

# Modelling soil physical crust development in field conditions


## Summary

Results of a laboratory experiment, described in Chapter 3, suggested that it is possible to model the amount of rainfall kinetic energy received by a soil sample, as a proxy for soil physical crust development, with vis-NIR multispectral proximal sensing. Chapter 4 aimed at verifying these findings with an experiment in real field conditions, in small plots on an agricultural loamy soil, and trying to quantify the contribution of the development of soil crust on sediment yield under natural rainfall conditions. Field experiment results showed that the five vis-NIR spectral broad-bands of a commercial grade multispectral camera were sufficient to predict ($R^2$ = 0.79) a series of KE levels by simply removing shadows and normalizing the spectra through a SNV transformation. These results represent a first step to start the UAS-based remote sensing assessment soil physical crust development at the wider scales of fields or small basins. On the other side, the collection of soil eroded and exported from the plots did not show a significant correlation between increased soil crust development and sediment export. Indeed, due to a non-optimal experiment design, it was also not possible to measure with accuracy the amount of runoff and associate its increase to crust development.


## 4.1 Introduction

Chapter 3 presented the development of a methodology to predict the cumulative rainfall kinetic energy received by soil samples, as a proxy for soil crust development, based on the analysis and modelling of vis-NIR multispectral imaging data. Results showed that the combination of hyperspectral data, multispectral imaging and high-resolution topography from photogrammetry offered insights to identify a suitable data pre-treatment protocol to isolate the effects of rainfall kinetic energy from micro-scale roughness in soil crust reflectance factors. One issue still open was the applicability of this method in real field conditions, when attempting to take advantage of proximal sensing technologies from UAS. Another open issue was whether a more detailed modelling and mapping of soil crust could

provide a better understanding of its complex influence on sediment generation. In this regard, this fourth chapter was devolved to pursue the following objectives:

I. To verify, building on the findings of thesis Chapter 3, if soil crusting stages can be described by means of low altitude UAS-based multispectral imaging in real field conditions.
II. To quantify the contribution of the development of soil crust on runoff and sediment yield under natural rainfall conditions on an agricultural loamy soil.

To reach these objectives, six small plots, located on the same cultivated field in the Belgian loam belt, were followed during a period of three months to monitor the evolution of soil surface conditions and their sediment generation response under natural rainfall. Crusting conditions were monitored with ground-based hyperspectral point data and UAS-based multispectral imaging data collected at an altitude of 20m. A linear mixed model approach was used to: i) quantify the effect of the KE term when used in addition to the rainfall term in the prediction of exported sediment (S); ii) verify whether the KE term is associated to an increase in erosion susceptibility.

## 4.2 Materials and Methods

### 4.2.1 Experimental plots

The experiment took place in spring 2018, between April and July. The six plots (Figure 4.1-a) were located on a single field in the Belgian loam belt (Louvain-La-Neuve), within a summer wheat cultivation. Its soil is classified as Luvisols by the WRB system, and as silt-loam according to the USDA classification. SOC content ranged between 9.3 and 10.9 g/Kg (analysed with the dry combustion method, as described in Chapter 2.2.1). Each plot consisted of a 2x1 m bare soil surface with the long side along the slope gradient. Surface was manually kept as bare soil for the whole duration of the experiment. The plots were ploughed and harrowed with a hoe for a depth of about 10 cm. As the soil served for the “soilbox” experiment, in series 1 and 2 (see Chapter 3.2.2), starting soil bulk density was assumed to be ~1.3 g/cm$^3$. The downstream side of each plot was ending in a triangular flume of aluminium, used to channel water and sediment coming from the plot into a plastic collector isolated from rainfall (Figure 4.1-b and detail in Figure 4.1-d). The entire upstream and lateral sides of each plot were

delimited by a strip of neoprene about 40 cm high, 20 cm of which underground, to prevent runoff from the rest of the field entering the plot (Figure 4.1-b, c). Plots were placed in pairs on three slopes (4.5, 6.5, 9.5 degrees). Within each slope-based pair, one plot was kept with completely bare soil, while the other was covered on about 5% of the surface with evenly sparse residues of the precedent cultivation (winter wheat straw). On each plot, four fixed targets were placed for drone-based image georeferencing. The position of each target was accurately measured (~3mm X, Y, Z) with an RTK GPS device Figure 4.1-c).




Figure 4.1. Experimental setting of the plots, with placement in the field (a), close-up example of a plot (b and c), and close-up of the funnel and runoff collector (d).

### 4.2.2 Rainfall data

A rain gauge was placed close to the plots to log rainfall amount data with a resolution of 0.3 mm/5 min for the whole duration of the experiment. To estimate the combined effect of rainfall duration and intensity on the evolution of soil crust, rainfall cumulative kinetic energy was chosen as an indicator, following the methodology adopted in the Chapter 3 of this manuscript (Crucil and Van Oost, 2021). To estimate the cumulative kinetic energy KE ($J \cdot m^{-2}$) applied during each measurement period, time-specific rainfall kinetic energy $KE_t$ ($J \cdot m^{-2} \cdot h^{-1}$) was first estimated using the universal

power law proposed by (Shin, Park and Choi, 2016), for each 5 min measuring time-step. KE was then estimated as the sum of $KE_t$ for each measurement time step during an event. This method is a simplification based on the assumption that the drop-size distribution is uniform in constant rainfall intensity. The cumulative kinetic energy KE was then calculated for each measured dry soil phase as the sum of kinetic energy since the start of the experiment (with the experiment starting conditions of freshly ploughed soil set at KE = 0 $J \cdot m^{-2}$).

### 4.2.3 Multispectral imaging

The multispectral sensors employed was a Micasense Rededge-M multispectral camera (described in Chapter 3.2.4). The camera was mounted on a Phantom 3 drone and operated on a fixed flight plan at 20 m of altitude, acquiring images every second. For optimal sensing conditions, all flight were executed when the combination of dry soil surface and clear sunny sky was present, within 2 hours from solar noon. A total of five flights were realized: the first flight before any rainfall input on seedbed soil (starting soil conditions); the subsequent four flights were evenly distributed across the measuring period, after significant rainfall events, when optimal flight conditions were available (Figure 4.2). A calibrated reflectance panel, provided by Micasense, was used to convert radiance data to reflectance. For each flight campaign, the image sets were merged in a multispectral orthomosaic using the software Pix4Dmapper (Pix4Dmapper SA, 2022), which also dealt with image correction, radiometric calibration, reflectance conversion, and provided a DSM. All orthomosaics were resampled to the resolution of 1.5 cm/pixel (average resolution among all flights). Following the methodology adopted in Chapter 3, maps of random roughness were then generated by calculating the standard deviation of the elevations on the residual topography in a moving square window of 5 x 5 pixels; pixels where the random roughness was above the threshold of 3 mm, which was visually assessed as appropriate to discard the soil clods, were then removed. Since multispectral images were acquired at high resolution, shadows cast on the soil surface by micro-reliefs were affecting a substantial portion of the soil surface. To solve this, the method for shadow elimination tested in Chapter 3 was also applied to the soil plots multispectral orthomosaics. Figure 4.3 reports an example of soil plot after shadow removal and roughness thresholding.

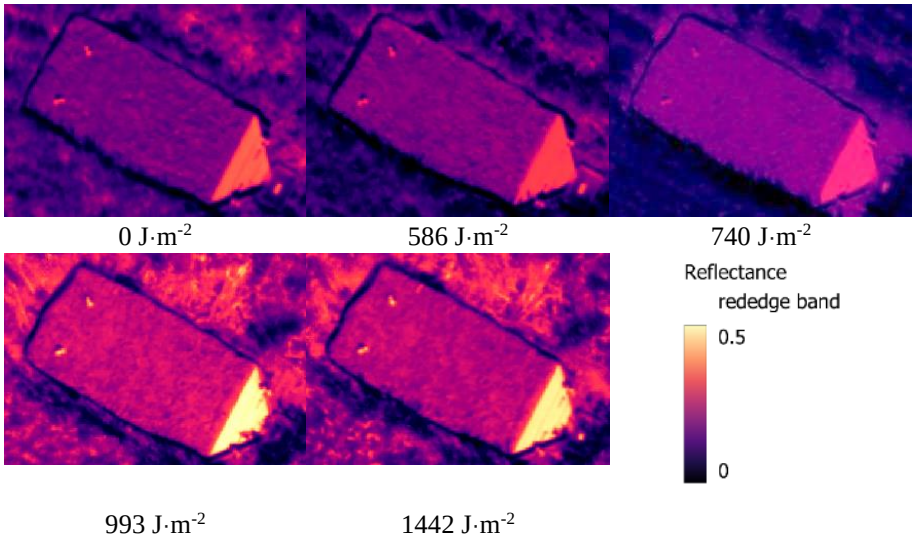


Figure 4.2 Example of a single plot evolution with increased levels of KE, as seen by the rededge channel of the multispectral camera. Associated KE levels are indicated below each image.

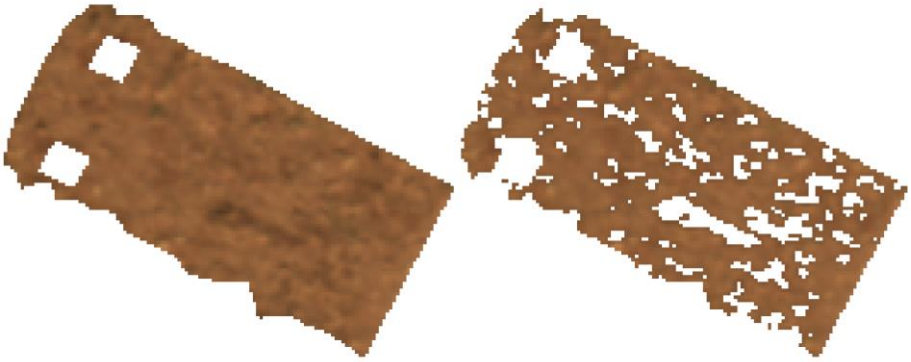

Figure 4.3. Example image, in false RGB, of a soil plot before (left) and after (right) shadow removal and roughness thresholding.

### 4.2.4 Hyperspectral sensing

The hyperspectral sensor was an ASD Fieldspec 3 FR spectro-radiometer sensor (described in Chapter 2.2.2). For the hyperspectral measures, the sensor head was set at c. 15 cm height above the soil surface, at the nadir

position, providing a measurement footprint with a diameter of c. 7.5 cm. Each single spectral acquisition with the ASD instruments was performed with an integration time of 5.4 seconds. 12 measurements were taken in combination with each UAS flight campaign, in a 4x3 grid distributed to evenly cover each plot (Figure 4.4). Radiometric calibration for the ASD was automatically managed by its hardware + software routine ($RS^3$ software from ASD). For the conversion of radiance to reflectance a Spectralon white reference surface measurement was repeated every ten samples. Bandwidths below 400 nm and above 2400 nm were removed because they typically contain excessive noise, as well as the bandwidths influenced by water vapour absorption in the intervals 1350-1450 and 1800-1950 nm. Spectra were also smoothed with a Savitzky-Golay smoothing filter (Savitzky and Golay, 1964) using a second order polynomial fit. Spectral outliers were removed, at each box/phase level, setting a threshold of three times the standard deviation of the Mahalanobis distance of the spectra projected in the first two latent variables of the principal component space.

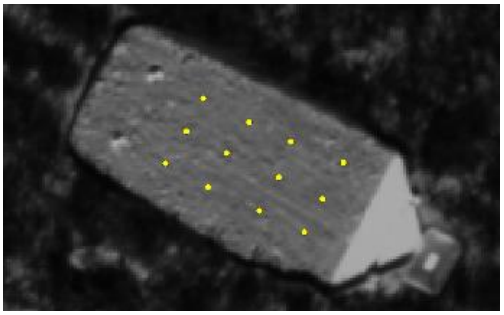

Figure 4.4. Distribution of hyperspectral measurement spots. They were distributed to evenly cover each plot in 4 rows at 30, 60, 90 and 120 cm from the outlet, with inter-column distance of 25 cm.

### 4.2.5 Spectral modelling of KE

Multispectral data were extracted from the orthomosaics using a regular sampling grid of 20 points inside each plot. In a radius of 15 cm around of each point (Figure 4.5-a) the mean and the inter-quantile range (*iqr*, as defined in Chapter 3.2.7) of the 5 spectral bands from available pixels was extracted. Sampling points with less than 50 pixels within each 15 cm radius were discarded.

From the multispectral data, PLSR models of KE were developed using: i) mean reflectance; ii) mean reflectance + *iqr*; iii) SNV transform; iv) SNV transform + *iqr*. A “Leave-one-out” cross validation was used to select the

optimal number of latent variables for each sub-dataset. The process is resumed in the workflow in Figure 4.5-b. The best PLSR model was selected based on the number of latent variables (PLSR components) above which a decrease in RMSE was not significant. To evaluate the stability and consistency of the models a validation was then performed splitting each dataset into calibration and validation (80% and 20%, respectively), with random selection and model re-calibration for 200 repetitions. The performance of the models was evaluated on the validation datasets using the mean of 200 simulations of the following metrics: i) MRE %, ii) RMSE, iii) $R^2$ and iv) RPIQ.

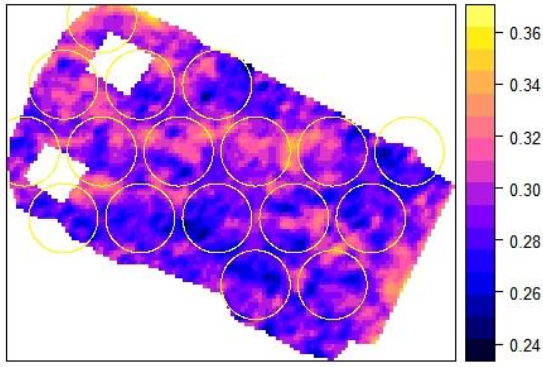


a

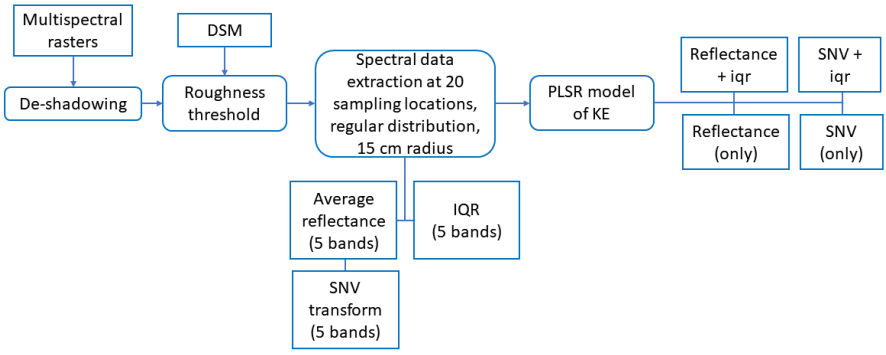


b

Figure 4.5. Example of sampling grid for extraction and averaging of multispectral data in a plot (a) and PLSR modelling flowchart (b).

### 4.2.6 Runoff and sediment data

Measured rainfall was first compared to records of the period 2000-2017, as measured by the nearby meteorological station of Wavre (about 3 Km north of the experiment site), to put them in context with the average precipitation regimes of the area (Figure 4.6). For the month of April, despite a measurement period of only the last 10 days, precipitations amounted to the monthly average, but were followed by relatively dry conditions for the full months of May and June (measured precipitation close to average minima). July measured rainfalls were close to the minimum too, but they comprised only the first nine days of the month. The distribution of the measured rainfall events is resumed in Figure 4.7. The KE amounts related to the five UAS flight measurement resulted in 0, 586, 740, 993 and 1442 $J \cdot m^{-2}$.

Runoff and sediment were naturally conveyed by gravity in the plastic bucket collector at the bottom of each funnel. Dried sediment leftovers on the funnel were manually included in the bucket at each collection. Sediment collection was executed nine times, following major storm events (Figure 4.7). Sediment weights were determined after drying the soil samples in the oven at 105 °C. Runoff was not considered in this study since, due to evaporation losses and long times between sample collection dates, it was not representative of the true amount. Relevant output variables were the grams of exported sediment (S), the grams of water runoff that generated it in each phase (Rf), and the sediment exported per unit of rainfall (S.Rf) calculated as ratio between the two parent variables. Antecedent KE levels were then associated with each measurement.

To evaluate the contribution of crust development on sediment generation, two modelling approaches were tested, corresponding to the two crust description methodologies adopted in this study:

- linear mixed modelling to predict the exported sediment S, using as input fixed effects the rainfall amount, both with and without the measured KE as complementary input. Plot identity was assigned as random effect. This was tested on the full dataset and on a sub-dataset excluding the first sediment collection (“fo” dataset).
- PLSR modelling to predict the exported sediment S, using as input the rainfall amount together with the multispectral indices from the sampling grid of each plot. This was tested on the data from the three multispectral datasets 2018/05/08, 2018/05/26 and 2018/06/30 and the

first sediment collection occurring after these UAS flights (respectively 2018/05/20, 2018/06/02, and 2018/07/07), as shown in Figure 4.7.

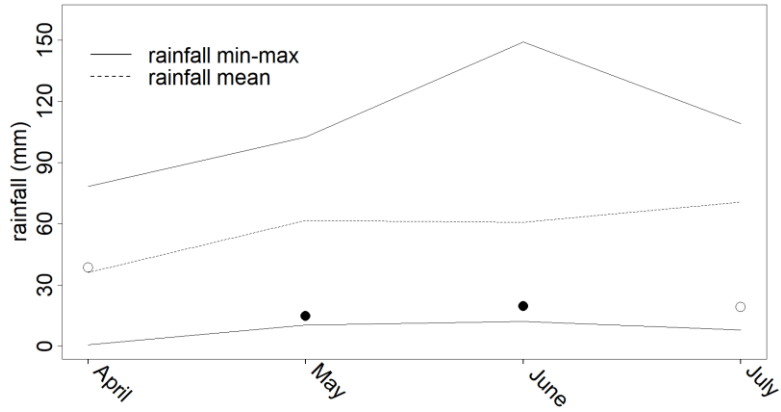


Figure 4.6. Monthly cumulated precipitations measured on the experiment plots, in the context of monthly average (dashed black line), minima and maxima (bottom and top full black lines) measured at the nearby Wavre meteorological station in the period 2000-2017. April and July are represented by empty dots as only part of those months was measured (last 10 days of April, first 9 days of July).

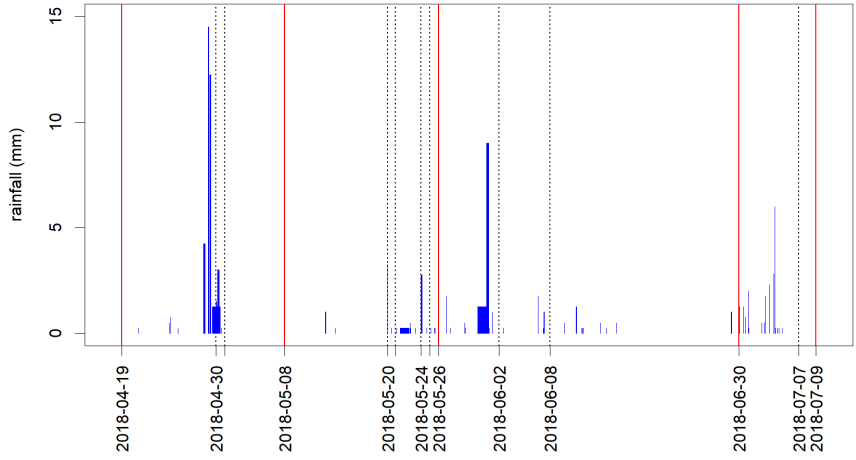


Figure 4.7. Data synopsis: blue bars for rainfall events (separated by at least 1 hour of no rainfall), red lines for drone flights, black dotted lines for runoff/sediment collection.

## 4.3 Results and Discussion

### 4.3.1 PLSR models of KE

Reflectance-based PLSR models of KE provided good results ($R^2$ = 0.71, RPIQ = 2.1) but were overestimating for initial soil conditions (at 0 KE, as appearing from Figure 4.8-a). On the other side, and contrary to the results of Chapter 3, SNV data provided the best model performances ($R^2$ = 0.8, RPIQ = 2.4, as summarized in Figure 4.8-b) and better prediction of the 0 KE (initial) soil conditions. The inclusion of the *iqr* terms, similarly to the results of Chapter 3 of this thesis (see Chapter 3, Figure 3.14), did not add useful information for modelling KE: reflectance + *iqr* obtained an $R^2$ = 0.71 and RPIQ = 2, while SNV + *iqr* an $R^2$ = 0.8 and RPIQ = 2.2. In Chapter 3, we did indeed assign *iqr* values to the spectral effects of microscale roughness (2 mm resolution) and not to KE induced surface/colour changes, and its effect was already insufficient to model roughness at 15 mm resolution. KE model validation results (Figure 4.8 for single points and Figure 4.9 for average results) showed a good consistency of KE prediction. Overall, modelling performance of KE/crusting with this experimental setup outperformed the results obtained with the soilboxes in Chapter 3 (see Chapter 3, Figure 3.14), but this is probably due to a much higher numerical sample availability (600 vs 42 samples) and a shorter and more uniform range of KE values.

Regarding the variable importance (summarized in Figure 4.10), multispectral reflectance and SNV data of this experiment confirmed the importance of the red channel already observed in Chapter 3, while more weight was given to the rededge and less weight to blue and green (see Chapter 3, Table 3.1). *Iqr* values, on the other hand, were completely discarded. Variable importance with hyperspectral data (Figure 4.10) showed that the SNV transformation highlighted the presence of peaks of information in the visible-NIR portion, rather than the whole region as provided by pure reflectance. With the SNV, new VIP peaks were obtained at 730 nm (in correspondence of the Micasense rededge channel) and at 760 nm, and the peaks already individuated in Chapter 3 at 930 and 1130, 1950, 2000, 2140 and 2200 nm were confirmed also in this study. While the 2140 and 2200 nm peaks were already described by other studies (Ben-Dor *et al.*, 2003; Eshel, Levy and Singer, 2004), a specific physico-chemical investigation would be desirable for the individuation of other specific chromophores. In particular, the relevance of reflectance in the whole visible range and a SNV peak at 940 nm, also observed in soil organic carbon modelling (Figure 2.6),

calls for a scrutiny of possible confounding factors in crust spectral modelling of soil samples with different SOC content. Overall, in accordance with the expectations, the SNV transformation seemed to have effectively compensated for the differences in baseline albedo, allowing the models to target more specific changes in soil surface texture and composition, resulting in better prediction performance. The relative difference in importance between the multispectral broad-bands, however, was not prominent as with the hyperspectral data. More observations, possibly with different soil characteristics, are needed to validate these results.

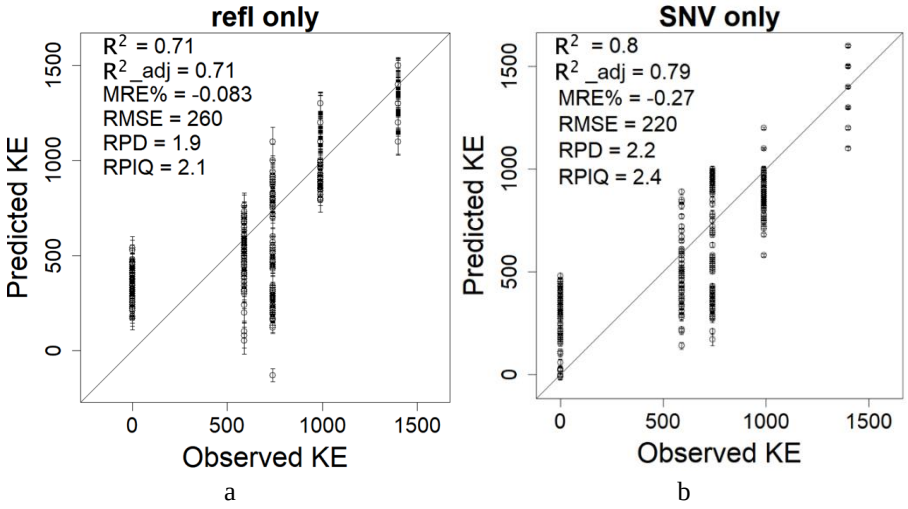


Figure 4.8. Observed vs Predicted KE values from the validation phase of PLSR modelling of multispectral data, with different reflectance data types: a) reflectance; b) SNV of reflectance. Each point shows the boxplot of the standard deviation of predicted values from the validation process. Plot results from the "*iqr*" dataset were omitted.

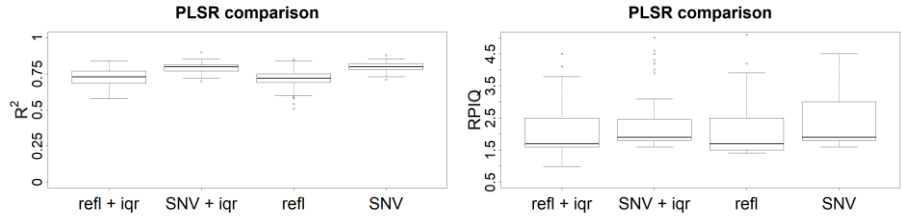


Figure 4.9. $R^2$ and RPIQ random resampling validation results from PLSR models of KE.

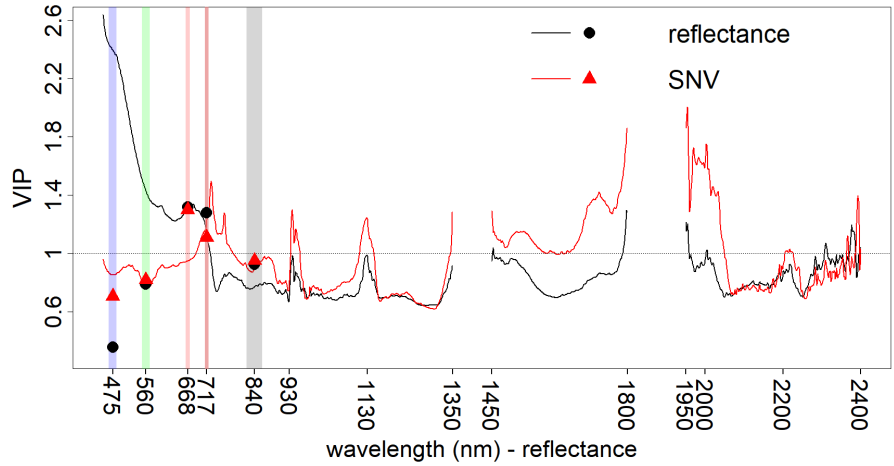


Figure 4.10. Variable importance (VIP) from PLSR models of KE, from both hyperspectral (lines) and multispectral (points) data, with reflectance (black) and standard normal variate (red). The spectral broad-bands of the Micasense Rededge, used in this study, are visualized as coloured strips.

### 4.3.2 Sediment modelling

Figure 4.11 summarizes the results of the data collection of sediment and rainfall. Pearson's correlation between variables was calculated both with the full data series and with the exclusion of the first rainfall measurement ([1] in Figure 4.11). The exclusion of the effect of the first event was motivated by the fundamentally different conditions between freshly harrowed soil, and all other subsequent experimental phases: these initial soil conditions are indeed usually characterized by a high availability of loose material prone to slaking and kinetic dispersion from rain drops, while the subsequent development of a shielding layer and crusting reduces sediment availability (Le Bissonnais and Singer, 1992; Kim and Ivanov, 2014). During our

monitoring period, the first rainfall event coincidentally was also the strongest of our measured series, further outlying the conditions of the first sediment collection. Sediment exported from the plots (S) was in both cases highly correlated with the rainfall (Rf) that directly generated it (r = 0.93 and 0.92, respectively, with and without first event). KE correlation with S changed from negative (r = - 0.4) to positive (r = 0.65) by omitting the first rainfall event, and became significant with S.Rf (r = 0.33). Slope and residue cover showed no correlation with S or S.Rf, and for this reason a coefficient of variation of sediment yield was calculated, for each data collection, considering all plots together. For the nine registered events the coefficient of variation ranged from 10.6% to 32.5%, with the higher values associated to the highest rainfalls (r = 0.69, $p < 0.05$). The results of the two modelling approaches for exported sediment S (summarized in Figure 4.12) showed that adding the measured KE term or the multispectral indices as a predictor together with rainfall amount did not improve modelling performance. In the linear mixed models using measured KE, $R^2$ remained indeed stable at 0.87 with the full dataset, while it only increased from 0.84 to 0.87 when excluding the first data series ("fo" results in Figure 4.12), with RPIQ decreasing. Modelling the increase of the S.Rf ratio with KE yielded poor results, both with the full dataset ($R^2$ = 0.01) and with the first measurement excluded ($R^2$ = 0.11). Using the multispectral indices in place of KE (only the best result is here reported, the SNV without *iqr*), yielded a slightly lower $R^2$ of 0.81, offset by a higher RPIQ of 4.8. The S.Rf prediction performance, on the other hand, resulted slightly improved ($R^2$ = 0.42, RPIQ = 2.6)

Soil antecedent conditions of cumulative rainfall kinetic energy, as it appeared from this experiment setup, did not play an important role in controlling sediment yields, which were instead well explained by rainfall alone. The lack of a meaningful effect of KE-induced soil crusting in our plots was possibly due to a scale effect: very small and isolated plots, missing a sensible upstream contribution, are not able to generate a proper runoff and thus often underestimate sediment yields in comparison to larger plots (Boix-Fayos *et al.*, 2006); the limited runoff of small plots also limits the erosion processes to the interrill type, which has been observed to be of minor or negligible importance as compared to the rill type (at least for loamy soils). Conversely, rill type erosion has been reported to initiate only on bigger surfaces, like 22 m x 8 m "USLE-type" plots (Bagarello and Ferro, 2004). Furthermore, the limited time scale and amount of precipitations during our measurement period may have not been sufficient for a transition from a

transport limited regime to a sediment limited regime (Kim and Ivanov, 2014) when the effect of crust on runoff generation is more significative (Le Bissonnais and Singer, 1992). Given these considerations, it is possible that sediment yields produced by our experimental setup were, for the most part, due to kinetic displacement of soil particles from raindrop impact instead of runoff.

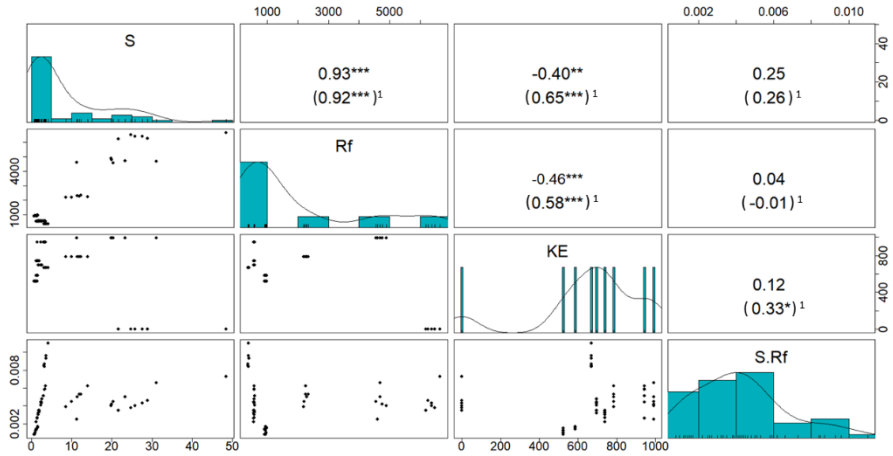


Figure 4.11. Scatterplot and Pearson's correlation of sediment and precipitation data: S = dry sediment (g), Rf = total rainfall (g) applied on plot during a single measuring period, KE = total kinetic energy cumulated on plot before the measuring period, S.Rf = soil eroded per unit of input rainfall. Significance codes (p-values): 0 < '***'< 0.001 <'**'< 0.01 <'*'< 0.05 <'.'< 0.1 <' '< 1. Correlation values between brackets ([1]) were calculated omitting the data from the first measurement ("fo" dataset at KE = 0).

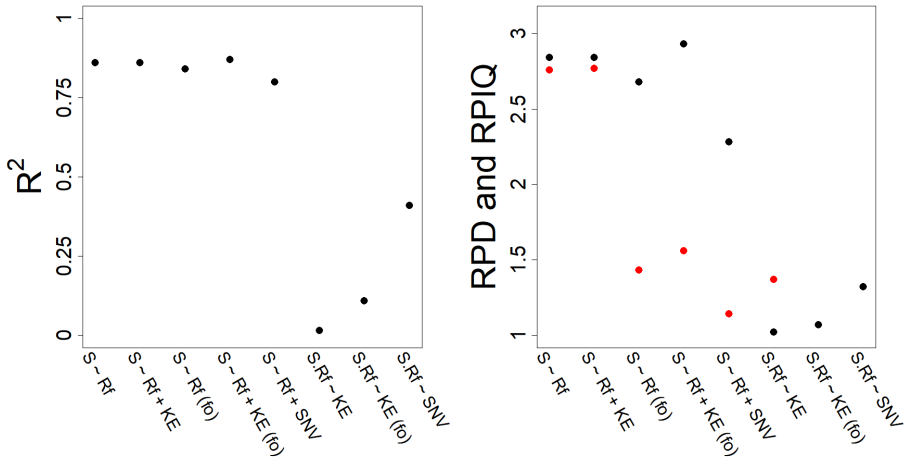


Figure 4.12. Model results, in terms of $R^2$, RPD and RPIQ, for sediment (S) and sediment for unit of rainfall (S.Rf) prediction. Predictor variables were the rainfall generating each specific sediment export (Rf), the measured, previously cumulated kinetic energy (KE), the standard normal variate of the Micasense rededge spectra (SNV). Type of model is indicated under the horizontal axis. RPD values in are marked in black, RPIQ in red. (fo) indicates dataset where the first measured rainfall was excluded

## 4.4 Conclusions

A methodology to monitor soil surface crust evolution with multispectral imaging, using rainfall kinetic energy (KE) as proxy, was developed and validated in laboratory conditions in Chapter 3. This same methodology has been now successfully applied on an experimental setup of a series of small loamy soil plots in real field conditions, using multispectral images from low altitude UAS flights. The experiment showed that the five vis-NIR spectral broad-bands of a commercial grade multispectral camera were sufficient to predict ($R^2$ = 0.79) a series of KE levels by simply removing shadows and normalizing the spectra from albedo increases through a SNV transformation. A close-proximity vis-NIR-SWIR hyperspectral analysis of the same soil surfaces highlighted some specific spectral features linked to crust development, one of which corresponded to the camera rededge band, further supporting the results. These results represent a first step into the UAS-based remote sensing assessment of soil physical crust development at the wider scales of fields or small basins. Studying the complications of soil moisture, vegetation residue and differences in SOC on spectral crust description represent the necessary further steps.

A complementary collection of soil eroded and exported from the plots did not show a significant correlation between increased soil crust development and sediment export. Due to the experiment design, it was also not possible to measure with accuracy the amount of water runoff and associate its increase to crust development, as documented in the laboratory trials of Chapter 3. It was concluded that to attempt the association of a spectral-based soil crust model to changes in infiltration rates and sediment generation it would be desirable to have: i) bigger plots, possibly spanning 20 m in length to avoid limitations in erosion and sediment transport regimes and to be comparable with similar studies; ii) a longer measurement period for more extensive rainfall data and overcoming occasional dry periods; iii) more accurate water runoff measurements. A thorough instrumental description of soil crust development, regarding its physico-chemical changes, should also accompany the spectral data for proper model development.

# Chapter 5

# A semi-empirical anisotropy correction model for UAS-based multispectral images of bare soil

*The content of this chapter is based on the published article:*
*Crucil, G.; Zhang, H.; Pauly, K.; Van Oost, K. A Semi-Empirical Anisotropy Correction Model for UAS-Based Multispectral Images of Bare Soil. Remote Sens. 2022, 14, 537. https://doi.org/10.3390/rs14030537*

## Abstract

The recent developments in performance and miniaturization of Unmanned Aircraft Systems (UAS) and multispectral imaging sensors provide new tools for the assessment of the spatial and temporal variability of soil properties at sub-meter resolution and at relatively low costs, in comparison to traditional chemical analysis. The accuracy of multispectral data is nevertheless influenced by the anisotropic behaviour of natural surfaces, framed in the general theory of the Bidirectional Reflectance Distribution Function (BRDF)**.** Accounting for BRDF effects in multispectral data is paramount before any scientific interpretation. This study presents a semi-empirical spectral normalization methodology for UAS-based multispectral imaging datasets of bare soils to account for the effects of the BRDF, based on the application of an Anisotropy Factor (ANIF). A dataset of images from 15 flights over bare soil fields in the Belgian loam belt was used to calibrate a model relating the ANIF to a wide range of illumination geometry conditions by using only two angles: relative sensor-pixel-sun zenith and relative sensor-pixel-sun azimuth. The employment of ANIF-corrected images for multispectral orthomosaic generation with a photogrammetric software provided spectral maps free of anisotropic related artefacts in most cases, as assessed by several ad-hoc indexes, and was also tested on an independent validation set. Most notably, the standard deviation in measured reflectance of the same georeferenced point by different pictures decreased from 0.032 to 0.023 ($p < 0.05$) in the calibration dataset and from 0.037 to 0.030 in the validation dataset. The validation dataset, however,

showed the presence of some systematic error, the causes of which requires further investigation.

## 5.1 Introduction

The previous chapters of this thesis showed how diffuse reflectance soil spectroscopy with small UAS-based sensors can provide a good alternative to enhance or replace conventional methods of soil analysis, as it is rapid, timely, less expensive, non-destructive, and allows for the simultaneous characterization of various soil properties. The accuracy of spectral remote sensing, however, is challenged by environmental conditions (illumination and atmosphere interactions), measurement protocols, data-processing procedures, and specific sensor characteristics. It is thus critical to understand both the potential and limitations of this technology before using its data products to study earth system processes (Aasen *et al.*, 2018).

One of the biggest challenges for spectral sensing is that the reflectance of natural surfaces shows anisotropic behaviour, i.e., measured reflectance varies with illumination and viewing geometry. This results in spectral variability not only from different angular measurements and times of the day, but also within the field of view of single images. The theoretical framework for modelling the angular effects occurring between illumination source, sensor and measured surface and has been formulated as the BRDF (Nicodemus, 1977). Several physical, empirical or semi-empirical models have been developed in attempt to normalize spectral data with the parametrization of the BRDF (Beisl, 2001). Traditionally, BRDF model calibrations were obtained by performing multi-angular reflectance measurements using complex goniometer setups, but nowadays aerial digital imaging provides an alternative platform to field goniometer systems for performing multi-angular reflectance measurements (Roosjen *et al.*, 2017). The advantage in the employment of imaging setups lays in the fact that the field of view of each single image can provide a range of measurement geometries, and thus spectral interactions between illumination source and measured surface (Aasen and Bolten, 2018). In this regard, several empirical methods were developed to use the statistics of images taken on flat homogeneous surfaces to normalize off-nadir reflectance values with those obtained at nadir, with the use of an Anisotropy Factor (ANIF) (Sandmeier *et al.*, 1998; Schlapfer, Richter and Feingersh, 2015).

Addressing BRDF related issues in data from remote sensing and imaging spectroscopy is of primary importance to ensure their accuracy, before attempting any further analysis. Since a few years, UAS-multispectral data have been used to infer the spatial variability of soil properties at very high spatial resolution. However, to the best of our knowledge, a thorough understanding of the bias introduced by using uncorrected image datasets is still very limited and a generally applicable workflow to construct and apply bare soil BRDF models is not available. Preliminary analysis from our own bare soil multispectral datasets that were not corrected showed that the resulting orthomosaics exhibited prominent spectral aberrances in the form of "stripes" of different reflectance intensity, parallel and coinciding with the drone flight lines. The full potential of multispectral imaging for bare soil applications is therefore not fully reached.

The primary objective of this article is to elaborate a semi-empirical correction methodology for multispectral imaging datasets to account for the effects of the BRDF, based on the calculation of an Anisotropy Factor (ANIF) calibrated from UAS-based hemispherical-directional (Sandmeier *et al.*, 1998; Menzies Pluer *et al.*, 2020) bare soil reflectance measurements. A secondary objective is to evaluate the benefits of this correction method on the quality of SfM-based multispectral orthomosaics, using an elaborated UAS data collection campaign of 15 flights conducted in the Belgian loam belt.

To accomplish this, sensor position and orientation data obtained from GPS measurements and SfM-based bundle adjustment algorithms were used to relate observation and illumination angles to soil anisotropy effects at the image level. Resulting data were then used to test different modelling approaches and to provide a consistent image correction workflow. Finally, the orthomosaic products obtained with a commercial SfM software using original and corrected images were analytically compared for an analysis of the reduction/elimination of the "striping" artefact and the stability of spectral measurement when explicitly considering for BRDF effects in bare soils.

## 5.2 Materials and Methods

### 5.2.1 Multispectral imaging system

The multispectral imaging system used to collect data was a MicaSense RedEdge-M (described in Chapter 3.2.4). A diffuse irradiance sensor array

with similar spectral band characteristics (the so-called Downwelling Light Sensor, DLS) is mounted on top of the drone in the same optical axis as the camera array and is wired to the main unit to provide synchronized irradiance data. The DLS unit also includes an on-board standalone L1 GPS and Inertial Measurement Unit (IMU) to provide location and orientation measurements (positioning accuracy of 2-5/10 m in xy/z, and orientation accuracy of 2-5/5-15° in roll, pitch/yaw). The multispectral imaging system stores a set of 5 TIFF image files (corresponding to the spectral bands) for every image acquisition point, for which their respective irradiance level and a common GPS position and IMU orientation are saved in the image EXIF and XMP metadata. A calibrated reflectance panel (CRP) of ca. 50% grey reflectance provided by the camera manufacturer was used to convert raw image radiance values to reflectance.

### 5.2.2 Data collection and pre-processing

A series of UAS flights with the Rededge-M rigidly mounted on a custom made quadcopter drone was conducted over bare soil fields in the Belgian loam belt between 2018 and 2021 (flight information is summarized in Table 5.1, locations are shown in Figure 5.1-a,c). The flights were conducted during clear sky conditions, on dry soil. The fields were in seedbed conditions, with very low roughness (example provided in Figure 5.1-b), very low stoniness, no growing vegetation and very limited vegetation residue. Soils in the area are classified as silt-loam by texture according to the USDA classification. Flight altitude was ca. 45 m above ground level, resulting in ca. 3 cm ground sample distance (GSD). Flight speed was set to 5-6 m/s to ensure a frontal image overlap of 80%, while interline distance was set to obtain a lateral image overlap of at least 75%. Flight plans were designed with a GIS software and then executed using the DJI GSPro application (version 2.0.15) (SZ DJI Technology Co., 2018). The camera was mounted on the UAS in a fixed position, with a frontal tilt (pitch) manually adjusted to provide almost nadir position at the chosen flight speed and with the UAS always turning the head to the flight direction. Flight lines were oriented along the long edge of the field to provide maximum coverage efficiency, while resulting in variable solar azimuth angles (given in Table 5.1).

PIX4Dmapper (Pix4Dmapper SA, 2022) was the SfM photogrammetric software used in this study for multispectral reflectance orthomosaic generation. PIX4Dmapper organizes the image processing workflow in three phases: i) initial processing for key-points identification and camera

calibration (for both interior and exterior orientation parameters); ii) point cloud densification; iii) DSM (Digital Surface Model) and multispectral orthomosaic generation. The first two phases were executed with the same processing options with both the original and the corrected image datasets. The first phase was of primary importance to obtain the adjustment of the camera orientation parameters ω, φ, κ (rotation with respect to the target projected coordinate system): since the original camera inertial navigation measurements can have inaccuracies up to about 5-20°, more accurate values coming from bundle adjustment algorithm were deemed necessary for the calibration of our ANIF model. The third phase differed in the choice for radiometric calibration, vignetting correction, black level compensation and final conversion to reflectance: automatically managed by Pix4Dmapper for the original orthomosaics versus manually pre-calculated on the input images for the corrected orthomosaics. In this last case, radiometric calibration, vignetting correction, black level compensation and final conversion to reflectance for the Rededge-M images were performed following the procedure described on the manufacturer's website (*RedEdge Camera Radiometric Calibration Model*, no date) using the software R (R Core Team, 2021).

Table 5.1. General flight information of the UAS-flights database: name, execution date, lateral overlap %, flight line and sunlight direction, and whether the dataset has been used for ANIF model calibration or validation. Names marked with an (*) represent datasets that in the original orthomosaic generation phase showed a prominent "striping" artefact effect. Flight altitude was ca. 45 m above ground level in all cases.

| Field name | Date | Lateral Overlap (%) | Flight line azimuth (deg) | Sun azimuth (deg) | Sun Zenith (deg) | Model calibration/ validation |
|---|---|---|---|---|---|---|
| Seumoy | 07/05/2018 | 80 | 60/240 | 220 | 38 | Cal |
| Thorembais* | 07/05/2018 | 75 | 40/220 | 150 | 37 | Cal |
| Beuzet Sud | 08/05/2018 | 75 | 127/307 | 240 | 46 | Cal |
| Hostellerie* | 02/09/2018 | 75 | 65/245 | 140 | 49 | Cal |
| Geeste 1 | 02/09/2018 | 75 | 67/247 - 147/327 | 160 | 44 | Cal |
| Geeste 3 | 02/09/2018 | 75 | 65/245 | 190 | 43 | Cal |
| Ernage* | 20/04/2019 | 75 | 35/215 | 140 | 44 | Cal |
| Villeroux a1* | 27/08/2019 | 80 | 45/225 | 200 | 42 | Cal |
| Villeroux a2* | 14/09/2019 | 80 | 45/225 | 190 | 47 | Cal |
| Gembloux F2* | 23/04/2021 | 60 | 115/295 | 130 | 47 | Cal |
| Gembloux F3* | 23/04/2021 | 60 | 115/295 | 190 | 38 | Cal |
| Gembloux F4* | 23/04/2021 | 60 | 115/295 | 230 | 49 | Cal |
| Marbaix West | 06/05/2018 | 75 | 35/215 | 150 | 37 | Val |
| Beuzet Nord | 08/05/2018 | 75 | 140/320 | 230 | 42 | Val |
| Sicy* | 02/09/2018 | 75 | 150/330 | 130 | 52 | Val |




(**a**)



(**b**)

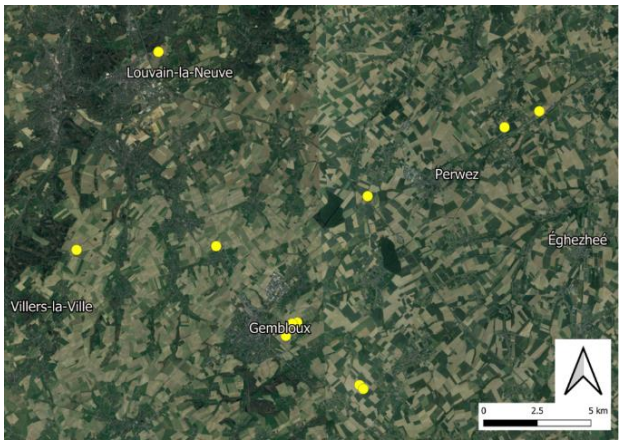


(**c**)

Figure 5.1. Locations within Belgian border (a), and more in detail within the Belgian loam belt area (c), of the UAS flights used in this study. A close-up example of soil conditions is reported in frame (b).

### 5.2.3 ANIF correction model

An empirical correction methodology for spectral imaging is proposed to account for the effects of the BRDF, based on the calculation of an Anisotropy Factor (ANIF) from drone-based hemispherical-conical (Schaepman-Strub *et al.*, 2004) reflectance measurements (in the context of this study, given that the pixels of imaging spectrometers have fairly small measuring cones, their measurements are treated as an approximation of directional measurements and the resulting quantities as hemispherical-directional reflectance factors (Aasen and Bolten, 2018)). The ANIF represents the ratio between reflectance measured at nadir position and reflectance measured at other angular positions in an imaging sensor. The application of this factor aims at normalizing reflectance values at each pixel position with those measured at nadir. Since reflectance anisotropy is related to the combination of viewing geometry (sensor azimuth and zenith) and illumination geometry (solar azimuth and zenith), a geometric modelling approach of the relative sensor-pixel-sun angles was tested to model the ANIF.

For model calibration and to isolate the effects of directional reflectance on soil images, twelve flights (indicated in Table 5.1) were selected for the

conjunction of high homogeneity of soil colour, low roughness (seed-bed conditions), and low/no slope. Within the image dataset of each flight, a subset of about 25-30 images (per spectral band) shot from the centre of each field was selected to obtain images exclusively representing flat, homogeneous, bare soil. These images served as model calibration dataset. Radiometric calibration, vignetting correction, black level compensation and final conversion to reflectance for the Rededge-M images were manually performed as indicated in the previous chapter. The workflow then proceeded with the identification of the nadir pixels (Figure 5.2) and the calculation of their relative sensor and sun angles (Figure 5.3). For each image, the distance in pixel units between the image optical centre (provided by the manufacturer factory calibration) and the pixel coordinates representing the surface point where the sensor was at nadir position were calculated as Equation (5.1) and Equation (5.2):

$$u = F \cdot \tan(\varphi) \tag{5.1}$$

$$v = F \cdot \tan(\omega) \tag{5.2}$$

where u is the pixel column number, v the pixel row number, F the camera focal distance in pixel unit, φ the adjusted sensor Y orientation, ω the adjusted X sensor orientation. This allowed to locate the "nadir" pixel coordinates (Figure 5.2). The ANIF map for each image was then calculated as the ratio between average reflectance in a 5 degrees diameter around the nadir and each other pixel. The adjusted sensor azimuth κ and the solar azimuth from R solar almanac package "suncalc" (Benoit Thieurmel and Elmarhraoui, 2019) were then used to calculate, for each image, the map of the relative azimuth (Figure 5.3) between each image pixel, the nadir pixel, and the sun azimuth (*Rel_az*). Relative azimuths were calculated in a 0-180 degrees reference system with 0 degrees coinciding with the same direction of solar rays and 180 degrees opposing the sun. The sensor zenith angle (*PS_zen*) was calculated as angle between each pixel, the focal point, and the nadir pixel by applying the law of cosines Equation (3.3):

$$PS_zen = arccos\left(\frac{FP^2 + FN^2 - NP^2}{2 \cdot FP \cdot FN}\right) \tag{3.3}$$

from the reference system of the internal camera parameters, where FP is the distance between the focal point and each pixel, FN the distance between the focal point and the nadir, and NP the distance between the nadir pixel and each other pixel (all distances in pixel units). Finally, image

maps of the relative sensor-pixel-sun zenith (*Rel_zen*) was then calculated as Equation (5.4):

$$Rel_zen = PS_zen \cdot \cos(Rel_az) + Sol_zen \quad (5.4)$$

where *Sol_zen* is the solar zenith from the solar almanac, calculated from the vertical.

From the maps obtained in the image calibration dataset, the ANIF values were extracted and analysed in correlation to *Rel_az*, *Rel_zen* and *PS_zen* values. The calibration data from the 12 selected flights were merged to represent the entire available range of hemispherical illumination and observation angles (1000 regularly distributed ANIF values per dataset, for a total of 12000 calibration values). Based on the observed relationships, several model equations with different combinations of the input angles were tested and compared for the best ANIF prediction. The performance of the best model was then assessed in the calibration procedure and subsequently on three validation datasets (1000 regularly distributed ANIF values per dataset, for a total of 3000 calibration values), obtained in the same way as for the calibration dataset. $R^2$, RMSE and MRE% were used as model fit evaluators. The general workflow adopted for the calibration and application of the ANIF correction is resumed in Figure 5.4.

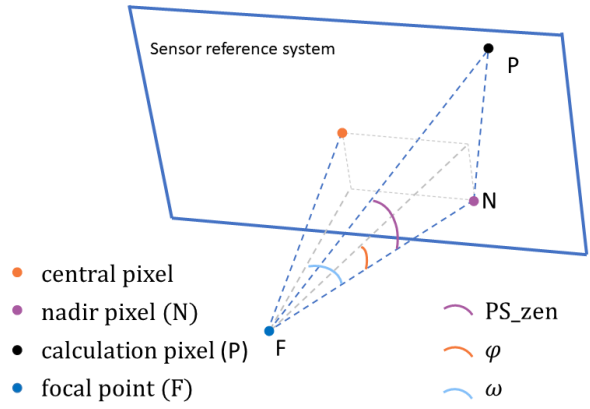


Figure 5.2. Scheme for the calculation of the pixel nadir coordinates and of the sensor zenith relative to the nadir "PS_zen" angle in a tilted (by pitch and roll angles) sensor reference system.

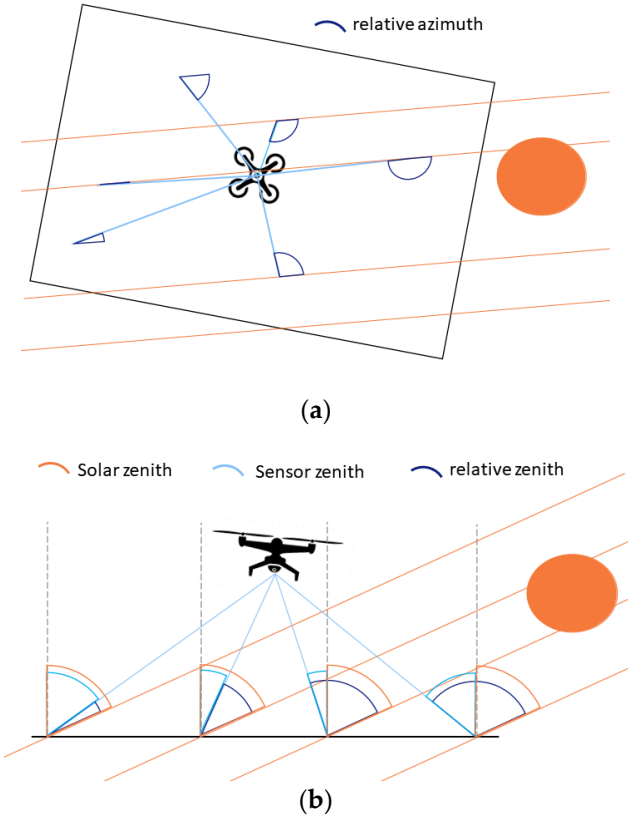


Figure 5.3. Visualization of the relative angles extracted for BRDF modelling within the sun-pixel-sensor framework: a) relative azimuth "*Rel_az*"; b) sensor zenith "*PS_zen*", solar zenith "*Sol_zen*", relative zenith "*Rel_zen*".

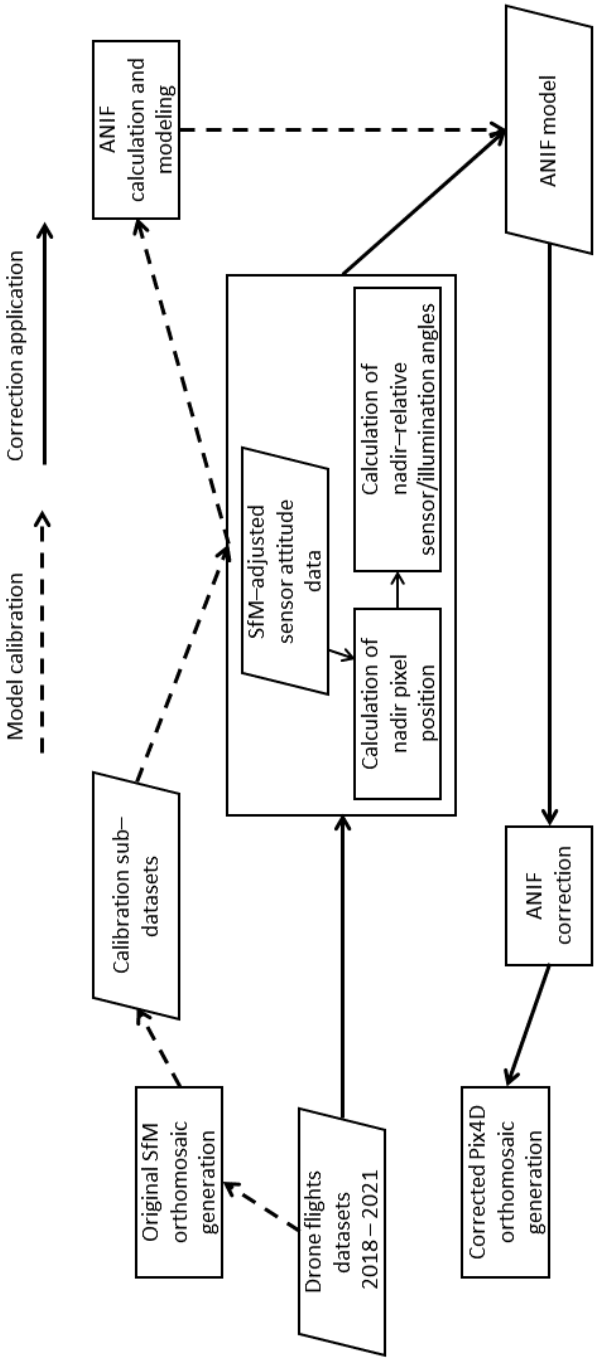


Figure 5.4. Workflow for ANIF model calibration and application.

### 5.2.4 Correction evaluation

The optimal ANIF correction model was then applied to all available datasets, where the datasets that were not used for calibration were used for validation (distinction marked in Table 5.1, last column). Images were first converted to reflectance, then *Rel_zen* and *PS_zen* angles were calculated to predict and apply the ANIF. The corrected images were then used in PIX4Dmapper for corrected orthomosaic generation, bypassing the camera radiometric calibration and reflectance calculation routine provided in the software. Two steps of correction evaluation were then executed: the first (i) on the images of both calibration and validation datasets, the second (ii) on a subset of orthomosaics, selected visually, that showed distinct "striping" effects (indicated with an * in Table 5.1 names).

During step (i), to quantify the efficacy of reflectance normalization at the image level, the change in reflectance of the same pixel location coordinates observed from different contiguous images (overlapping FOV but with different shooting time, position, and orientation) was studied before and after correction application. This was accomplished by selecting a set of 220 sample pixels from the orthomosaics of the calibration dataset (12 flights) and 80 sample pixels from the validation dataset (3 flights) and tracking their corresponding pixel in all their "parent" images. Between 8 and 20 parent images were identified per pixel sample. The standard deviation (*sd*) of the reflectance of these parent pixels across different images was then compared between original and corrected images datasets. A substantial reduction in standard deviation after correction is then assumed as indicative for an efficient ANIF correction.

In step (ii), to quantify the "striping" effect in each orthomosaic, before and after the correction, spectral data were extracted from 8-10 transects positioned perpendicularly to the stripes. In this way the stripes were expected to appear as spectral peaks and valleys along the transects. The positions of the drone flight lines were then overlaid on the transects, and this allowed to study magnitude of the striping effect in relation to the flight line positions. A "spectral sinuosity" index (*SSin*), and the correlation between the magnitude of spectral peaks/valleys and the distance from the drone flight lines. *SSin* was calculated as Eq. (5):

$$SSin = \frac{\sum_{p=1}^{N-1} \sqrt{(r_p - r_{p+1})^2 + l^2}}{N \cdot l} \quad (5)$$

where N is the number of pixels along the transect, $p$ the pixel index along the transect, $r$ the reflectance (0-100 scale), $l$ the average pixel length on the transect (m). It is the ratio between the transect distance weighted by its pixel-by-pixel spectral variability and the real planimetric distance, with domain *SSin* ≥ 1, where the minimum value of 1 means no spectral variability across transect distance. The average *SSin* of all transects of a map is then calculated.

To calculate the correlation between striping and distance from the flight lines, the magnitude of the peaks/valleys was associated to the residuals of a linear interpolation of the reflectance values along each transect. The correlation was then calculated between these residuals and the horizontal distance to the closest flight line. The underlying assumption is that, in an ideal multispectral image dataset free of anisotropic effects, reflectance changes should not show correlation with distance to the image capture positions.

## 5.3 Results

### 5.3.1 Striping issue

The effects of soil reflectance anisotropy on the products of our UAS-based multispectral survey were evident both on the images and on the final products of the photogrammetric orthomosaic reconstruction. A spectral gradient in apparent correlation with the direction of incoming sunlight was evident on all images (e.g. in Figure 5.5-a), in accordance with previous observations on the differences between forward- and back-scattering reflectance of soil surfaces (Brennan and Bandeen, 1970; Milton and Webb, 1987; Anderson and Croft, 2009; Croft, Anderson and Kuhn, 2012). With the camera forward tilted in a fixed position to constantly aim at the nadir during cruising speed, such spectral gradient was invariant from the changing drone heading. We therefore excluded any other major systematic effect on measured reflectance (i.e. due to the camera orientation) than illumination direction. The combination of this systematic gradient behaviour and the regular geometry of flight lines used for image acquisition resulted in spectral artefacts in the final products of photogrammetric orthomosaic reconstruction. These artefacts (example in Figure 5.5-b) manifested as stripes of different spectral intensity, parallel and in concomitance with flight lines. When observed along transects perpendicular to the flight lines (e.g. in

Figure 5.6-a), these stripes took the form of spectral peaks and valleys (e.g. in Figure 5.6-b).

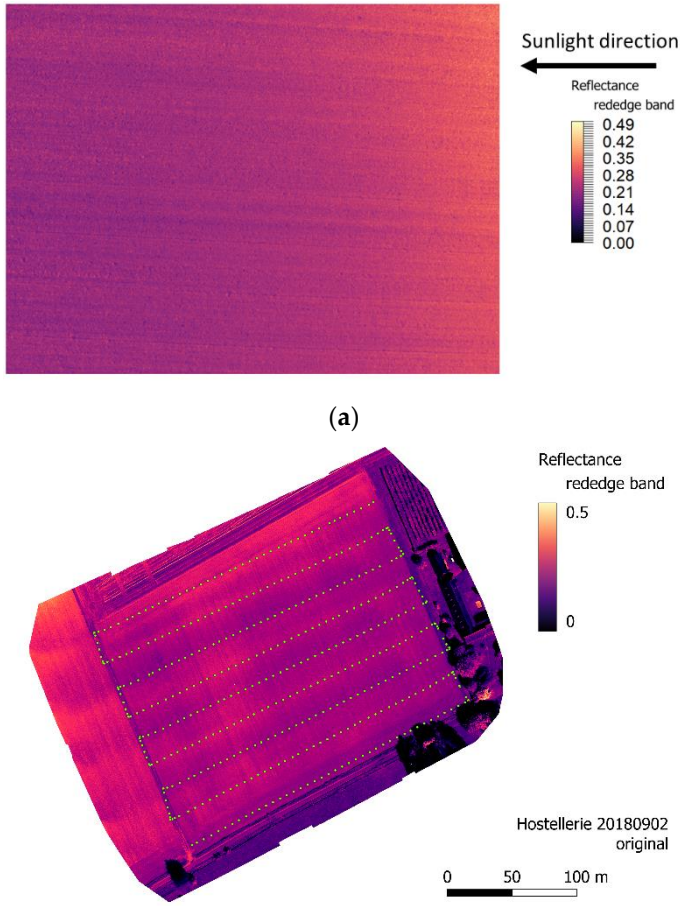


Figure 5.5. a) example of Micasense Rededge picture of flat soil, shot from 45 m above ground level, after manual radiometric calibration, vignetting correction, black level compensation and conversion to reflectance (rededge band as example): to be noted how it is affected by reflectance gradient due to back- and forward-scattering effects of incoming sunlight; b) example of Pix4D-generated spectral orthomosaic (rededge band as example) obtained from a dataset of images non corrected for the soil anisotropy effects. The image positions, along the flight lines, are put in evidence (green dots) to show their correspondence with the “stripes” artefact. The rededge band has been arbitrary chosen for display purposes only, as all spectral bands exhibited the same behaviour.

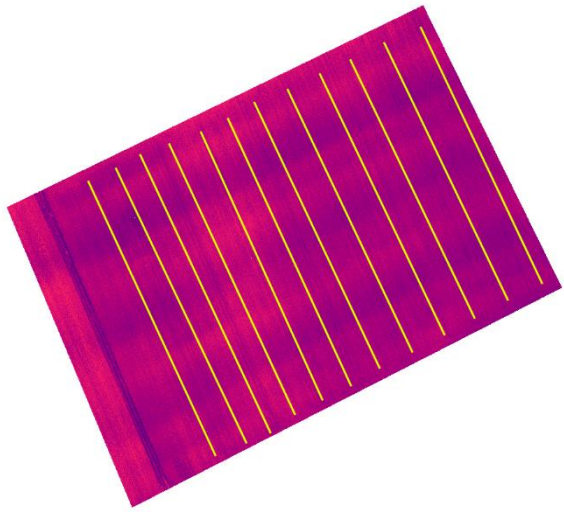

(**a**)

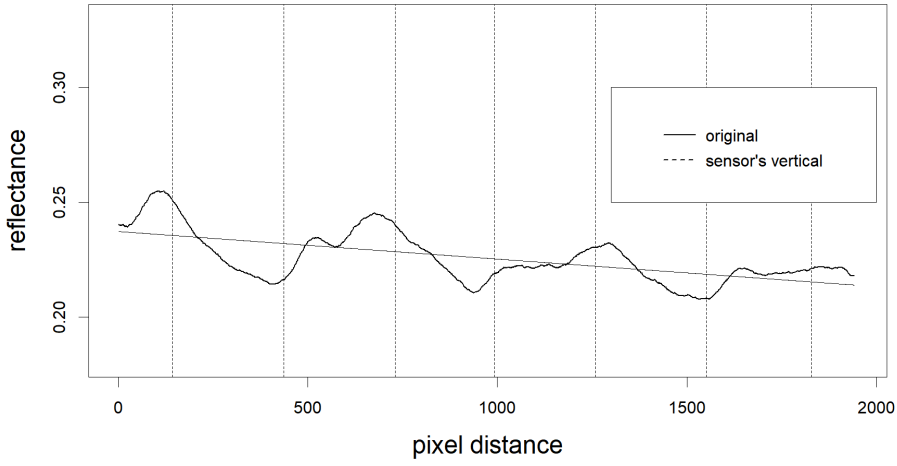


(**b**)

Figure 5.6. a) Example of transect drawing on a map affected by the stripes artefact; b) Example of transect spectral data, from the original dataset, and the corresponding linear interpolation. The position of flight lines (sensor vertical position) is indicated as black dashed lines.

### 5.3.2 Model fit

The results of the calibration data extraction are summarized in Figure 5.7, where the correlation plots show that both *Rel_az* and *Rel_zen* exhibit a stable behaviour with the ANIF across all sampled conditions of solar illumination. Different equation arrangements of the *Rel_az*, *Rel_zen*, and *PS_zen* angles were tested for their overall ANIF prediction capability and for

their image correction capability. The chosen form of the final model was Equation (5.5):

$$ANIF \sim a \cdot Rel_zen^1 + b \cdot Rel_zen^2 + c \cdot Rel_zen^3 + d \cdot PS_zen \quad (5.5)$$

with a, b, c, and d being the regression coefficients. The model was chosen for its high fit ($R^2$ = 0.81, RMSE = 0.07, MRE = 0% in Figure 5.8-a) and after the assessment of the absence of artefacts in the corrected images, and of the "flattening" of the spectral value across the image field. The spectral "flattening" was visually examined through spectral data extraction in transects, as shown in Figure 5.9 in a subset of two images per calibration set (2 x 12). The model was tested on the three validation datasets, providing the results summarized in Figure 5.8-b. The validation results showed that the model seems to provide stable and consistent ANIF predictions across the tested observation/illumination range ($0.81 < R^2 < 0.91$, $0.08 < RMSE < 0.1$) but with a dataset-dependent bias, showed by a noticeable positive or negative MRE (%) and evident in the observed vs predicted plot (Figure 5.8-b).

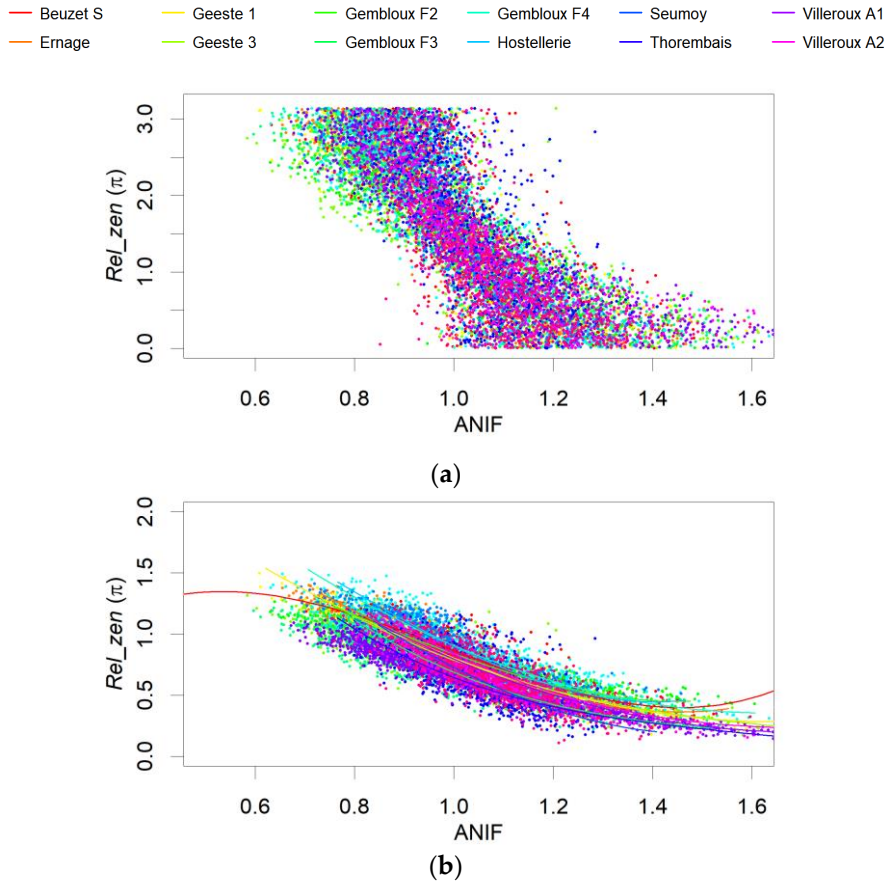


Figure 5.7. From a subsampling of the ensemble of the 12 calibration datasets: a) correlation plot of *Rel_az* (in radians) against the ANIF; b) correlation plot of *Rel_zen* (in radians) against the ANIF, with the 3$^{rd}$ order polynomial interpolation lines from the different datasets.

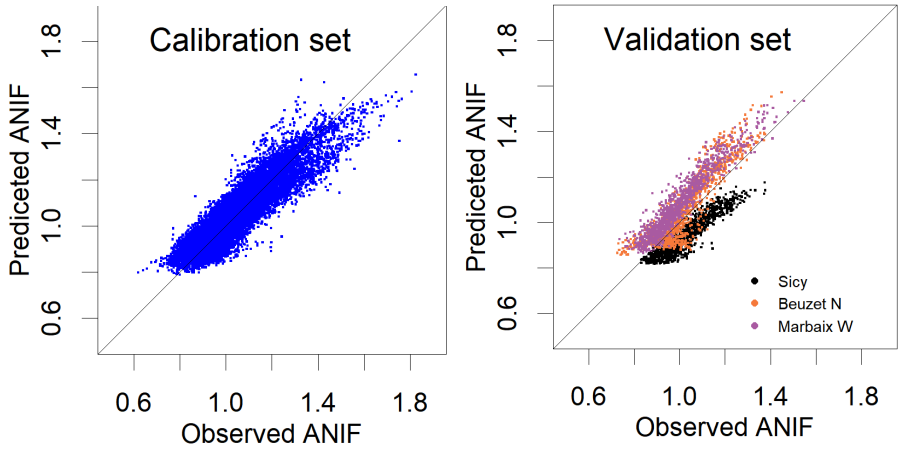


| | $R^2$ | RMSE | MRE % |
|---|---|---|---|
| Final model | 0.81 | 0.07 | 0 |

(**a**)

| | $R^2$ | RMSE | MRE % |
|---|---|---|---|
| Sicy | 0.85 | 0.1 | 8.6 |
| Beuzet N | 0.81 | 0.08 | -3.7 |
| Marbaix W | 0.91 | 0.09 | -8.1 |

(**b**)

Figure 5.8. Observed vs predicted plot of the ANIF from the modelling of the calibration (a) and validation (b) datasets. $R^2$, RMSE and MRE % are indicated below each respective plot.

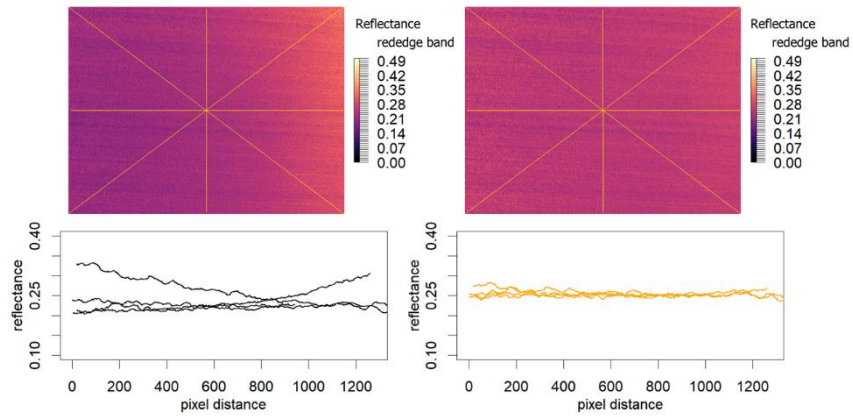


Figure 5.9. Example of reflectance picture (rededge band) before (left) and after (right) ANIF correction. The yellow lines represent the transect from which spectral data were extracted to check the result of spectral normalization. The data extracted from the transects are plotted under the respective images, in black for the original image and in orange for the corrected one.

### 5.3.3 Correction evaluation results

Step (i) of our analysis showed that, on average, the measurement of the same pixel location from different images was more spectrally stable after the proposed ANIF correction. In the calibration dataset, the standard deviation of measured sample pixel reflectance from the corrected images (mean = 0.023) was indeed lower ($t[429] = 6.03$, $p << 0.05$) than in the original images (mean = 0.032). This is also supported by a comparison of the density plots before and after correction (Figure 5.10). A comparable result was also obtained with the validation dataset (density plots in Figure 5.10), were the *sd* of reflectance in the corrected images (mean = 0.030), was significantly lower ($t[172] = 3.58$, $p < 0.05$) than with the original images (mean = 0.037). The reflectance stability on the validation set was generally lower (corrected images obtained the same mean and *sd* density distribution as the original images in the calibration dataset) but the starting conditions were also worse (starting from a *sd* of 0.037).

Regarding the evaluation step (ii), the average *SSin* index calculated for the 9 selected sets (Figure 5.12) decreased for all cases except one ("Sicy") showing that with the proposed correction the sinuosity is generally reduced by a minimum of 0.63% to a maximum of 5.97%. A visual *SSin* reference example can be found in Figure 5.11, where the original and corrected transect provided *SSin* values of 1.030 and 1.022, respectively, with a decrease in sinuosity of 0.77%. Without a clear reference sinuosity index to discriminate between a map affected by stripes and a corrected map, apart from a visual interpretation, an analysis of the spectral data in relation to the drone flight lines was carried out to support the positive effects of our correction methodology. The correlation between the magnitude of the spectral peaks and valleys on the transect and the distance to the closest flight line (sensor position) is added in Figure 5.13 for the 9 selected datasets. Generally, a higher correlation (both positive and negative) is observed in the original maps, where the peaks and/or valleys of the stripes seem to be either very close (as per example in Figure 5.11) or very far to the flight lines. On the other hand, a weaker or zero correlation is generally observed on the corrected maps. The position of the sensor in presence of stripes did not show a consistent behaviour: in some cases, both peaks and valleys were associated with high proximity to flight lines, resulting in an overall negative correlation; in other cases, only peaks or only valleys were close to flight lines, resulting in either a positive or negative correlation depending on the

local transect linear interpolation. In general, a lower correlation associated with the corrected orthomosaics indicated that the striping effect was effectively eliminated in most cases and at least reduced in some others. As a visual example of the difference between original and corrected spectral orthomosaic (e.g., rededge band) and of the elimination of the "striping" effect, the orthomosaic product of the "Hostellerie" dataset is reported in Figure 5.14. For the visual result of all the other datasets, refer to Appendix C (Figure C 1-13).

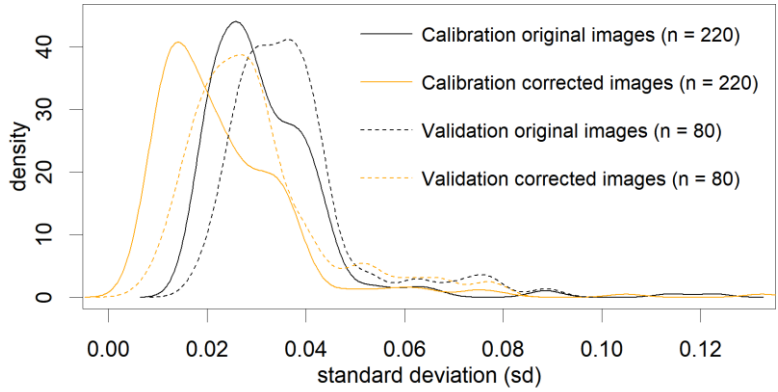


Figure 5.10**.** Results of step (i) analysis: density distribution for a calibration sample size n = 220 and validation sample size n = 80 of the standard deviation *sd* of reflectance for same pixel observation by different camera positions/angles (9-20 different camera observation per pixel), before and after ANIF correction (black and orange lines respectively).

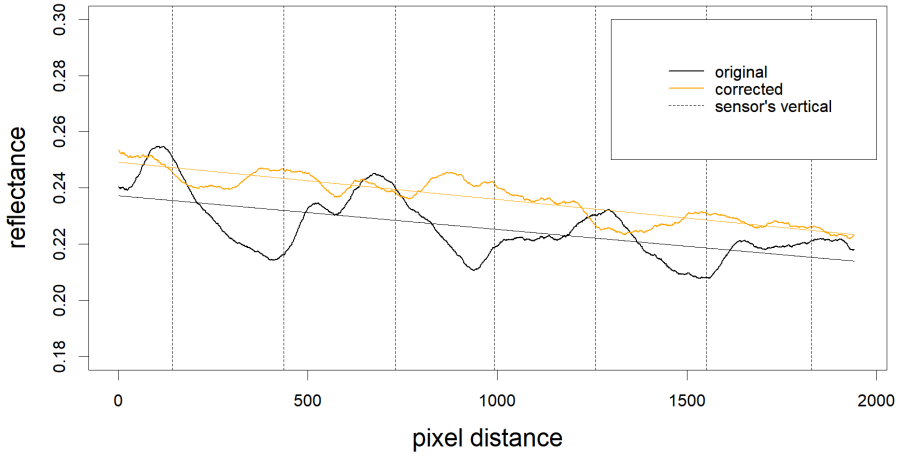


Figure 5.11**.** Results of step (ii): example of transect spectral data evaluation (Hostellerie dataset), before and after image correction (black and orange,

respectively), and the corresponding linear interpolation. The position of flight lines (sensor vertical position) is added as black dashed lines. The *SSin* calculated for the original transect was 1.030 while that for the corrected transect 1.022.

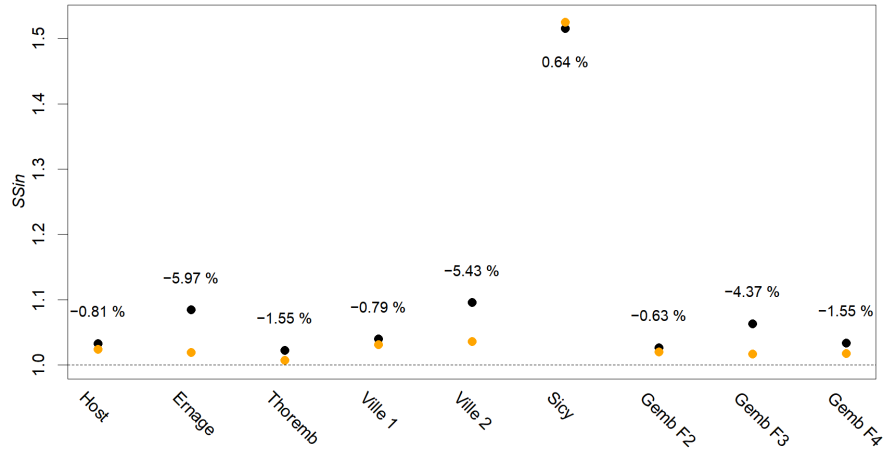


Figure 5.12**.** Results of step (ii): average spectral Sinuosity index *SSin* for each field. Black = original orthomosaics, orange = corrected orthomosaics. The % difference between *SSin* of corrected and original reflectance transects is indicated above each point.

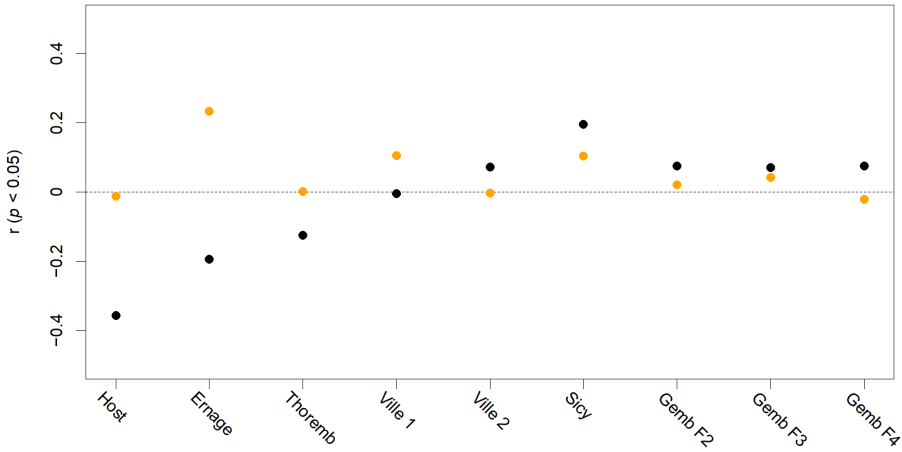


Figure 5.13**.** Results of step (ii): correlation between striping magnitude and distance to the vertical of the closest flight line/sensor position, measured across spectral transects.

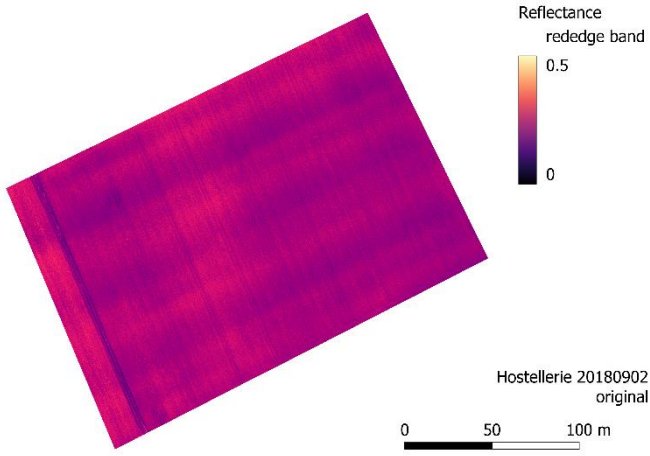


(**a**)

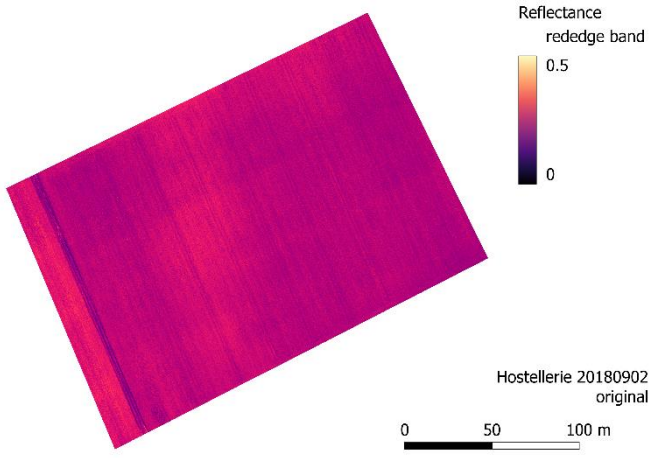


(**b**)

Figure 5.14**.** Example of original (a) and ANIF-corrected (b) final spectral orthomosaic (rededge band example) for the flight Hostellerie 02/09/2018.

## 5.4 Discussion

Results of analysis step (i) showed that the stability of the spectral measurement of the same pixel location across different images sensibly improved after the application of the ANIF correction. The relative improvement in *sd* (Figure 5.10) resulted almost the same for the calibration and validation datasets, although overall spectral stability was lower in the validation dataset. This is probably due to the non-optimal terrain conditions that prevented the initial choice of the three validation datasets for

calibration purposes. Contrary to the calibration dataset, the fields used for the validation data were indeed characterized by non-homogeneous soil colours, soil crusting (accumulation on the surface of finer particles with high reflectance), vegetation residue and varying slope/aspect. In this regard, the effects of soil colour and vegetation residuals could probably be encompassed by a richer calibration sampling. On the other hand, surface slope and aspect have a much more important role on illumination geometry, which are generally tackled with topographic correction methods (Richter, Kellenberger and Kaufmann, 2009; Jakob, Zimmermann and Gloaguen, 2017), but their effect on soil anisotropy has not been accounted for in the context of this research. The specific ANIF model equation of this study was developed using only relative observation/illumination angles, which are slope/aspect-invariant and only dependent on sensor and sun orientation. This represents a limitation and calls for further development of the proposed model. Moreover, surface roughness and the partial or total loss of radiometric signature caused by its shadows represent another issue in need of further scrutiny (Croft, Anderson and Kuhn, 2014; Alessia Movia, Beinat and Crosilla, 2016; Crucil and Van Oost, 2021).

The two correction evaluation indicators adopted in step (ii) seem to show that, in general, the specific "striping" artefact affecting the orthomosaics of the available dataset has been greatly reduced or eliminated following the proposed correction methodology. Some uncertainties arise, e.g., in the observation of *SSin* analysis results (Figure 5.13) with the anomaly of higher *SSin* values for the "Sicy" dataset, as compared to the other fields. For that specific case it must be noted that the dataset was not used in model calibration as its images were not sufficiently homogeneous due to the prominent presence of tractor tracks in most images. Therefore, the interpretation of step (ii) indexes, remain closely confined to this specific case study, as no other studies were found to tackle this specific problem, and no proper comparison with other indicators could be made. Moreover, they do not represent completely objective evaluations on the correctness of the analysed spectral orthomosaics, as no independent data with reference methods were available.

## 5.5 Conclusions

This study provided an empirical correction methodology for UAS-based multispectral imaging datasets of bare soils to account for the effects of the BRDF, based on the application of an Anisotropy Factor (ANIF) correction.

The dataset of images available for this study was sufficient to calibrate a simple model relating the ANIF to a wide range of sensor-pixel-illumination conditions by using only two angles: relative sensor-pixel-sun zenith and relative sensor-pixel-sun azimuth. The proposed correction has been tested on 15 available datasets. As a result, the employment of ANIF-corrected images for multispectral orthomosaic generation with a photogrammetric software provided spectral maps free of anisotropic related artefacts in most cases, as assessed by several ad-hoc indexes. The validation on an independent image dataset, however, showed the presence of some systematic error, the causes of which require further investigation. Plausible future directions for model enhancement would be the implementation of a topographic index to account for the effects of slope and aspect, the consideration of soil roughness and its related shadows, and/or an enrichment of model calibration with different soil conditions (vegetation residue, humidity, crusting).

# Chapter 6

# General conclusions

## 6.1 Main findings

Modelling soil erosion is hampered by the complexity intrinsic to the short-term variability and dynamics between its physical properties, especially on the soil surface layer. Accurate and spatially distributed data, particularly at fine scale, are increasing in demand by the scientific community to tackle this issue. Remote sensing with multispectral imaging could partly meet this demand, but another series of issues related to the complexity of the signal to be detected must be solved to provide qualitative data on specific target soil variables. The work of this thesis focused on the detection capability of the development dynamics of soil physical crust. The general objective was to understand whether soil physical crust development could be detected and modelled by means of low altitude, UAS-based, multispectral remote sensing, with a case study on loamy soils of the Belgian loess belt. Four specific objectives were strategically ordered in pursue of the general one: these objectives have been structured on an ideological pathway to test a set of sensors and their detection capability for soil properties, starting from laboratory analysis and progressively scaling to the remote sensing domain. After a general introduction, Chapters 2 to 5 of this thesis were dedicated each to one of these objectives.

In Chapter 2, a set of UAS-compatible hyperspectral sensors and multi-spectral cameras operating in the vis-NIR spectral range were tested for their ability to provide data with a sufficient quality for developing soil organic carbon (SOC) prediction with multivariate spectral models in outdoor conditions, in a proximal sensing setup. The sensor capabilities were compared with those provided by laboratory standard measurements coming from an ASD Fieldspec 3 hyperspectral sensor. SOC modelling prediction based on the narrow bands of two multispectral cameras (Parrot Sequoia and Tetracam Mini-MCA6) provided better performances than those obtained with a portable hyperspectral sensor (OceanOptics STS). Furthermore, the model built on the Sequoia camera reached the same performance (RMSE = 2.7 $g \cdot kg^{-1}$, RPD = 4.2) as the reference ASD measurements in outdoor conditions (RMSE = 2.6 $g \cdot kg^{-1}$, RPD = 4.2). Variable importance analysis of the spectral models showed that: i) the spectral

region between 500 and 600 nm contains most information for hyperspectral SOC modelling, and ii) the vis-NIR range up to about 900nm is exploited when using multispectral narrow bands. Validation results indicated that the vis-NIR range alone may be sufficient for SOC prediction, at least for the conditions encountered in this study. Moreover, it was demonstrated that it is possible to exploit predictive models calibrated with hyperspectral laboratory data on outdoor spectra obtained by the same portable instruments, applying a correction factor based on an internal soil standard. It was concluded that the implementation of small-form vis-NIR portable sensors in UAS systems could be a viable strategy to improve the effectiveness of SOC assessments at a much higher spatial and temporal resolution than existing methodologies. More importantly, this work offered a proof of concept for the instrumental and methodological basis to start the study of soil crust development.

Chapter 3 explicitly started to address soil physical crust modelling. Its objective was to analyse the functional relationships between soil crusting and soil surface reflectance as derived from multispectral imaging and how this can be inferred from proximal sensing and from (simulated) low-altitude UAS sensing. More specifically, the aim was disentangling the effects of soil surface roughness from those of crust development on spectral reflectance factors, by establishing and evaluating a dedicated data pre-processing protocol. To do so, indoor and outdoor experiments were carried out on soil samples to monitor the evolution of soil crust and micro-scale soil roughness in response to cumulative rainfall kinetic energy. After successfully testing a method to eliminate shadows from multispectral images, the residual light scattering effect related to soil surface irregularities (i.e., roughness) in the multispectral spatial domain were assigned to the i*qr* of the reflectance values in a kernel. A high-resolution digital terrain model provided a map to exclude areas where roughness was present (i.e., DR sub-setting). When working at high image resolution (proximal sensing setup, 2 mm/pixel) it resulted that the *iqr* of all multispectral bands was significantly related to soil roughness ($0.21 < r < 0.36$, $p < 0.05$). PLSR models were then developed based on vis-NIR data to predict the cumulative kinetic energy received by soil samples, as a proxy for soil crust development. These models suggested that an input based on multispectral reflectance + *iqr* data with DR pre-treatment provides the best combination of high predictive performance ($R^2 = 0.44$) and high discrimination between kinetic energy and roughness. Hyperspectral data were shown to contain information to model the effect of kinetic energy

on soil crusting from small, specific features and this with a high model performance ($R^2$ = 0.97). When analysing images at the 15 mm image resolution (low altitude flight setup), the same conclusions could not be made, as no clear discrimination between roughness and crust could be made, model wise. It was concluded that it is possible to model vis-NIR image data of bare soil into amounts of rainfall kinetic energy received by a soil sample, as a proxy for crust development, but roughness effects on spectral features should be eliminated before modelling.

Chapter 4 directly capitalized on the findings of Chapter 3, adopting its instrumental and methodological basis to apply them in real field conditions, from real UAS-surveys. To do so, a series of 2x1 m plots were monitored during a three-month period under natural rainfall. The experiment showed that the five vis-NIR spectral broad-bands used in the previous experiments were sufficient to predict ($R^2$ = 0.79) a series of KE levels by simply removing shadows and normalizing the spectra through a SNV transformation. A close-proximity vis-NIR-SWIR hyperspectral analysis of the same soil surfaces further supported the results. On the downside, a complementary collection of soil eroded and exported from the plots did not show a significant correlation between increased soil crust development and sediment export. Due to the experiment design, it was also not possible to measure with accuracy the amount of runoff and associate its increase to crust development. It was concluded that larger plots, and a longer measurement period would be desirable to attempt the association of a spectral-based soil crust model to changes in infiltration rates and sediment generation.

An optimal prosecution of the work of the previous chapters would have been testing the assessment of physical crust development at field or small basin scale, taking advantage of the full potential of UAS surveys. Nevertheless, several data collection campaigns carried out at the same time or after the work of the previous chapters highlighted the problems of primary importance caused by the anisotropic properties of natural surfaces when measuring radiation for analytical purposes. Preliminary analysis from our own bare soil multispectral datasets from low flight UAS showed indeed that the resulting orthomosaics exhibited prominent spectral aberrances in the form of “stripes” of different reflectance intensity, parallel and coinciding with the drone flight lines. Consequently, it was deemed necessary to solve this problem before attempting any wide-scale assessment of soil properties. Chapter 5, in this regard, sets aside the study of soil crust to prioritize the provision of an empirical correction methodology for UAS-based

multispectral imaging datasets of bare soils to account for the effects of the bidirectional reflectance distribution function (BRDF), based on the application of an Anisotropy Factor (ANIF) correction. The dataset of images available for this study was sufficient to elaborate and calibrate a simple model relating the ANIF to a wide range of sensor-pixel-illumination conditions and correct for the effects of the BRDF. As a result, the employment of ANIF-corrected images for multispectral orthomosaic generation with a photogrammetric software provided spectral maps free of anisotropic related artefacts in most cases, as assessed by several ad-hoc indexes. The validation on an independent image dataset, however, showed the presence of some systematic error, the causes of which require further investigation.

In summary, after a preliminary assessment of spectral sensor technology and analytical methods in Chapter 2, Chapter 3 proposed an innovative methodology to model a component of soil physical crust development, defined by the spectral changes caused on the soil surface by cumulative amounts of rainfall kinetic energy. This was achieved by developing a data processing protocol for multispectral imaging in the vis-NIR range. By validating the results of Chapter 3 in real field conditions, Chapter 4 offered some evidence that it is possible to map the development of soil physical crust with a remote sensing application, able to overcome the uncertainties of “expert based” classifications. Chapter 5, finally, tackled a critical issue with the negative effects of soil anisotropy on multispectral imaging, proposing a semi-empirical correction methodology with good preliminary results, and easing the way for wide scale UAS-based assessment of soil properties with multispectral imaging.

## 6.2 Potential, limitations, and future perspectives

This thesis presented a data treatment and modelling protocol that, combined with the recent advancements in technology and availability of remote sensing tools like UASs, can provide useful answers to the increasing demand of quantitative and spatially distributed data for soil science, soil erosion modelling, and policy decision making. Despite not offering new meaningful insights on the effect of crust development on runoff and sediment generation at the plot level, these results nevertheless provided a preliminary step to characterize soil crust at wider scale. This step was deemed necessary before further studies can address soil crust dynamic

relationships with other soil variables like roughness, crops and vegetation residue, soil organic carbon, and its general contribution in soil erosion.
Regarding the potential in remote sensing development, UAS surveys and the results of this work could represent a solution to cover the gap between proximal sensing and aerial/satellite sensor, either by providing validation data at the needed spatial and temporal resolutions (Mulder *et al.*, 2011), or by expanding the availability for data fusion approaches (Ghamisi *et al.*, 2019). Indeed, as discussed in Section 1.1.6, current satellite sensors have a spatial resolution (e.g., 10-20 m for Sentinel-2) that may not be sufficient for the fine-scale variability that characterizes some soil variables, and fixed revisit may easily miss optimal soil conditions. Aerial data instead, while offering higher data resolution (2-5 m), have relatively high or prohibitive operative costs. A recent example for the case of soil organic carbon can be found in (Biney *et al.*, 2021). With the increasing interest and accessibility to UAS capabilities and open-source software solutions, also in the so called "tech-savvy" general public, adaptation of this work could easily find a place in precision agriculture applications.
Among the limitations of the presented approached, must be remembered that multivariate regression models, such as the PLSR technique adopted in this work, are an empirical approach that may need a relatively large number of calibration samples to achieve satisfying prediction results. This is due to the fact that reflectance spectra of soils are largely nonspecific due to the overlapping absorption of soil constituents and to the scattering effects caused by soil structure, which complicates mathematical feature extraction (refer to Section 1.1.5). Field conditions are then heavily complicating soil spectral response with other sources of uncertainty. In Chapter 3 a discrimination of the spectral response of crust and roughness was attempted, but future research should certainly repeat the process for other confounding variables, like soil moisture, vegetation (especially vegetation residue, for which an example is provided in Dvorakova *et al.*, 2020), and soil organic carbon (like discussed in Chapter 4.3.1). This is specifically true when adopting point-measurement spectrometers, whose measurement is the result of an integration over a certain area. The nature of spectral imaging, on the other side, offers the possibility to selectively discard unwanted features/pixels, like with the shadow elimination or the roughness masking approach used in Chapters 3 and 4 of this thesis. However, important questions on spectral unmixing would rise again when sacrificing pixel spatial resolution for image spatial coverage, in higher altitude flights.

Must also be taken into consideration that soil crust models of this thesis have been calibrated from samples of the same soil type, with negligible differences in soil organic carbon. For the same reasons stated in a previous paragraph, local multivariate calibrations with spectral data are not suitable for a direct application in different soil substrates, as a peculiar spectral signature is derived from the specificity of the associated soil composition. Understanding the physical meaning of crust spectral changes, intrinsic to each specific soil texture, aggregate state, particle rearrangement, should be a priority before generalizing any result. As advocated in Chapter 4.3.1, an ideal prosecution of this work would carry a specific physico-chemical investigation of soil crust to complement the spectra data. Another possible approach to address this issue could be the enrichment of an existing local spectral model by working on a more diverse selection of samples (i.e., spiking). That is the main reason for the interest dedicated in the creation of national, continental, and even global spectral libraries, as discusses in Section 1.1.5. An approach involving a small regional spectral library for SOC estimation with UAS-based hyperspectral data has already been successfully attempted (Zhang *et al.*, 2021).

Soil moisture represent another challenge for future investigations, as it is a fast-changing soil property with a strong influence on the spectral signal of soils. It affects the visible portion of the spectrum with albedo changes and the NIR-SWIR portion with substantial noise in the absorption bands of water vapour (see Chapter 2.2.4). Understanding and analytically quantifying its effect on the spectral detection of other soil properties is of primary importance for soil remote sensing (Babaeian *et al.*, 2019). Recently, proximal sensing (Lambot *et al.*, 2006) and UAS-based (Wu *et al.*, 2019) applications of Ground Penetrating Radar technology have been developed to measure soil water content of the first few cm of soil. Given the open research questions just outlined, it would be desirable to take advantage of these approaches to further advance the research initiated in this thesis

Another series of drawbacks are related to UAS technology and survey planning. On one side, an important limitation in current UAS surveys is dictated by battery duration. While the advancements in firmware and software solutions, engines efficiency and payload reduction (through sensor miniaturization) reached a mature stage, huge improvements are still needed to extend flying time. Within the purposes of this study, and depending on altitude, on flight speed and on the needed data resolution, single multi-rotor UAS flights were able to cover 4-6 ha of terrain. Flight time

and coverage could be extended with the adoption of fixed wing UAS solutions, but new operative considerations must be made (e.g., piloting license, availability of the aerial space, data acquisition rate). On the other side, meteorological conditions are limiting the timeframes for baseline quality of spectral data. All of the spectral surveys carried out for this thesis were executed in optimal conditions, i.e., within 2-3h from solar noon and with clear sky, to avoid the light aberrations caused by moving clouds. With these assumptions made, reaching the basin-scale coverage needed to study the effects of land use, agricultural practices and connectivity on soil erosion may still be a lengthy approach.

Finally, regarding Chapter 5 and its BRDF correction model, must be remembered that the validation attempts on an independent image dataset, despite providing orthomosaics free of aberrations, showed some bias in ANIF prediction, the causes of which may reside in environmental parameters not accounted before. Plausible future directions for model enhancement would be the implementation of a topographic index to account for the effects of slope and aspect, the consideration of soil roughness and its related shadows, and/or an enrichment of model calibration with different soil conditions (vegetation residue, humidity, crusting).

# Appendix A

## SOC modelling results

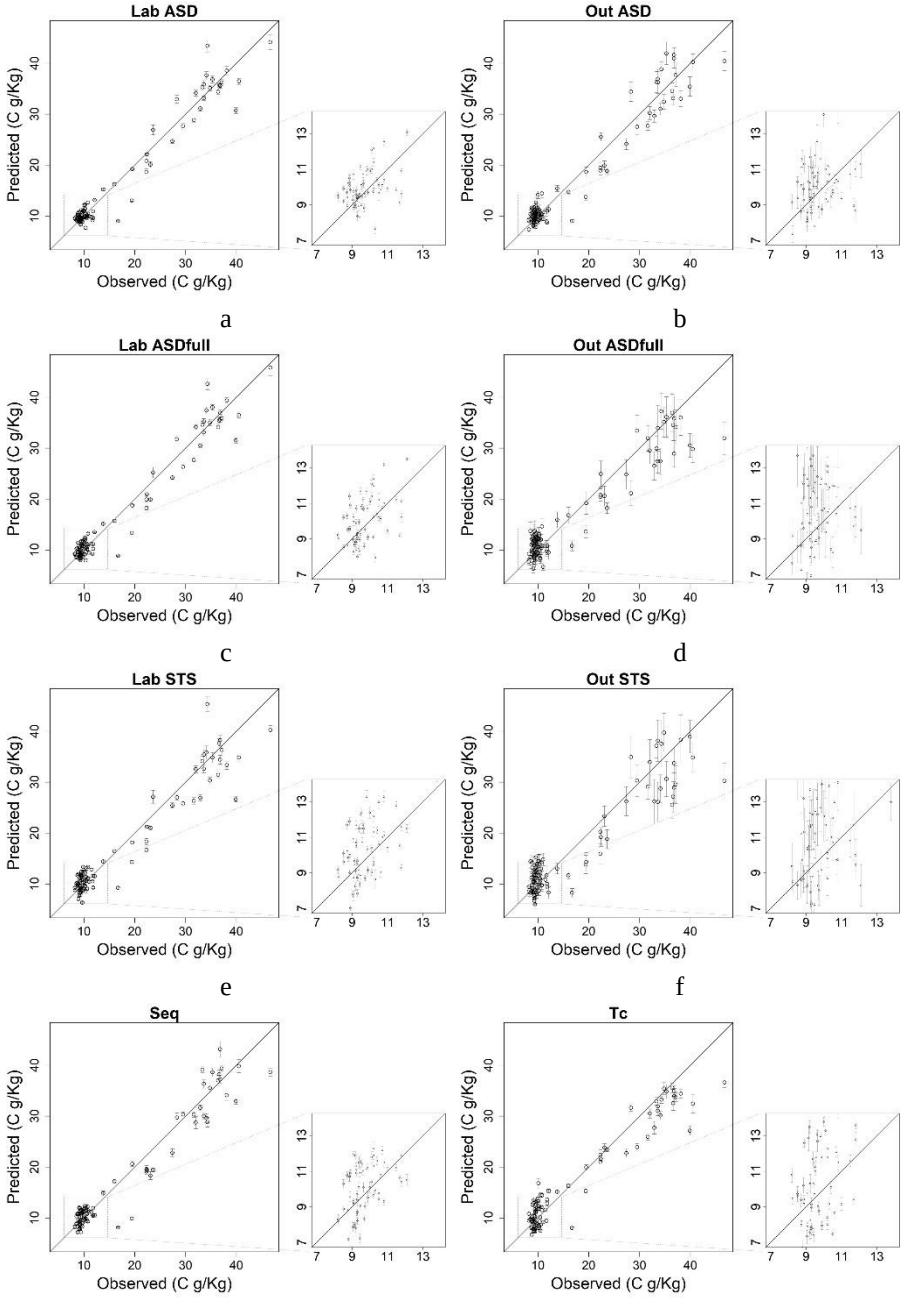

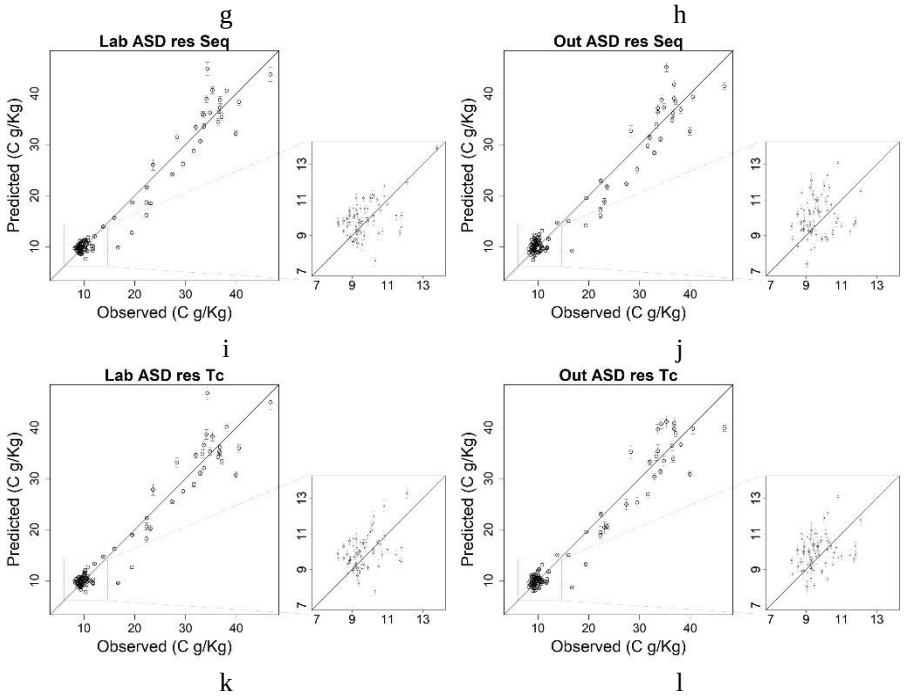


Figure A 1. Plots of observed versus predicted SOC values from the models used in the comparison of the measuring setups. Vertical error bars represent the standard deviation obtained from the validation process through 100x random selection.

# Appendix B

## Shadow Removal

A calibration dataset was first created by manually selecting 30 illuminated and 30 shadowed pixels per image on two RGB composite images from two soilboxes (total of 60 and 60 pixels respectively). The difference in reflectance between illuminated and shadowed pixels was evident in all the five spectral bands (Figure B 1-a), so the brightness index was calculated as Equation (B1):

$$I = \frac{Blue + Green + Red + Rededge + NIR}{5} \quad \text{(B1)}$$

A threshold for automatic unsupervised shadow detection was then individuated by:

1. sorting all pixel I values pertaining to a soilbox;
2. applying a detrend function to enhance local peaks by fitting a second order linear model and returning the fitted residuals (Figure B 1-b);
3. searching for the first local maximum (vertical grey line Figure B 1-b).

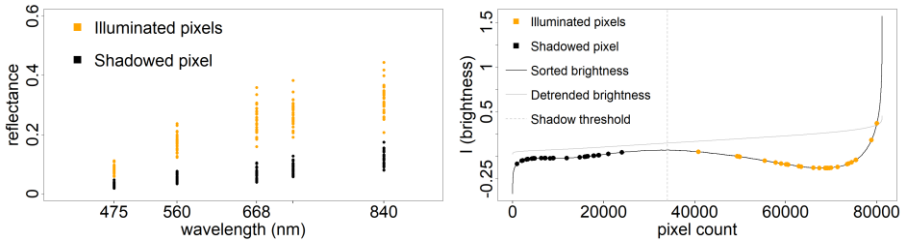


Figure B 1. Example of the procedure for shadow threshold individuation on a soil multispectral image: difference in reflectance between illuminated and shadowed calibration pixel (a) and the brightness curves after sorting and detrending to make the shadow threshold stand out as a local maximum (b).

The threshold was calculated for each single image, and then applied for pixel selection. The quality of the output was visually evaluated in a side-by-side comparison between the original and the de-shadowed image (Figure B 2).

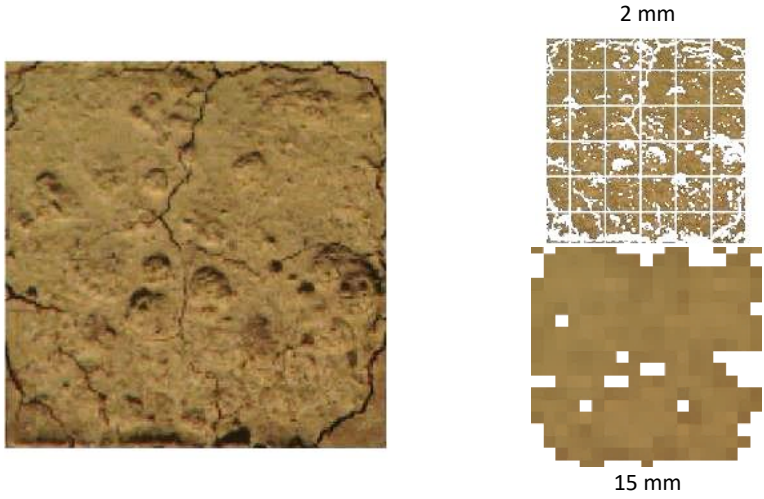


Figure B 2. Example of soilbox image (false colour RGB composite) before de-shadowing (left), and after de-shadowing at 2 mm resolution (top right) and 15 mm resolution (bottom right).

For all soil samples, the percentage amount of pixel removed for the same soil sample between the 2 mm and the 15 mm resolution was compared (Figure B 3 - left). The relative percentage difference between the removal amount in the two resolutions (Figure B 3 - right) showed that the majority of samples got almost the same amount of pixels removed (between the −20% and + 20% difference).

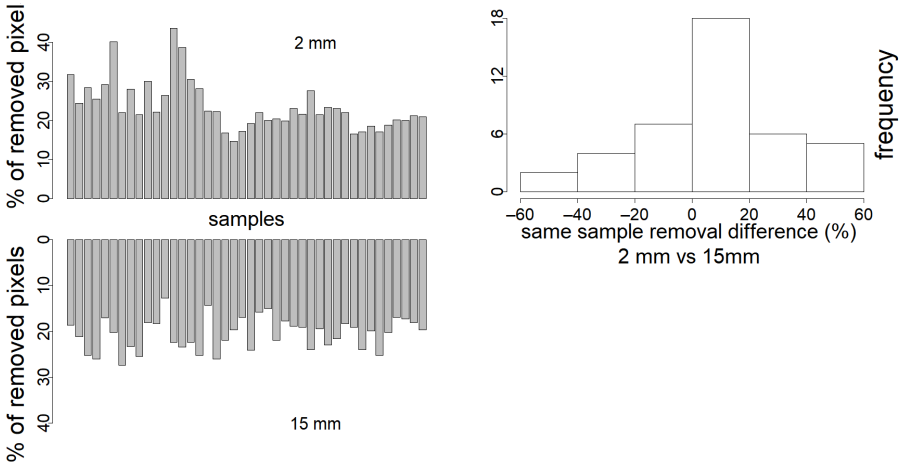


Figure B 3. Statistics on the percentage of pixel removal due to shadow across the full dataset: percentage of pixel removal across the samples at 2 mm resolution (top left); percentage of pixel removal across the samples at 15 mm resolution (bottom left); relative percentage difference in pixel removal between same samples at different resolutions (right).

# Appendix C

## ANIF correction results on spectral orthomosaics

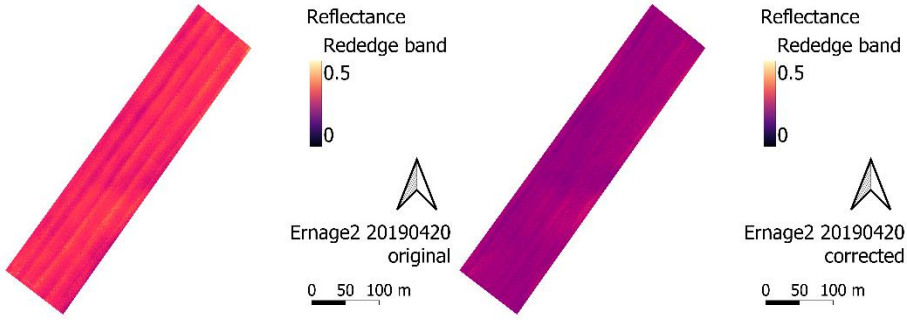


Figure C 1. Original (left) and ANIF-corrected (right) final reflectance orthomosaic (rededge band example) for the flight Ernage 20190420.

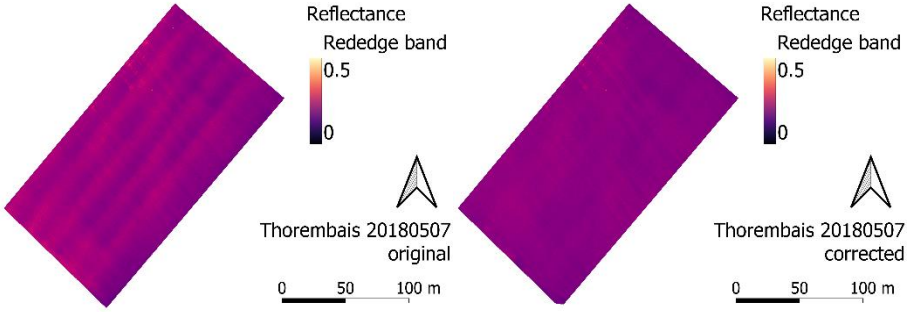


Figure C 2. Original (left) and ANIF-corrected (right) final reflectance orthomosaic (rededge band example) for the flight Thorembais 20180507.

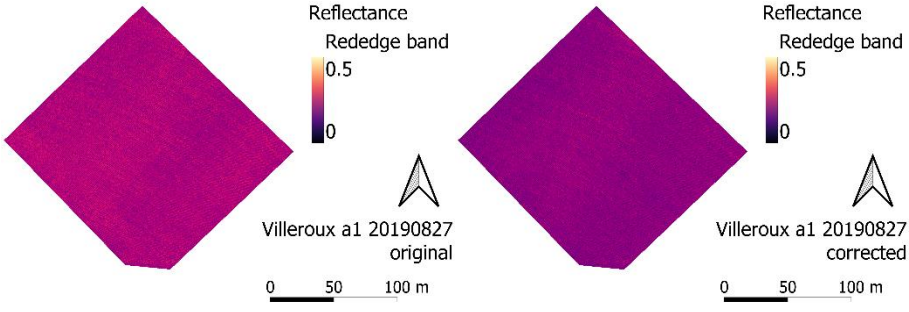


Figure C 3. Original (left) and ANIF-corrected (right) final reflectance orthomosaic (rededge band example) for the flight Villeroux a1 20190827.

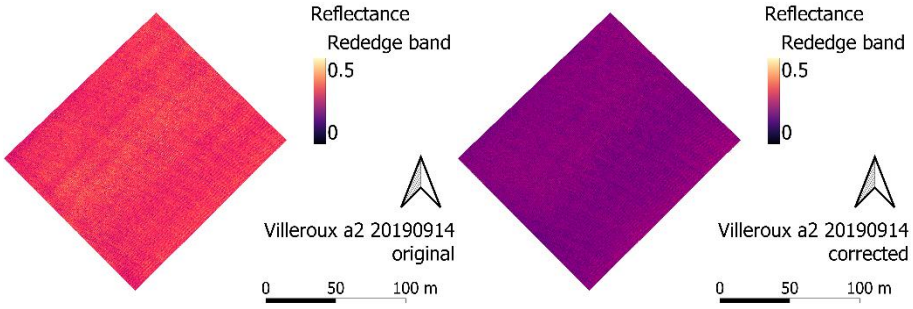


Figure C 4. Original (left) and ANIF-corrected (right) final reflectance orthomosaic (rededge band example) for the flight Villeroux a2 20190914.

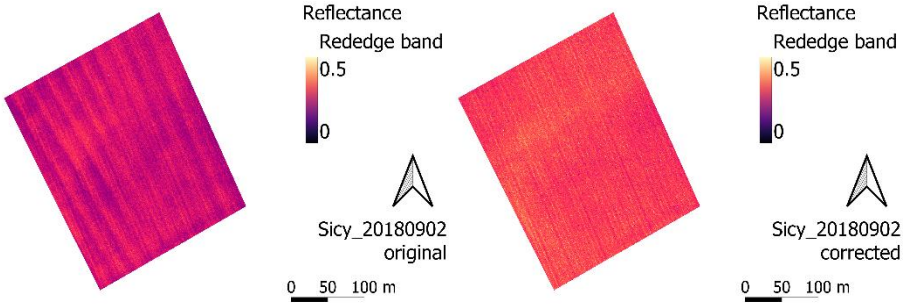


Figure C 5. Original (left) and ANIF-corrected (right) final reflectance orthomosaic (rededge band example) for the flight Sicy 20180902.

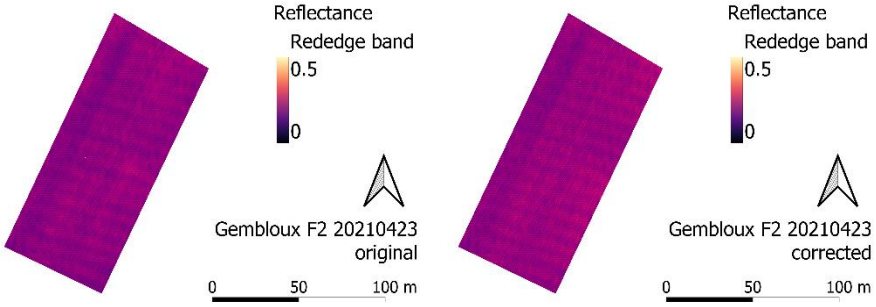


Figure C 6. Original (left) and ANIF-corrected (right) final reflectance orthomosaic (rededge band example) for the flight Gembloux F2 20210423.

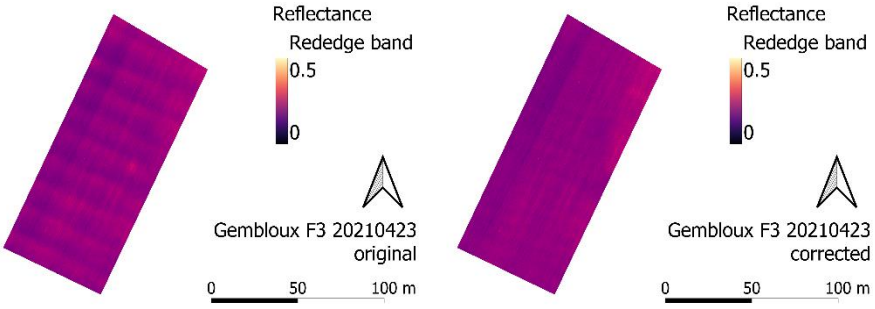


Figure C 7. Original (left) and ANIF-corrected (right) final reflectance orthomosaic (rededge band example) for the flight Gembloux F3 20210423.

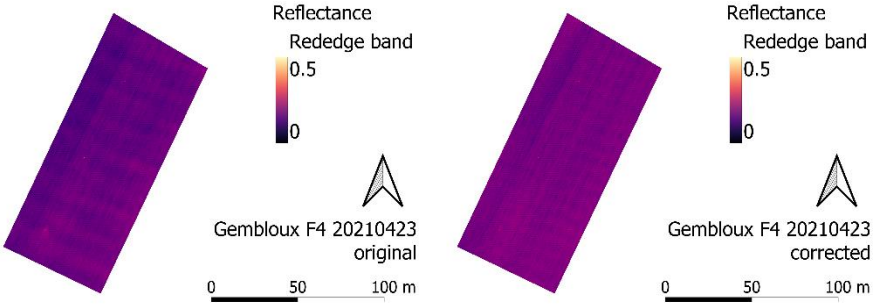


Figure C 8. Original (left) and ANIF-corrected (right) final reflectance orthomosaic (rededge band example) for the flight Gembloux F4 20210423.

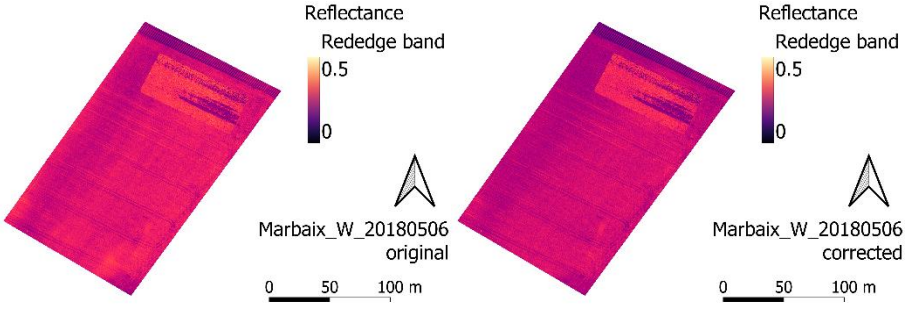


Figure C 9. Original (left) and ANIF-corrected (right) final reflectance orthomosaic (rededge band example) for the flight Marbaix 20180506.

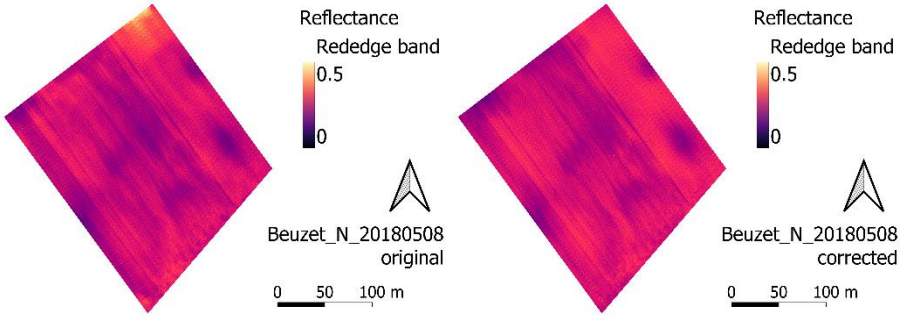


Figure C 10. Original (left) and ANIF-corrected (right) final reflectance orthomosaic (rededge band example) for the flight Beuzet N 20180508.

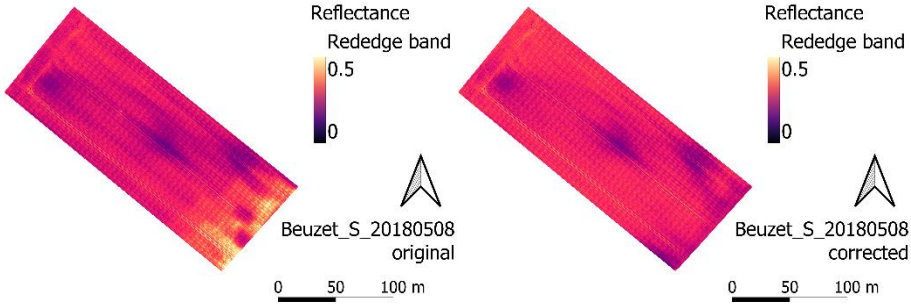


Figure C 11. Original (left) and ANIF-corrected (right) final reflectance orthomosaic (rededge band example) for the flight Beuzet S 20180508.

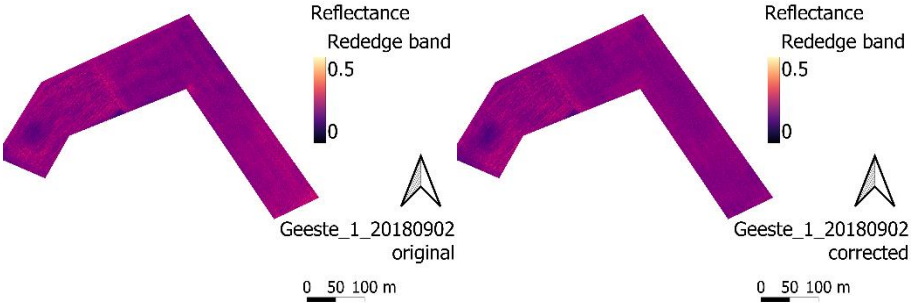


Figure C 12. Original (left) and ANIF-corrected (right) final reflectance orthomosaic (rededge band example) for the flight Geeste 1 20180902.

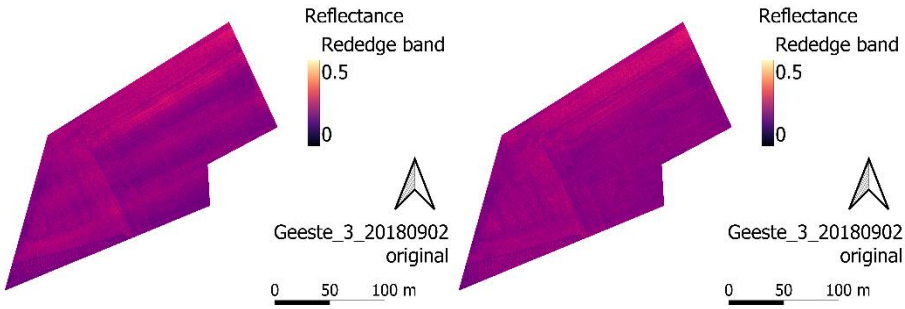


Figure C 13. Original (left) and ANIF-corrected (right) final reflectance orthomosaic (rededge band example) for the flight Geeste 3 20180902.

# References


Aasen, H. *et al.* (2018) 'Quantitative remote sensing at ultra-high resolution with UAV spectroscopy: A review of sensor technology, measurement procedures, and data correctionworkflows', *Remote Sensing*, 10(7), pp. 1–42. doi: 10.3390/rs10071091.

Aasen, H. and Bolten, A. (2018) 'Multi-temporal high-resolution imaging spectroscopy with hyperspectral 2D imagers–From theory to application', *Remote sensing of environment*. Elsevier, 205, pp. 374–389.

Aldana-Jague, E. *et al.* (2016) 'UAS-based soil carbon mapping using VIS-NIR (480-1000 nm) multi-spectral imaging: Potential and limitations', *Geoderma*. Elsevier B.V., 275, pp. 55–66. doi: 10.1016/j.geoderma.2016.04.012.

Anderson, K. and Croft, H. (2009) 'Remote sensing of soil surface properties', *Progress in Physical Geography*, 33(4), pp. 457–473. doi: 10.1177/0309133309346644.

Angelopoulou, T. *et al.* (2019) 'Remote sensing techniques for soil organic carbon estimation: A review', *Remote Sensing*, 11(6), pp. 1–18. doi: 10.3390/rs11060676.

Antoine, M., Javaux, M. and Bielders, C. (2009) 'What indicators can capture runoff-relevant connectivity properties of the micro-topography at the plot scale?', *Advances in Water Resources*. Elsevier Ltd, 32(8), pp. 1297–1310. doi: 10.1016/j.advwatres.2009.05.006.

Auerswald, K. *et al.* (2014) 'Use and misuse of the K factor equation in soil erosion modeling: An alternative equation for determining USLE nomograph soil erodibility values', *Catena*. Elsevier B.V., 118, pp. 220–225. doi: 10.1016/j.catena.2014.01.008.

Auerswald, K. *et al.* (2015) 'Comment on "Rainfall erosivity in Europe" by Panagos et al. (Sci. Total Environ., 511, 801-814, 2015)', *Science of the Total Environment*. Elsevier B.V., 532, pp. 849–852. doi: 10.1016/j.scitotenv.2015.05.019.

B. A. King and D. L. Bjorneberg (2012) 'Transient Soil Surface Sealing and Infiltration Model for Bare Soil under Droplet Impact', *Transactions of the ASABE*, 55(3), pp. 937–945. doi: 10.13031/2013.41525.

Babaeian, E. *et al.* (2019) 'Ground, Proximal, and Satellite Remote Sensing of Soil Moisture', *Reviews of Geophysics*, 57(2), pp. 530–616. doi: 10.1029/2018RG000618.

Bagarello, V. and Ferro, V. (2004) 'Plot-scale measurement of soil erosion at the experimental area of Sparacia (southern Italy)', *Hydrological Processes*, 18(1), pp. 141–157. doi: 10.1002/hyp.1318.

Bartholomeus, H. M. *et al.* (2008) 'Spectral reflectance based indices for soil organic carbon quantification', *Geoderma*, 145(1–2), pp. 28–36. doi: 10.1016/j.geoderma.2008.01.010.

Beisl, U. (2001) *Correction of Bidirectional Effects in Imaging Spectrometer Data*, *Remote Sensing Series*.

Bellon-Maurel, V. *et al.* (2010) 'Critical review of chemometric indicators commonly used for assessing the quality of the prediction of soil attributes by NIR spectroscopy', *TrAC - Trends in Analytical Chemistry*. Elsevier Ltd, 29(9), pp. 1073–1081. doi: 10.1016/j.trac.2010.05.006.

Ben-Dor, E. *et al.* (2003) 'The Spectral Reflectance Properties of Soil Structural Crusts in the 1.2- to 2.5-µm Spectral Region', *Soil Science Society of America Journal*, 67(1), p. 289. doi: 10.2136/sssaj2003.0289.

Ben-Dor, E. *et al.* (2004) 'Monitoring infiltration rates in semiarid soils using airborne hyperspectral technology', *International Journal of Remote Sensing*, 25(13), pp. 2607–2624. doi: 10.1080/01431160310001642322.

Ben-Dor, E. *et al.* (2009) 'Using Imaging Spectroscopy to study soil properties', *Remote Sensing of Environment*. Elsevier Inc., 113(SUPPL. 1), pp. S38–S55. doi: 10.1016/j.rse.2008.09.019.

Ben-Dor, E. (2012) 'Soil spectral imaging: moving from proximal sensing to spatial quantitative domain', *ISPRS Annals of the Photogrammetry, Remote Sensing and Spatial Information Sciences*, 1(September), pp. 67–70. doi: 10.5194/isprsannals-I-7-67-2012.

Ben-Dor, E. and Demattê, J. A. M. (2015) 'Remote sensing of soil in the optical domains', *Land Resources Monitoring, Modeling, and Mapping with Remote Sensing*, pp. 733–787. doi: 10.1201/b19322.

Benoit Thieurmel and Elmarhraoui, A. (2019) 'suncalc: Compute Sun Position, Sunlight Phases, Moon Position and Lunar Phase. R package version 0.5.0.' Available at: https://cran.r-project.org/package=suncalc.

Biney, J. K. M. *et al.* (2021) 'Exploring the suitability of uas-based multispectral images for estimating soil organic carbon: Comparison with proximal soil sensing and spaceborne imagery', *Remote Sensing*, 13(2), pp. 1–19. doi: 10.3390/rs13020308.

Le Bissonnais, Y. (1996) 'Aggregate stability and assessment of soil crustability and erodibility: I. Theory and methodology', *European Journal of*

*Soil Science*, 47(4), pp. 425–437. doi: 10.1111/j.1365-2389.1996.tb01843.x.

Le Bissonnais, Y., Daroussin, J., *et al.* (2005) 'Pan-European soil crusting and erodibility assessment from the European Soil Geographical Database using pedotransfer rules', *Advances in Environmental Modelling and Monitoring*, 2(1), pp. 1–15.

Le Bissonnais, Y., Cerdan, O., *et al.* (2005) 'Variability of soil surface characteristics influencing runoff and interrill erosion', *Catena*, 62(2–3), pp. 111–124. doi: 10.1016/j.catena.2005.05.001.

Le Bissonnais, Y. and Singer, M. J. (1992) 'Crusting, runoff, and erosion response to soil water content and successive rainfalls', *Soil Science Society of America Bulletin*, 56(6), pp. 1898–1903. doi: 10.2136/sssaj1992.03615995005600060042x.

Bjørn-Helge, B.-H. and Wehrens, R. (2007) 'The pls Package Principal Component and Partial Least Squares Regression in R', *Journal of statistical software*, 18(2).

Boiffin, J. and Monnier, G. (1985) 'Infiltration rate as affected by soil surface crusting caused by rainfall', in *Symposium*. Flanders Research Centre for Soil Erosion and Soil Conservation.

Boix-Fayos, C. *et al.* (2006) 'Measuring soil erosion by field plots: Understanding the sources of variation', *Earth-Science Reviews*, 78(3–4), pp. 267–285. doi: 10.1016/j.earscirev.2006.05.005.

Borrelli, P. *et al.* (2021) 'Soil erosion modelling: A global review and statistical analysis', *Science of the Total Environment*, 780. doi: 10.1016/j.scitotenv.2021.146494.

Brennan, B. and Bandeen, W. R. (1970) 'Anisotropic Reflectance Characteristics of Natural Earth Surfaces', *Applied Optics*. OSA, 9(2), pp. 405–412. doi: 10.1364/AO.9.000405.

Bull, I. D. *et al.* (1998) 'Organic geochemical studies of soils from the Rothamsted Classical Experiments—II, soils from the Hoosfield Spring Barley Experiment treated with different quantities of manure', *Organic Geochemistry*. Elsevier, 28(1–2), pp. 11–26.

Campbell, J. B. and Wynne, R. H. (2011) *Introduction to remote sensing*. Guilford Press.

Cantreul, V. *et al.* (2018) 'How pixel size affects a sediment connectivity index in central Belgium', *Earth Surface Processes and Landforms*, 43(4), pp. 884–893. doi: 10.1002/esp.4295.

Cantreul, V. *et al.* (2020) 'Performance of the LandSoil expert-based model to map erosion and sedimentation: application to a cultivated catchment in central Belgium', *Earth Surface Processes and Landforms*, 45(6), pp. 1376–1391. doi: 10.1002/esp.4808.

Carmi, G. and Berliner, P. (2008) 'The effect of soil crust on the generation of runoff on small plots in an arid environment', *Catena*, 74(1), pp. 37–42. doi: 10.1016/j.catena.2008.02.002.

Casa, R. *et al.* (2013) 'Geophysical and Hyperspectral Data Fusion Techniques for In-Field Estimation of Soil Properties', *Vadose Zone Journal*, 12(4), p. vzj2012.0201-vzj2012.0201.

Castaldi, F. *et al.* (2014) 'Estimation of soil properties at the field scale from satellite data: A comparison between spatial and non-spatial techniques', *European Journal of Soil Science*, 65(6), pp. 842–851. doi: 10.1111/ejss.12202.

Castaldi, F. *et al.* (2016) 'Evaluation of the potential of the current and forthcoming multispectral and hyperspectral imagers to estimate soil texture and organic carbon', *Remote Sensing of Environment*. Elsevier Inc., 179, pp. 54–65. doi: 10.1016/j.rse.2016.03.025.

Castaldi, F. *et al.* (2018) 'Soil organic carbon estimation in croplands by hyperspectral remote APEX data using the LUCAS topsoil database', *Remote Sensing*, 10(2). doi: 10.3390/rs10020153.

Castaldi, F. *et al.* (2019) 'Evaluating the capability of the Sentinel 2 data for soil organic carbon prediction in croplands', *ISPRS Journal of Photogrammetry and Remote Sensing*. Elsevier, 147(October 2018), pp. 267–282. doi: 10.1016/j.isprsjprs.2018.11.026.

Cerdan, O. *et al.* (2002) 'Incorporating soil surface crusting processes in an expert-based runoff model: Sealing and transfer by runoff and erosion related to agricultural management', *Catena*, 46(2–3), pp. 189–205. doi: 10.1016/S0341-8162(01)00166-7.

Cerdan, O. *et al.* (2010) 'Rates and spatial variations of soil erosion in Europe: A study based on erosion plot data', *Geomorphology*. Elsevier B.V., 122(1–2), pp. 167–177. doi: 10.1016/j.geomorph.2010.06.011.

Chabrillat, S. *et al.* (2019) 'Imaging spectroscopy for soil mapping and monitoring', *Surveys in Geophysics*. Springer, 40(3), pp. 361–399.

Chamizo, S. *et al.* (2012) 'Discriminating soil crust type, development stage and degree of disturbance in semiarid environments from their spectral characteristics', *European Journal of Soil Science*, 63(1), pp. 42–53. doi:

10.1111/j.1365-2389.2011.01406.x.

Cheng, Q., Ma, W. and Cai, Q. (2008) 'The relative importance of soil crust and slope angle in runoff and soil loss: A case study in the hilly areas of the Loess Plateau, North China', *GeoJournal*, 71(2–3), pp. 117–125. doi: 10.1007/s10708-008-9149-5.

Chenu, C., Le Bissonnais, Y. and Arrouays, D. (2000) 'Organic Matter Influence on Clay Wettability and Soil Aggregate Stability', *Soil Science Society of America Journal*, 64(4), pp. 1479–1486. doi: 10.2136/sssaj2000.6441479x.

Chong, I.-G. and Jun, C.-H. (2005) 'Performance of some variable selection methods when multicollinearity is present', *Chemometrics and Intelligent Laboratory Systems*, 78(1–2), pp. 103–112. doi: 10.1016/j.chemolab.2004.12.011.

Colomina, I. and Molina, P. (2014) 'Unmanned aerial systems for photogrammetry and remote sensing: A review', *ISPRS Journal of Photogrammetry and Remote Sensing*, 92(June), pp. 79–97. doi: 10.1016/j.isprsjprs.2014.02.013.

Commission of the European Communities (CEC) (2006) 'Communication from the Commission to the Council, the European Parliament, the European Economic and Social Committee and the Committee of the Regions. Thematic Strategy for Soil Protection. COM 231 Final, Brussels.'

Conforti, M. *et al.* (2013) 'Studying the relationship between water-induced soil erosion and soil organic matter using Vis-NIR spectroscopy and geomorphological analysis: A case study in southern Italy', *Catena*. Elsevier B.V., 110, pp. 44–58. doi: 10.1016/j.catena.2013.06.013.

Corbane, C. *et al.* (2008) 'Remote sensing of soil surface characteristics from a multiscale classification approach', *Catena*. Elsevier B.V., 75(3), pp. 308–318. doi: 10.1016/j.catena.2008.07.009.

Cresswell, Hp. and Hamilton, G. J. (2002) 'Bulk density and pore space relations', *Soil physical measurement and interpretation for land evaluation*. CSIRO publishing Victoria, AU, 5, pp. 35–58.

Croft, H., Anderson, K. and Kuhn, N. J. (2009) 'Characterizing soil surface roughness using a combined structural and spectral approach', *European Journal of Soil Science*, 60(3), pp. 431–442. doi: 10.1111/j.1365-2389.2009.01129.x.

Croft, H., Anderson, K. and Kuhn, N. J. (2012) 'Reflectance anisotropy for measuring soil surface roughness of multiple soil types', *Catena*. Elsevier B.V., 93, pp. 87–96. doi: 10.1016/j.catena.2012.01.007.

Croft, H., Anderson, K. and Kuhn, N. J. (2014) 'Evaluating the influence of surface soil moisture and soil surface roughness on optical directional reflectance factors', *European Journal of Soil Science*, 65(4), pp. 605–612. doi: 10.1111/ejss.12142.

Crucil, G. *et al.* (2019) 'Assessing the performance of UAS-Compatible multispectral and hyperspectral sensors for soil organic carbon prediction', *Sustainability (Switzerland)*, 11(7). doi: 10.3390/su11071889.

Crucil, G. and Van Oost, K. (2021) 'Towards mapping of soil crust using multispectral imaging', *Sensors*. Multidisciplinary Digital Publishing Institute, 21(5), pp. 1–19. doi: 10.3390/s21051850.

D'Oleire-Oltmanns, S. *et al.* (2012) 'Unmanned aerial vehicle (UAV) for monitoring soil erosion in Morocco', *Remote Sensing*, 4(11), pp. 3390–3416. doi: 10.3390/rs4113390.

Ben Dor, E. (1997) 'The Reflectance Spectra of Organic Matter in the Visible Near-Infrared and Short Wave Infrared Region (400-2500 nm) during a Controlled Decomposition Process', *Remote Sensing of Environment*, 61, pp. 1–15.

Dvorakova, K. *et al.* (2020) 'Soil organic carbon mapping from remote sensing: The effect of crop residues', *Remote Sensing*, 12(12), pp. 1–25. doi: 10.3390/rs12121913.

Dvorakova, K., Heiden, U. and van Wesemael, B. (2021) 'Sentinel-2 Exposed Soil Composite for Soil Organic Carbon Prediction', *Remote Sensing* . doi: 10.3390/rs13091791.

Eltner, A. and Schneider, D. (2015) 'Analysis of Different Methods for 3D Reconstruction of Natural Surfaces from Parallel-Axes UAV Images', *Photogrammetric Record*, 30(151), pp. 279–299. doi: 10.1111/phor.12115.

Eltner, A., Schneider, D. and Maas, H. G. (2016) 'Integrated processing of high resolution topographic data for soil erosion assessment considering data acquisition schemes and surface properties', *International Archives of the Photogrammetry, Remote Sensing and Spatial Information Sciences - ISPRS Archives*, 41(July), pp. 813–819. doi: 10.5194/isprsarchives-XLI-B5-813-2016.

Eshel, G., Levy, G. J. and Singer, M. J. (2004) 'Spectral Reflectance Properties of Crusted Soils under Solar Illumination', *Soil Science Society of America Journal*, 68(6), pp. 1982–1991. doi: 10.2136/sssaj2004.1982.

FAO and ITPS (2015) *Status of the World's Soil Resources (SWSR) – Main Report. Food and Agriculture Organization of the United Nations and Intergovernmental Technical Panel on Soils, Rome, Italy*.

Fazeli, H., Samadzadegan, F. and Dadrasjavan, F. (2016) 'Evaluating the potential of RTK-UAV for automatic point cloud generation in 3D rapid mapping', *International Archives of the Photogrammetry, Remote Sensing and Spatial Information Sciences - ISPRS Archives*, 41(July), pp. 221–226. doi: 10.5194/isprsarchives-XLI-B6-221-2016.

Fearn, T. (2001) 'Standardisation and calibration transfer for near infrared instruments: A review', *Journal of Near Infrared Spectroscopy*, 9(4), pp. 229–244. doi: 10.1255/jnirs.309.

Fiener, P. and Auerswald, K. (2016) 'Comment on "The new assessment of soil loss by water erosion in Europe" by Panagos et al. (Environmental Science & Policy 54 (2015) 438-447)', *Environmental Science and Policy*. Elsevier Ltd, 57, pp. 140–142. doi: 10.1016/j.envsci.2015.12.012.

Franceschini, M. H. D. *et al.* (2018) 'Effects of external factors on soil reflectance measured on-the-go and assessment of potential spectral correction through orthogonalisation and standardisation procedures', *Soil and Tillage Research*. Elsevier, 177(November 2017), pp. 19–36. doi: 10.1016/j.still.2017.10.004.

Galvao, L. S. and Vitorello, I. (1998) 'Role of organic matter in obliterating the effects of iron on spectral reflectance and colour of Brazilian tropical soils', *International Journal of Remote Sensing*, 19(10), pp. 1969–1979.

GDAL/OGR contributors (2020) 'GDAL/OGR Geospatial Data Abstraction software Library. Open Source Geospatial Foundation, Available at: https://gdal.org.' Available at: https://gdal.org.

Ge, Y. *et al.* (2011) 'Comparison of soil reflectance spectra and calibration models obtained using multiple spectrometers', *Geoderma*. Elsevier B.V., 161(3–4), pp. 202–211. doi: 10.1016/j.geoderma.2010.12.020.

Geeves, G. W. (1998) *Aggregate breakdown and soil surface sealing under rainfall*. The Australian National University (Australia).

Ghamisi, P. *et al.* (2019) 'Multisource and multitemporal data fusion in remote sensing: A comprehensive review of the state of the art', *IEEE Geoscience and Remote Sensing Magazine*, 7(1), pp. 6–39. doi: 10.1109/MGRS.2018.2890023.

Gilliot, J. M. *et al.* (2017) 'Estimation des teneurs en carbone organique des sols agricoles par télédétection par drone', *Revue Francaise de Photogrammetrie et de Teledetection*, pp. 213–214.

Glendining, M. J. *et al.* (1997) 'Fate of 15 N-labelled fertilizer applied to spring barley grown on soils of contrasting nutrient status', *Plant and Soil*. Springer,

195(1), pp. 83–98.

Goldshleger, N. *et al.* (2004) 'Soil reflectance as a tool for assessing physical crust arrangement of four typical soils in Israel', *Soil Science*, 169(10), pp. 677–687. doi: 10.1097/01.ss.0000146024.61559.e2.

Grunwald, S. (2009) 'Multi-criteria characterization of recent digital soil mapping and modeling approaches', *Geoderma*. Elsevier, 152(3–4), pp. 195–207. doi: 10.1016/J.GEODERMA.2009.06.003.

Guanter, L. *et al.* (2015) 'The EnMAP Spaceborne Imaging Spectroscopy Mission for Earth Observation', *Remote Sensing* . doi: 10.3390/rs70708830.

Hardie, M. and Almajmaie, A. (2019) 'Measuring and estimating the hydrological properties of a soil crust', *Journal of Hydrology*. Elsevier, 574(December 2018), pp. 12–22. doi: 10.1016/j.jhydrol.2019.04.031.

Hassan-Esfahani, L. *et al.* (2015) 'Assessment of surface soil moisture using high-resolution multi-spectral imagery and artificial neural networks', *Remote Sensing*, 7(3), pp. 2627–2646. doi: 10.3390/rs70302627.

Hussein, M. H., Awad, M. M. and Abdul-Jabbar, A. S. (2010) 'Effect of Surface Crust on Rainfall Infiltration in an Aridisoil in Northern Iraq', *European Water Publications*, 32(October), pp. 25–34. Available at: www.ewra.net.

Itten, I. K. *et al.* (2008) 'APEX - the Hyperspectral ESA Airborne Prism Experiment', *Sensors* . doi: 10.3390/s8106235.

Jakob, S., Zimmermann, R. and Gloaguen, R. (2017) 'The Need for Accurate Geometric and Radiometric Corrections of Drone-Borne Hyperspectral Data for Mineral Exploration: MEPHySTo-A Toolbox for Pre-Processing Drone-Borne Hyperspectral Data', *Remote Sensing*, 9(1). doi: 10.3390/rs9010088.

Kim, J. and Ivanov, V. Y. (2014) 'On the nonuniqueness of sediment yield at the catchment scale: The effects of soil antecedent conditions and surface shield', *Water Resources Research*, 50(2), pp. 1025–1045. doi: 10.1002/2013WR014580.

Kim, J., Ivanov, V. Y. and Fatichi, S. (2016) 'Environmental stochasticity controls soil erosion variability', *Scientific Reports*. Nature Publishing Group, 6(February), pp. 1–7. doi: 10.1038/srep22065.

King, C. *et al.* (2005) 'Remote-sensing data as an alternative input for the "STREAM" runoff model', *Catena*, 62(2–3), pp. 125–135. doi: 10.1016/j.catena.2005.05.008.

Kopačková, V. and Ben-Dor, E. (2016) 'Normalizing reflectance from different spectrometers and protocols with an internal soil standard', *International*

*Journal of Remote Sensing*, 37(6), pp. 1276–1290. doi: 10.1080/01431161.2016.1148291.

Kruse, F. A., Boardman, J. W. and Huntington, J. F. (2003) 'Comparison of airborne hyperspectral data and EO-1 Hyperion for mineral mapping', *IEEE Transactions on Geoscience and Remote Sensing*, 41(6), pp. 1388–1400. doi: 10.1109/TGRS.2003.812908.

Kühnel, A. and Bogner, C. (2017) 'In-situ prediction of soil organic carbon by vis–NIR spectroscopy: an efficient use of limited field data', *European Journal of Soil Science*, 68(5), pp. 689–702. doi: 10.1111/ejss.12448.

Laloy, E. and Bielders, C. L. (2008) 'Plot scale continuous modelling of runoff in a maize cropping system with dynamic soil surface properties', *Journal of Hydrology*, 349(3–4), pp. 455–469. doi: 10.1016/j.jhydrol.2007.11.033.

Lambot, S. *et al.* (2006) 'Analysis of air-launched ground-penetrating radar techniques to measure the soil surface water content', *Water Resources Research*. John Wiley & Sons, Ltd, 42(11). doi: https://doi.org/10.1029/2006WR005097.

Langhans, C. *et al.* (2011) 'Experimental rainfall-runoff data: Reconsidering the concept of infiltration capacity', *Journal of Hydrology*. Elsevier B.V., 399(3–4), pp. 255–262. doi: 10.1016/j.jhydrol.2011.01.005.

Leys, A. *et al.* (2007) 'Conservation tillage on loamy soils: Explaining the variability in interrill runoff and erosion reduction', *European Journal of Soil Science*, 58(6), pp. 1425–1436. doi: 10.1111/j.1365-2389.2007.00947.x.

Li, Z. and Fang, H. (2016) 'Impacts of climate change on water erosion: A review', *Earth-Science Reviews*. Elsevier B.V., 163, pp. 94–117. doi: 10.1016/j.earscirev.2016.10.004.

Matese, A. *et al.* (2015) 'Intercomparison of UAV, aircraft and satellite remote sensing platforms for precision viticulture', *Remote Sensing*, 7(3), pp. 2971–2990. doi: 10.3390/rs70302971.

McCool, D. K. and Williams, J. D. (2008) 'Soil Erosion by Water', in Jørgensen, S. E. and Fath, B. D. B. T.-E. of E. (eds). Oxford: Academic Press, pp. 3284–3290. doi: https://doi.org/10.1016/B978-008045405-4.00296-2.

Melendez-Pastor, I. *et al.* (2008) 'Identifying optimal spectral bands to assess soil properties with VNIR radiometry in semi-arid soils', *Geoderma*, 147(3–4), pp. 126–132. doi: 10.1016/j.geoderma.2008.08.004.

Menzies Pluer, E. G. *et al.* (2020) 'Pairing soil sampling with very-high resolution UAV imagery: An examination of drivers of soil and nutrient movement and agricultural productivity in southern Ontario', *Geoderma*.

Elsevier, 379(July), p. 114630. doi: 10.1016/j.geoderma.2020.114630.

Micasens Support (2021) *Micasens Support website*. Available at: https://support.micasense.com/hc/en-us/articles/115000351194-Rededge-Camera-Radiometric-Calibration-Model.

Milton, E. J. and Webb, J. P. (1987) 'Ground radiometry and airborne multispectral survey of bare soils', *International Journal of Remote Sensing*. Taylor & Francis, 8(1), pp. 3–14. doi: 10.1080/01431168708948611.

Montanarella, L. *et al.* (2016) 'World's soils are under threat', *Soil*, 2(1), pp. 79–82. doi: 10.5194/soil-2-79-2016.

Mouazen, A. M. *et al.* (2007) 'On-line measurement of some selected soil properties using a VIS-NIR sensor', *Soil and Tillage Research*, 93(1), pp. 13–27. doi: 10.1016/j.still.2006.03.009.

Movia, A., Beinat, A. and Crosilla, F. (2016) 'Shadow detection and removal in RGB VHR images for land use unsupervised classification', *ISPRS Journal of Photogrammetry and Remote Sensing*. International Society for Photogrammetry and Remote Sensing, Inc. (ISPRS), 119, pp. 485–495. doi: 10.1016/j.isprsjprs.2016.05.004.

Movia, Alessia, Beinat, A. and Crosilla, F. (2016) 'Shadow detection and removal in RGB VHR images for land use unsupervised classification', *ISPRS Journal of Photogrammetry and Remote Sensing*. Elsevier, 119, pp. 485–495.

Mulder, V. L. *et al.* (2011) 'The use of remote sensing in soil and terrain mapping - A review', *Geoderma*. Elsevier B.V., 162(1–2), pp. 1–19. doi: 10.1016/j.geoderma.2010.12.018.

Nawar, S. and Mouazen, A. M. (2017) 'Predictive performance of mobile vis-near infrared spectroscopy for key soil properties at different geographical scales by using spiking and data mining techniques', *Catena*. Elsevier B.V., 151, pp. 118–129. doi: 10.1016/j.catena.2016.12.014.

Nciizah, A. D. and Wakindiki, I. I. C. (2015) 'Soil sealing and crusting effects on infiltration rate: a critical review of shortfalls in prediction models and solutions', *Archives of Agronomy and Soil Science*, 61(9), pp. 1211–1230. doi: 10.1080/03650340.2014.998203.

Nearing, M. A., Govers, G. and Norton, L. D. (1999) 'Variability in Soil Erosion Data from Replicated Plots', *Soil Science Society of America Journal*, 63(6), pp. 1829–1835. doi: 10.2136/sssaj1999.6361829x.

Nebiker, S. *et al.* (2016) 'Light-weight multispectral uav sensors and their capabilities for predicting grain yield and detecting plant diseases', *International Archives of the Photogrammetry, Remote Sensing and Spatial*

*Information Sciences - ISPRS Archives*, 2016-Janua(July), pp. 963–970. doi: 10.5194/isprsarchives-XLI-B1-963-2016.

Nicodemus, F. (1977) 'Book Reviews', *Journal of the Optical Society of America*. OSA, 67(1), pp. 127–130. doi: 10.1364/JOSA.67.000127.

Nocita, M. *et al.* (2015) 'Soil Spectroscopy: An Alternative to Wet Chemistry for Soil Monitoring', *Advances in Agronomy*, 132(March), pp. 139–159. doi: 10.1016/bs.agron.2015.02.002.

Nouri, M. *et al.* (2017) 'Clay content mapping from airborne hyperspectral Vis-NIR data by transferring a laboratory regression model', *Geoderma*. Elsevier, 298, pp. 54–66. doi: 10.1016/J.GEODERMA.2017.03.011.

Nunes, J. P. *et al.* (2018) 'Better models are more effectively connected models', *Earth Surface Processes and Landforms*, 43(6), pp. 1355–1360. doi: 10.1002/esp.4323.

Oldeman, L. R., Hakkeling, R. T. A. and Sombroek, W. G. (1990) *World map of the status of human-induced soil degradation: an explanatory note.* International Soil Reference and Information Centre.

Panagos, P. *et al.* (2013) 'Estimating soil organic carbon in Europe based on data collected through an European network', *Ecological Indicators*. Elsevier, 24, pp. 439–450. doi: 10.1016/J.ECOLIND.2012.07.020.

Panagos, P. *et al.* (2015) 'The new assessment of soil loss by water erosion in Europe', *Environmental Science and Policy*. Elsevier Ltd, 54, pp. 438–447. doi: 10.1016/j.envsci.2015.08.012.

Pandey, A. *et al.* (2016) 'Physically based soil erosion and sediment yield models revisited', *Catena*. Elsevier B.V., 147, pp. 595–620. doi: 10.1016/j.catena.2016.08.002.

Peñuela, A., Javaux, M. and Bielders, C. L. (2015) 'How do slope and surface roughness affect plot-scale overland flow connectivity?', *Journal of Hydrology*, 528, pp. 192–205. doi: 10.1016/j.jhydrol.2015.06.031.

Phinzi, K. and Ngetar, N. S. (2019) 'The assessment of water-borne erosion at catchment level using GIS-based RUSLE and remote sensing: A review', *International Soil and Water Conservation Research*. Elsevier B.V., 7(1), pp. 27–46. doi: 10.1016/j.iswcr.2018.12.002.

Piekarczyk, J. *et al.* (2016) 'Effects of Soil Surface Roughness on Soil Reflectance Measured in Laboratory and Outdoor Conditions', *IEEE Journal of Selected Topics in Applied Earth Observations and Remote Sensing*, 9(2), pp. 827–834. doi: 10.1109/JSTARS.2015.2450775.

Pignatti, S. *et al.* (2015) 'Environmental products overview of the Italian hyperspectral prisma mission: The SAP4PRISMA project', in *2015 IEEE International Geoscience and Remote Sensing Symposium (IGARSS)*, pp. 3997–4000. doi: 10.1109/IGARSS.2015.7326701.

Pimstein, A., Notesco, G. and Ben-Dor, E. (2011) 'Performance of Three Identical Spectrometers in Retrieving Soil Reflectance under Laboratory Conditions This article has supplemental material available online.', *Soil Science Society of America Journal*. Madison, WI: Soil Science Society, 75, pp. 746–759. doi: 10.2136/sssaj2010.0174.

Pineux, N. *et al.* (2017) 'Can DEM time series produced by UAV be used to quantify diffuse erosion in an agricultural watershed?', *Geomorphology*. Elsevier B.V., 280, pp. 122–136. doi: 10.1016/j.geomorph.2016.12.003.

Pix4Dmapper SA (2022) 'Pix4Dmapper. Prilly, Switzerland. Version 4.4.12'. Prilly, Switzerland. Available at: https://www.pix4d.com/product/pix4dmapper-photogrammetry-software.

Prudnikova, E. and Savin, I. (2021) 'Some peculiarities of arable soil organic matter detection using optical remote sensing data', *Remote Sensing*, 13(12), pp. 1–26. doi: 10.3390/rs13122313.

Van den Putte, A. *et al.* (2013) 'Estimating the parameters of the Green-Ampt infiltration equation from rainfall simulation data: Why simpler is better', *Journal of Hydrology*. Elsevier B.V., 476, pp. 332–344. doi: 10.1016/j.jhydrol.2012.10.051.

Quine, T. A. and Van Oost, K. (2020) 'Insights into the future of soil erosion', *Proceedings of the National Academy of Sciences of the United States of America*, 117(38), pp. 23205–23207. doi: 10.1073/pnas.2017314117.

R Core Team (2021) 'R: A language and environment for statistical computing. R Foundation for Statistical Computing, Vienna, Austria. Version3.6.3'. Available at: https://www.r-project.org/.

*RedEdge Camera Radiometric Calibration Model* (no date). Available at: https://support.micasense.com/hc/en-us/articles/115000351194-Rededge-Camera-Radiometric-Calibration-Model (Accessed: 8 February 2020).

Renard, K. G. (1997) *Predicting soil erosion by water: a guide to conservation planning with the Revised Universal Soil Loss Equation (RUSLE)*. United States Government Printing.

Richter, R., Kellenberger, T. and Kaufmann, H. (2009) 'Comparison of topographic correction methods', *Remote Sensing*, 1(3), pp. 184–196. doi: 10.3390/rs1030184.

Romero, D. J. *et al.* (2018) 'Internal soil standard method for the Brazilian soil spectral library: Performance and proximate analysis', *Geoderma*, 312(July 2017), pp. 95–103. doi: 10.1016/j.geoderma.2017.09.014.

Roosjen, P. P. J. *et al.* (2017) 'Mapping reflectance anisotropy of a potato canopy using aerial images acquired with an unmanned aerial vehicle', *Remote Sensing*, 9(5). doi: 10.3390/rs9050417.

Rothamsted Research (2006) 'Guide to the Classical and other Long-term Experiments, Datasets and Sample Archive. Lawes Agriculture Trust Co. Ltd., Ltd, Harpenden, UK', *Lawes Agric. Trust Co., Harpenden, UK*, pp. 8–18.

Sandmeier, S. *et al.* (1998) 'Sensitivity Analysis and Quality Assessment of Laboratory BRDF Data', *Remote Sensing of Environment*, 64(2), pp. 176–191. doi: https://doi.org/10.1016/S0034-4257(97)00178-8.

Savitzky, A. and Golay, M. J. E. (1964) 'Smoothing and Differentiation of Data by Simplified Least Squares Procedures.', *Analytical Chemistry*. American Chemical Society, 36(8), pp. 1627–1639. doi: 10.1021/ac60214a047.

Schaepman-Strub, G. *et al.* (2004) 'About the importance of the definition of reflectance quantities - Results of case studies', *International Archives of the Photogrammetry, Remote Sensing and Spatial Information Sciences - ISPRS Archives*, 35.

Schlapfer, D., Richter, R. and Feingersh, T. (2015) 'Operational BRDF effects correction for wide-field-of-view optical scanners (BREFCOR)', *IEEE Transactions on Geoscience and Remote Sensing*, 53(4), pp. 1855–1864. doi: 10.1109/TGRS.2014.2349946.

Schmitt, M. and Zhu, X. X. (2016) 'Data Fusion and Remote Sensing: An ever-growing relationship', *IEEE Geoscience and Remote Sensing Magazine*, 4(4), pp. 6–23. doi: 10.1109/MGRS.2016.2561021.

Sherrod, L. A. *et al.* (2002) 'Inorganic carbon analysis by modified pressure-calcimeter method', *Soil Sci. Soc. Am. J.*, 66, pp. 299–305.

Shin, S. S., Park, S. D. and Choi, B. K. (2016) 'Universal power law for relationship between rainfall kinetic energy and rainfall intensity', *Advances in Meteorology*, 2016. doi: 10.1155/2016/2494681.

Siesler, H. W. *et al.* (2008) *Near-infrared spectroscopy: principles, instruments, applications*. John Wiley & Sons.

Singer, M. J. and Shainberg, I. (2004) 'Mineral soil surface crusts and wind and water erosion', *Earth Surface Processes and Landforms*, 29(9), pp. 1065–1075. doi: 10.1002/esp.1102.

Soriano-Disla, J. M. *et al.* (2017) 'Evaluation of the performance of portable visible-infrared instruments for the prediction of soil properties', *Biosystems Engineering*, 161, pp. 24–36. doi: 10.1016/j.biosystemseng.2017.06.017.

Stenberg, B. *et al.* (2010) 'Visible and Near Infrared Spectroscopy in Soil Science', *Advances in Agronomy*, 107(C), pp. 163–215. doi: 10.1016/S0065-2113(10)07005-7.

Stevens, A. *et al.* (2010) 'Measuring soil organic carbon in croplands at regional scale using airborne imaging spectroscopy', *Geoderma*, 158(1), pp. 32–45. doi: https://doi.org/10.1016/j.geoderma.2009.11.032.

Stevens, Antoine *et al.* (2013) 'Prediction of Soil Organic Carbon at the European Scale by Visible and Near InfraRed Reflectance Spectroscopy', *PLoS ONE*, 8(6). doi: 10.1371/journal.pone.0066409.

Stevens, A *et al.* (2013) 'Prediction of Soil Organic Carbon at the European Scale by Visible and Near InfraRed Reflectance Spectroscopy', *PLoS One*, 8(6), p. e66409. doi: 10.1371/journal.pone.0066409.

Stevens, A. and Ramirez-Lopez, L. (2013) 'An introduction to the prospectr package. R package Vignette R package. Version 0.1.3.'

Surveying, S. (2013) 'an Index-Based Shadow Extraction Approach on High-Resolution', *Proceedings of the International Symposium on Satellite Mapping Technology and Application, Nanjing, China, 6–8 November 2013*, pp. 19–26. Available at: http://www.isprs.org/proceedings/2013/ISSMTA2013/04.pdf.

SZ DJI Technology Co., L. (2018) 'DJI Ground Station Pro. Version 2.0.15'. Shenzhen, China. Available at: https://www.dji.com/it/ground-station-pro.

'The contribution of diffuse reflectance spectroscopy to soil organic carbon analysis : from laboratory to airborne' (no date).

Thomsen, L. M. *et al.* (2015) 'Soil surface roughness: Comparing old and new measuring methods and application in a soil erosion model', *Soil*, 1(1), pp. 399–410. doi: 10.5194/soil-1-399-2015.

Tóth, G., Jones, A. and Montanarella, L. (2013) 'The LUCAS topsoil database and derived information on the regional variability of cropland topsoil properties in the European Union', *Environmental Monitoring and Assessment*, 185(9), pp. 7409–7425. doi: 10.1007/s10661-013-3109-3.

Tziolas, N. *et al.* (2021) 'Earth observation data-driven cropland soil monitoring: A review', *Remote Sensing*, 13(21). doi: 10.3390/rs13214439.

Valentin, C. and Bresson, L.-M. (1992) 'Morphology, genesis and classification

of surface crusts in loamy and sandy soils', *Geoderma*, 55(3–4), pp. 225–245. doi: 10.1016/0016-7061(92)90085-L.

Valentin, C. and Bresson, L. M. (1998) 'Soil crusting', *Soil crusting*.

Viscarra Rossel, R. A. *et al.* (2006) 'Visible, near infrared, mid infrared or combined diffuse reflectance spectroscopy for simultaneous assessment of various soil properties', *Geoderma*, 131(1–2), pp. 59–75. doi: 10.1016/j.geoderma.2005.03.007.

Viscarra Rossel, R. A. *et al.* (2016) 'A global spectral library to characterize the world's soil', *Earth-Science Reviews*, 155(February), pp. 198–230. doi: 10.1016/j.earscirev.2016.01.012.

Wassenaar, T. *et al.* (2005) 'Soil surface infiltration capacity classification based on the bi-directional reflectance distribution function sampled by aerial photographs. The case of vineyards in a Mediterranean area', *Catena*, 62(2–3), pp. 94–110. doi: 10.1016/j.catena.2005.05.004.

Wehrhan, M., Rauneker, P. and Sommer, M. (2016) 'UAV-based estimation of carbon exports from heterogeneous soil landscapes—a case study from the carboZALF experimental area', *Sensors (Switzerland)*, 16(2). doi: 10.3390/s16020255.

Wischmeier, W. H. and Smith, D. D. (1978) *Predicting rainfall erosion losses: a guide to conservation planning*. Department of Agriculture, Science and Education Administration.

Wold, S., Sjöström, M. and Eriksson, L. (2001) 'PLS-regression: A basic tool of chemometrics', *Chemometrics and Intelligent Laboratory Systems*, 58(2), pp. 109–130. doi: 10.1016/S0169-7439(01)00155-1.

Wrb, I. W. G. (2015) 'World Reference Base for Soil Resources 2014, update 2015 International soil classification system for naming soils and creating legends for soil maps', *World Soil Resources Reports No. 106*. FAO Rome, p. 192.

Wu, K. *et al.* (2019) 'A new drone-borne GPR for soil moisture mapping', *Remote Sensing of Environment*. Elsevier, 235(May), p. 111456. doi: 10.1016/j.rse.2019.111456.

Zaher, H., Caron, J. and Ouaki, B. (2005) 'Modeling Aggregate Internal Pressure Evolution following Immersion to Quantify Mechanisms of Structural Stability', *Soil Science Society of America Journal*, 69(1), p. 1. doi: 10.2136/sssaj2005.0001.

Zhang, C. and Kovacs, J. M. (2012) 'The application of small unmanned aerial systems for precision agriculture: A review', *Precision Agriculture*, 13(6), pp.

693–712. doi: 10.1007/s11119-012-9274-5.

Zhang, D. and Zhou, G. (2016) 'Estimation of soil moisture from optical and thermal remote sensing: A review', *Sensors (Switzerland)*, 16(8). doi: 10.3390/s16081308.

Zhang, H. *et al.* (2021) 'Evaluating the capability of a UAV-borne spectrometer for soil organic carbon mapping in bare croplands', *Land Degradation and Development*, 32(15), pp. 4375–4389. doi: 10.1002/ldr.4043.

Žížala, D., Zádorová, T. and Kapička, J. (2017) 'Assessment of Soil Degradation by Erosion Based on Analysis of Soil Properties Using Aerial Hyperspectral Images and Ancillary Data, Czech Republic', *Remote Sensing*, 9(1), p. 28. doi: 10.3390/rs9010028.

# List of Figures

Figure 1.1. This conceptual workflow represents how the four objectives of this thesis have been structured to pursue the general objective. The work started with a test of sensors and their detection capability for soil properties, moving from laboratory analysis and progressively scaling to proximal sensing in outdoor and field conditions, and finally to the remote sensing domain. ... 13

Figure 2.1. Flowchart of the experimental design..... 19

Figure 2.2. The experiment setup in laboratory (left) and outdoor (right) conditions..... 22

Figure 2.3. Pearson's correlation plot between SOC and spectral wavelengths for the "ASDfull" laboratory (dashed line) and outdoor (solid line) setups. The spectral windows of the Sequoia (Seq) are highlighted in red and Mini-MCA6 (Tc) in blue. ..... 27

Figure 2.4. RMSE and RPD from the validation of the models built under laboratory conditions: "ASD", "ASDfull", "STS", "ASD res Seq", and "ASD res Tc". ..... 29

Figure 2.5. RMSE and RPD from the validation of the models built under outdoor conditions: "ASD", "ASDfull", "STS", "ASD res Seq", "ASD res Tc", "Seq", and "Tc". ..... 30

Figure 2.6. VIP scores in the vis-NIR range from the PLSR models: laboratory and outdoor "ASD", laboratory and outdoor "ASD res Seq" and "ASD res Tc", and outdoor "Seq" and "Tc". ..... 31

Figure 2.7. Example of soil sample spectrum as registered by the ASD in laboratory conditions (in blue) and by ASD and STS in outdoor conditions (green and black, respectively). Head and tail of the STS signal are zoomed to highlight the higher noise, as compared to the ASD signals. ..... 34

Figure 3.1. Data series structure (left) and variables (right). ..... 42

Figure 3.2. Illustration of a soilbox used during the experiments..... 43

Figure 3.3. Roughness characterization using photogrammetry: (a) an illustration of the 3D mesh and the estimated positions of the camera; (b) detailed view of the 3D mesh from close distance; (c) DTM with hillshade representation. In the middle (d) an

example of random roughness map, for the same soilbox, in three subsequent phases (left to right: before, after first and after second rainfall application) and, on the bottom (e), their corresponding RGB images. ..... 46

Figure 3.5. Example of RGB composite from multispectral image that shows the steps of pixel selection for the selective extraction of spectral data: original image; base dataset (with shadows removed) at 2 mm and 15 mm resampling; DR dataset (with roughness threshold < 2 mm) at 2 mm and 15 mm resampling. The images at 2 mm resolution also display with white lines the 6 × 6 grid used for partitioning reflectance histogram extraction. ..... 48

Figure 3.6. (a) Example of the evolution of the multispectral pixel density histograms, for two spectral bands drawn as an example (blue and NIR, respectively coloured in blue and grey), from a single soilbox across two different amounts of cumulated rainfall kinetic energy (0 and 5500 J/m$^2$). The *iqr* is visualized as the span distance between the 1st and 3rd quantile of each histogram; (b) example of the evolution of mean multispectral reflectance values (points) and corresponding hyperspecral reflectance samples (lines) at the same soilbox location, for three levels of KE (0, 1160 and 2320 J/m$^2$). ..... 50

Figure 3.7. Flowchart of data selection and sub-setting for the PLSR modelling of multispectral data. ..... 52

Figure 3.8. Scatterplot of KE in J/m2 and RC. The pertinence to the four data series is highlighted with colours. Correlation values with p < 0.05 are marked with *. ..... 53

Figure 3.9. Scatterplot of KE in J/m2 and measured roughness in mm of standard deviation, detailed for the 2 mm resolution. Data histograms are plotted side by side to the respective axes..... 54

Figure 3.10. Scatterplot of KE in J/m$^2$ and measured roughness in mm of standard deviation, detailed for the 15 mm resolution. Data histograms are plotted side by side to the respective axes. The pertinence to the four data series is highlighted with colours. Correlation values with $p < 0.05$ are marked with *..... 54

Figure 3.11. VIP scores of KE PLSR models from hyperspectral data using full vis-NIR-SWIR reflectance spectral range. Goodness of fit is

reported using $R^2$ and RPIQ. The multispectral broad-bands of the Rededge-M camera model are shown for comparison. .... 55

Figure 3.12. VIP scores of KE PLSR models from hyperspectral data using the SNV of the full vis-NIR-SWIR spectral range. Goodness of fit is reported with $R^2$ and RPIQ. The multispectral broad-bands of the Rededge-M camera model are shown for comparison. .... 56

Figure 3.13. VIP scores of KE PLSR models from hyperspectral data using: (a) reflectance vis-NIR range; (b) SNV vis-NIR range. Goodness of fit is reported with $R^2$ and RPIQ. The multispectral broad-bands of the Rededge-M camera model are shown for comparison. .... 56

Figure 3.14. Correlation of the multispectral indexes with KE (a) and with roughness (b) from the 2 mm resolution dataset: "refl" represents the base dataset, "DR" the roughness threshold dataset, "SNV" the Standard Normal Variate transformation of reflectance data. Points where $p < 0.05$ were excluded from the plot. ..... 58

Figure 3.15. Validation of the PLSR models (using $R^2$) for the different data transformations, ordered by their degree of roughness removal, from left (none) to rigth (max). Black symbols depict KE models $R^2$, while red symbols represent RG models $R^2$. Solid symbols represent models based on spectral data + *iqr*, void symbols represent models based on spectra only. Panel (a) shows result for the 2 mm scale, panel (b) results for the 15 mm scale. ..... 61

Figure 3.16. Validation of the PLSR models (using RPIQ) for the different data transformations, ordered by their degree of roughness removal, from left (none) to rigth (max). Black symbols depict KE models $R^2$, while red symbols represent RG models $R^2$. Solid symbols represent models based on spectral data + *iqr*, void symbols represent models based on spectra only. Panel (a) shows result for the 2 mm scale, panel (b) results for the 15 mm scale. ..... 62

Figure 4.1. Experimental setting of the plots, with placement in the field (a), close-up example of a plot (b and c), and close-up of the funnel and runoff collector (d). ..... 69

Figure 4.2 Example of a single plot evolution with increased levels of KE, as seen by the rededge channel of the multispectral camera. Associated KE levels are indicated below each image. ..... 71

Figure 4.3. Example image, in false RGB, of a soil plot before (left) and after (right) shadow removal and roughness thresholding. ..... 71

Figure 4.4. Distribution of hyperspectral measurement spots. They were distributed to evenly cover each plot in 4 rows at 30, 60, 90 and 120 cm from the outlet, with inter-column distance of 25 cm. ..... 72

Figure 4.5. Example of sampling grid for extraction and averaging of multispectral data in a plot (a) and PLSR modelling flowchart (b). ..... 73

Figure 4.6. Monthly cumulated precipitations measured on the experiment plots, in the context of monthly average (dashed black line), minima and maxima (bottom and top full black lines) measured at the nearby Wavre meteorological station in the period 2000-2017. April and July are represented by empty dots as only part of those months was measured (last 10 days of April, first 9 days of July). ..... 75

Figure 4.7. Data synopsis: blue bars for rainfall events (separated by at least 1h of no rainfall), red lines for drone flights, black dotted lines for runoff/sediment collection. ..... 75

Figure 4.8. Observed vs Predicted KE values from the validation phase of PLSR modelling of multispectral data, with different reflectance data types: a) reflectance; b) SNV of reflectance. Each point shows the boxplot of the standard deviation of predicted values from the validation process. Plot results from the "*iqr*" dataset were omitted. ..... 77

Figure 4.9. $R^2$ and RPIQ random resampling validation results from PLSR models of KE. ..... 78

Figure 4.10. Variable importance (VIP) from PLSR models of KE, from both hyperspectral (lines) and multispectral (points) data, with reflectance (black) and standard normal variate (red). The spectral broad-bands of the Micasense Rededge, used in this study, are visualized as coloured strips. ..... 78

Figure 4.11. Scatterplot and Pearson's correlation of sediment and precipitation data: S = dry sediment (g), Rf = total rainfall (g) applied on plot during a single measuring period, KE = total kinetic energy cumulated on plot before the measuring period,

S.Rf = soil eroded per unit of input rainfall. Significance codes (p-values): 0 < '***'< 0.001 <'**'< 0.01 <'*'< 0.05 <'.'< 0.1 <' '< 1. Correlation values between brackets ([1]) were calculated omitting the data from the first measurement ("fo" dataset at KE = 0). ..... 80

Figure 4.12. Model results, in terms of $R^2$, RPD and RPIQ, for sediment (S) and sediment for unit of rainfall (S.Rf) prediction. Predictor variables were the rainfall generating each specific sediment export (Rf), the measured, previously cumulated kinetic energy (KE), the standard normal variate of the Micasense rededge spectra (SNV). Type of model is indicated under the horizontal axis. RPD values in are marked in black, RPIQ in red. (fo) indicates dataset where the first measured rainfall was excluded ..... 81

Figure 5.1. Locations within Belgian border (a), and more in detail within the Belgian loam belt area (c), of the UAS flights used in this study. A close-up example of soil conditions is reported in frame (b). ..... 89

Figure 5.2. Scheme for the calculation of the pixel nadir coordinates and of the sensor zenith relative to the nadir "PS_zen" angle in a tilted (by pitch and roll angles) sensor reference system. ..... 91

Figure 5.3. Visualization of the relative angles extracted for BRDF modelling within the sun-pixel-sensor framework: a) relative azimuth "*Rel_az*"; b) sensor zenith "*PS_zen*", solar zenith "*Sol_zen*", relative zenith "*Rel_zen*"..... 92

Figure 5.4. Workflow for ANIF model calibration and application..... 93

Figure 5.5. a) example of Micasense Rededge picture of flat soil, shot from 45 m above ground level, after manual radiometric calibration, vignetting correction, black level compensation and conversion to reflectance (rededge band as example): to be noted how it is affected by reflectance gradient due to back- and forward-scattering effects of incoming sunlight; b) example of Pix4D-generated spectral orthomosaic (rededge band as example) obtained from a dataset of images non corrected for the soil anisotropy effects. The image positions, along the flight lines, are put in evidence (green dots) to show their correspondence with the "stripes" artefact. The rededge band has been arbitrary

chosen for display purposes only, as all spectral bands exhibited the same behaviour. ..... 96

Figure 5.6. a) Example of transect drawing on a map affected by the stripes artefact; b) Example of transect spectral data, from the original dataset, and the corresponding linear interpolation. The position of flight lines (sensor vertical position) is indicated as black dashed lines. ..... 97

Figure 5.7. From a subsampling of the ensemble of the 12 calibration datasets: a) correlation plot of *Rel_az* (in radians) against the ANIF; b) correlation plot of *Rel_zen* (in radians) against the ANIF, with the 3rd order polynomial interpolation lines from the different datasets..... 99

Figure 5.8. Observed vs predicted plot of the ANIF from the modelling of the calibration (a) and validation (b) datasets. $R^2$, RMSE and MRE % are indicated below each respective plot. ..... 100

Figure 5.9. Example of reflectance picture (rededge band) before (left) and after (right) ANIF correction. The yellow lines represent the transect from which spectral data were extracted to check the result of spectral normalization. The data extracted from the transects are plotted under the respective images, in black for the original image and in orange for the corrected one..... 100

Figure 5.10**.** Results of step (i) analysis: density distribution for a calibration sample size n = 220 and validation sample size n = 80 of the standard deviation *sd* of reflectance for same pixel observation by different camera positions/angles (9-20 different camera observation per pixel), before and after ANIF correction (black and orange lines respectively). ..... 102

Figure 5.11**.** Results of step (ii): example of transect spectral data evaluation (Hostellerie dataset), before and after image correction (black and orange, respectively), and the corresponding linear interpolation. The position of flight lines (sensor vertical position) is added as black dashed lines. The *SSin* calculated for the original transect was 1.030 while that for the corrected transect 1.022. ..... 102

Figure 5.12**.** Results of step (ii): average spectral Sinuosity index *SSin* for each field. Black = original orthomosaics, orange = corrected

orthomosaics. The % difference between *SSin* of corrected and original reflectance transects is indicated above each point. 103

Figure 5.13. Results of step (ii): correlation between striping magnitude and distance to the vertical of the closest flight line/sensor position, measured across spectral transects. 103

Figure 5.14. Example of original (a) and ANIF-corrected (b) final spectral orthomosaic (rededge band example) for the flight Hostellerie 02/09/2018. 104

Figure A 1. Plots of observed versus predicted SOC values from the models used in the comparison of the measuring setups. Vertical error bars represent the standard deviation obtained from the validation process through 100x random selection. 116

Figure B 1. Example of the procedure for shadow threshold individuation on a soil multispectral image: difference in reflectance between illuminated and shadowed calibration pixel (a) and the brightness curves after sorting and detrending to make the shadow threshold stand out as a local maximum (b). 117

Figure B 2. Example of soilbox image (false colour RGB composite) before de-shadowing (left), and after de-shadowing at 2 mm resolution (top right) and 15 mm resolution (bottom right). 118

Figure B 3. Statistics on the percentage of pixel removal due to shadow across the full dataset: percentage of pixel removal across the samples at 2 mm resolution (top left); percentage of pixel removal across the samples at 15 mm resolution (bottom left); relative percentage difference in pixel removal between same samples at different resolutions (right). 119

Figure C 1. Original (left) and ANIF-corrected (right) final spectral orthomosaic (rededge band example) for the flight Ernage 20190420. 121

Figure C 2. Original (left) and ANIF-corrected (right) final spectral orthomosaic (rededge band example) for the flight Thorembais 20180507. 121

Figure C 3. Original (left) and ANIF-corrected (right) final spectral orthomosaic (rededge band example) for the flight Villeroux a1 20190827. 121

Figure C 4. Original (left) and ANIF-corrected (right) final spectral orthomosaic (rededge band example) for the flight Villeroux a2 20190914. 122

Figure C 5. Original (left) and ANIF-corrected (right) final spectral orthomosaic (rededge band example) for the flight Sicy 20180902. ..... 122

Figure C 6. Original (left) and ANIF-corrected (right) final spectral orthomosaic (rededge band example) for the flight Gembloux F2 20210423. .. 122

Figure C 7. Original (left) and ANIF-corrected (right) final spectral orthomosaic (rededge band example) for the flight Gembloux F3 20210423. .. 123

Figure C 8. Original (left) and ANIF-corrected (right) final spectral orthomosaic (rededge band example) for the flight Gembloux F4 20210423. .. 123

Figure C 9. Original (left) and ANIF-corrected (right) final spectral orthomosaic (rededge band example) for the flight Marbaix 20180506. ..... 123

Figure C 10. Original (left) and ANIF-corrected (right) final spectral orthomosaic (rededge band example) for the flight Beuzet N 20180508. ..... 124

Figure C 11. Original (left) and ANIF-corrected (right) final spectral orthomosaic (rededge band example) for the flight Beuzet S 20180508..... 124

Figure C 12. Original (left) and ANIF-corrected (right) final spectral orthomosaic (rededge band example) for the flight Geeste 1 20180902. ..... 124

Figure C 13. Original (left) and ANIF-corrected (right) final spectral orthomosaic (rededge band example) for the flight Geeste 3 20180902. ..... 125

# List of Tables

Table 2.1. Spectral resolution of the sensors used in this study. ..... 21

Table 2.2. RMScorr of the four spectral regions for the “ASDfull” laboratory and outdoor setups. ..... 27

Table 2.3. RE%, RMSE (g·kg-1), RPD, RPIQ, and $R^2$ of the validation PLSR performances (data reported represents the mean value over 100 repetitions) for all the instruments and setups: “ASD”, “ASDfull”, “STS”, “ASD res Seq”, “ASD res Tc”, “Seq”, and “Tc”. The number of latent variables (n° comp) used in each model is also reported. ..... 28

Table 2.4. RMSE (g·kg-1), RPD, RPIQ, and $R^2$ of PLSR performances of transferred models, both with and without the application of a spectral correction using an internal soil standard ..... 32

Table 3.1. VIP scores from the multispectral data PLSR models of kinetic energy (KE) and roughness (RG) at the two different resolutions. VIP scores higher than 1 are marked with grey colour cells. ..... 64

Table 5.1. General flight information of the UAS-flights database: name, execution date, lateral overlap %, flight line and sunlight direction, and whether the dataset has been used for ANIF model calibration or validation. Names marked with an (*) represent datasets that in the original orthomosaic generation phase showed a prominent “striping” artefact effect. Flight altitude was ca. 45 m above ground level in all cases. ..... 88